

12-2014

In Vivo Dosimetry using Plastic Scintillation Detectors for External Beam Radiation Therapy

Landon S. Wootton

Follow this and additional works at: https://digitalcommons.library.tmc.edu/utgsbs_dissertations

 Part of the [Medicine and Health Sciences Commons](#)

Recommended Citation

Wootton, Landon S., "In Vivo Dosimetry using Plastic Scintillation Detectors for External Beam Radiation Therapy" (2014). *The University of Texas MD Anderson Cancer Center UTHealth Graduate School of Biomedical Sciences Dissertations and Theses (Open Access)*. 525.
https://digitalcommons.library.tmc.edu/utgsbs_dissertations/525


This Dissertation (PhD) is brought to you for free and open access by the The University of Texas MD Anderson Cancer Center UTHealth Graduate School of Biomedical Sciences at DigitalCommons@TMC. It has been accepted for inclusion in The University of Texas MD Anderson Cancer Center UTHealth Graduate School of Biomedical Sciences Dissertations and Theses (Open Access) by an authorized administrator of DigitalCommons@TMC. For more information, please contact digitalcommons@library.tmc.edu.

IN VIVO DOSIMETRY USING PLASTIC SCINTILLATION DETECTORS FOR
EXTERNAL BEAM RADIATION THERAPY

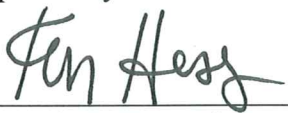
by

Landon Scott Wootton, B.S.


APPROVED:



Sam Beddar, Ph.D.
Supervisory Professor



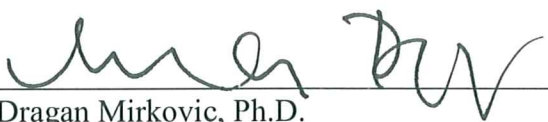
Kenneth R. Hess, Ph.D.



Rajat J. Kudchadker, Ph.D.



Andrew K. Lee, M.D.



Dragan Mirkovic, Ph.D.

APPROVED:

Dean, The University of Texas
Graduate School of Biomedical Sciences at Houston

IN VIVO DOSIMETRY USING PLASTIC SCINTILLATION DETECTORS FOR
EXTERNAL BEAM RADIATION THERAPY

A
DISSERTATION

Presented to the Faculty of
The University of Texas
Health Science Center Houston
and

The University of Texas
MD Anderson Cancer Center
Graduate School of Biomedical Sciences
in Partial Fulfillment

of the Requirements

for the Degree of

DOCTOR OF PHILOSOPHY

by

Landon Scott Wootton, B.S.

Houston, Texas

December 2014

DEDICATION

This work is dedicated to my loving wife and best friend Whitney, to my parents Robert and Cathy, my brother Marshall, to the rest of my wonderful family, and especially to Rudy Pirovitz: a kind hearted high school physics teacher who inspired me to be a physicist.

ACKNOWLEDGEMENTS

First and foremost I'd like to acknowledge and thank Dr. Beddar for his mentorship, support and guidance without whom this work would not have been possible. I'd like to acknowledge all the members of my committees, past and present: Dr. Mirkovic, Dr. Zhu, Dr. Sahoo, Dr. Johnson, Dr. Hess, Dr. Wendt, Dr. Briere, and particularly Dr. Lee and Dr. Kudchadker who have been instrumental in the course of this research and in my education. Thanks to current and former lab members: Francois Therriault-Proulx, David Klein, Daniel Robertson, Lelei Wang, Clint Zeringue, Slade Klawikowski, Beckett Hui, Thomas Henry, and Gustavo Kertzsch. Thanks especially to Francois and David who served as mentors to me when I first joined. Thanks to the many people who have helped along the way. There are too many to name, and I owe each a debt of gratitude. Finally, a special thanks to the members of the American Legion Auxiliary for their support through the American Legion Auxiliary Fellowship in Cancer Research.

IN VIVO DOSIMETRY USING PLASTIC SCINTILLATION DETECTORS FOR EXTERNAL BEAM RADIATION THERAPY

Landon Scott Wootton, B.S.

Supervisory Professor: Sam Beddar, Ph.D.

In vivo dosimetry, the direct measurement of dose delivered to patients during radiation therapy, has significant potential in ensuring safe and effective treatment in radiation therapy. It can serve as point-of-delivery, patient specific quality assurance and direct verification of treatment. Despite evidence that *in vivo* dosimetry can detect errors in patient treatment that would otherwise go undetected, it is not commonly practiced. This is due in part to a lack of available detectors ideally suited to perform *in vivo* dosimetry. Plastic scintillation detectors (PSDs) possess a number of dosimetric characteristics advantageous for *in vivo* dosimetry including water equivalence, real-time capability, small size, and energy independence. However, PSDs have not been used for *in vivo* dosimetry of external beam radiation therapy to date. The overall purpose of this work is to apply PSDs to *in vivo* dosimetry of external beam radiation therapy, and demonstrate the utility and practicality of performing *in vivo* dosimetry with PSDs.

Three avenues of research were pursued in accordance with this purpose. First, the temperature dependence of PSDs was characterized. Prior to this work, PSDs were understood to be temperature independent detectors. However responses of PSDs constructed with BCF-60 and BCF-12, two common scintillating fibers, were

demonstrated to decrease by 0.5% and 0.1% per °C increase relative to 22 °C, respectively. The spectral distribution of light was observed to change with temperature as well. This resulted in a non-negligible error in measured dose at human body temperature, requiring a temperature-specific correction factor.

Next, PSDs were used for *in vivo* dosimetry of the rectal wall in five patients undergoing intensity modulated radiation therapy for prostate cancer. This was done as part of an Institutional Review Board approved protocol. PSDs were attached to endorectal balloons used routinely during prostate radiotherapy, positioning the detectors in close proximity with the rectal wall. Two PSDs were used for two treatment fractions each week for the duration of each patient's treatment. The difference between the measured dose and expected dose was used to evaluate the accuracy and precision of the system. The mean difference between the measured and expected dose for the five patient population was -0.4%, with a standard deviation of 2.8%. The mean differences for individual patients fell between -3.3% and 3.3%.

Finally, a thorough characterization of the response of PSDs used for absolute entrance dosimetry in proton beams was performed. Entrance dose measurements for a passively scattered proton beam performed with a PSD were compared to measurements made with an ion chamber and radiochromic film. Ionization quenching, an under-response due to densely ionizing radiation, was found to be responsible for a 7% loss of signal at the highest energy studied (250 MeV) and a 10% loss at the lowest (140 MeV). The under-response was found to be insensitive to other beam parameters, such as the width of the spread out Bragg peak.

TABLE OF CONTENTS

Title Page	ii
Dedication	iii
Acknowledgements	iv
Abstract	v
Table of Contents	vii
List of Illustrations	xi
List of Tables	xiii
Abbreviations	xiv
1. Introduction	1
1.1 Purpose Statement	2
1.2 Rationale and Significance	2
1.3 Specific Aims	4
1.4 Organization	5
2. Background	6
2.1 Physical Mechanism of Scintillation	7
2.2 Design of Plastic Scintillation Detector Systems	12
2.3 Dosimetric Properties of Plastic Scintillation Detectors	16
2.4 <i>In Vivo</i> Dosimetry	18
2.5 Challenges of <i>In Vivo</i> Dosimetry	21
2.6 Plastic Scintillation Detectors for <i>In Vivo</i> Dosimetry	23
3. Temperature Dependence of Plastic Scintillation Detectors	26

3.1 Introduction	27
3.2 Methods and Materials	29
3.2.1 Detectors	29
3.2.2 Experimental Setup.....	30
3.2.3 Dose Measurements	32
3.2.4 Spectrometry.....	33
3.2.5 Detector Stabilization	35
3.3 Results	35
3.3.1 Dose Measurements	35
3.3.2 Spectrometry.....	37
3.3.3 Detector Stabilization.....	41
3.4 Discussion	45
3.5 Conclusion.....	50
4. Internal <i>In Vivo</i> Dosimetry for Prostate Intensity Modulated Radiation Therapy	51
4.1 Introduction.....	52
4.2 Methods and Materials.....	54
4.2.1 Detector Design.....	54
4.2.2 Protocol Design.....	57
4.2.3 Imaging Methodology.....	61
4.2.4 Data Acquisition.....	62
4.2.5 Data Analysis	63
4.3 Results.....	64

4.3.1 <i>Imaging Methodology</i>	64
4.3.2 <i>In Vivo Results</i>	64
4.4 Discussion.....	69
4.5 Conclusion	76
5. Passively Scattered Proton Beam Entrance Dosimetry with Plastic Scintillation	
Detectors	77
5.1 Introduction.....	78
5.2 Methods and Materials.....	80
5.2.1 <i>Detectors</i>	80
5.2.2 <i>Setup</i>	82
5.2.3 <i>Ionization Quenching Characterization</i>	83
5.2.4 <i>Cerenkov Light Removal</i>	84
5.2.5 <i>Accuracy and Precision of Relative Dose Measurements</i>	85
5.3 Results.....	86
5.3.1 <i>Response vs Range</i>	86
5.3.2 <i>Response vs SOBP Width</i>	88
5.3.3 <i>Cerenkov Light Contribution</i>	88
5.3.4 <i>Profile Measurements</i>	91
5.3.5 <i>SNR</i>	91
5.4 Discussion.....	95
5.5 Conclusion	100
6. Conclusion	101
6.1 Summary and Conclusions	102

6.2 Future Directions	104
Appendix	109
A. Scintillator Energy Levels.....	109
B. The Chromatic Removal Technique	111
Bibliography	116
Vita.....	127

LIST OF ILLUSTRATIONS

Figure 2.1 – Aromatic Hydrocarbons	8
Figure 2.2 – Delocalized Electron Ring.....	9
Figure 2.3 – Scintillator Energy Levels	11
Figure 2.4 – NTCP vs TCP Curves.....	19
Figure 3.1 – Temperature Dependence Experimental Setup	31
Figure 3.2 – Measured Dose vs Temperature	36
Figure 3.3 – Cerenkov Light Spectrum vs Temperature.....	38
Figure 3.4 – BCF-60 Spectrum vs Temperature.....	39
Figure 3.5 – BCF-12 Spectrum vs Temperature.....	40
Figure 3.6 – Optical Coupling Spectrum vs Temperature	42
Figure 3.7 – Total Light Intensity vs Temperature	43
Figure 3.8 – Detector Stabilization	44
Figure 4.1 – <i>In Vivo</i> Plastic Scintillation Detector Design	56
Figure 4.2 – <i>In Vivo</i> Plastic Scintillation Detector CT Image	59
Figure 4.3 – <i>In Vivo</i> Protocol Workflow Diagram	60
Figure 4.4 – Detector Localization Results.....	66
Figure 4.5 – <i>In Vivo</i> Results Histogram.....	67
Figure 4.6 – Patient Specific Results Boxplot	68
Figure 4.7 – Real-Time <i>In Vivo</i> Dosimetry Plot.....	70
Figure 4.8 – Dose Gradient Effect	73
Figure 4.9 – Protocol Patient CT Artifacts	75

Figure 5.1 – Proton Energy vs Detector Under-Response	87
Figure 5.2 – SOBP Width vs Detector Under-Response	89
Figure 5.3 –Cerenkov Light Generated in Proton Beams.....	90
Figure 5.4 – Error Introduced via Neglecting Cerenkov Light.....	92
Figure 5.5 – 225 MeV Measured Profile	93
Figure 5.6 – 140 MeV Measured Profile	94
Figure 5.7 – Bragg Peak SOBP Contribution	98
Figure B.1 – Plastic Scintillation Detector Spectral Components	112
Figure B.2 – Spectral Splitting.....	114

LIST OF TABLES

Table 4.1 – <i>In Vivo</i> Dosimetry Results	65
--	----

ABBREVIATIONS

CCD – Charge Coupled Device

CT – Computed Tomography

IMRT – Intensity Modulated Radiation Therapy

LET – Linear Energy Transfer

MOSFET – Metal Oxide Semiconductor Field Effect Transistor

MU – Monitor Unit

OSLD – Optically Stimulated Luminescent Dosimeter

PMT – Photomultiplier Tube

PSD – Plastic Scintillation Detector

ROI – Region of Interest

SNR – Signal to Noise Ratio

SOBP – Spread Out Bragg Peak

TLD – Thermoluminescent Dosimeter

TPS – Treatment Planning System

CHAPTER 1

INTRODUCTION

1.1 Purpose Statement

The primary objective of this research is to implement plastic scintillation detectors for *in vivo* dosimetry and to evaluate the practicality of doing so. *In vivo* dosimetry - direct measurement of dose delivered to patients during treatment – is a valuable tool for treating patients safely and effectively. However, its routine practice is uncommon despite evidence that it can identify treatment errors that would otherwise go undetected (Fiorino *et al.* 2000). This is due in part to the labor intensive nature of *in vivo* dosimetry and a lack of ideally suited detectors (Edwards 2007, Williams and McKenzie 2008). By demonstrating the plastic scintillation detectors are easy to use, highly accurate *in vivo* detectors, it is hoped that this research will contribute to increased adoption of *in vivo* dosimetry and enhance patient safety.

1.2 Rationale and Significance

Successful radiation therapy depends on an increasingly complicated interplay of different technologies and people including physicians, physicists, dosimetrists, and therapists. Such a complicated system will naturally be error prone if caution is not exercised, and errors can have severe consequences for patients undergoing treatment. Accordingly, numerous error checks and safety measures are routinely practiced in radiation therapy: chart checks, machine quality assurance, patient specific quality assurance, secondary dose calculations, machine interlocks and more detect and prevent errors that could compromise treatment quality or result in patient injury.

This system has been largely successful: radiation therapy is on par with other areas of medicine in terms of safety (The Royal College of Radiologists 2008). However,

some errors still avoid detection and result in inadequate or excessive dose to patients. This fact has been the focus of high profile media attention in recent years due to avoidable patient deaths and injuries resulting from treatment errors (Bogdanich 2010). While patient deaths are uncommon, the literature contains reports of incidents resulting in the systematic under- or over-dosing of large patient populations (Ash and Bates 1994, ICRP 2000, Derreumaux *et al.* 2008, WHO 2008) with adverse results. The number of such reports is increasing as incident reporting becomes mandated by regulation in more countries.

Many of the errors reported could have been identified if an *in vivo* dosimetry system was in place. In fact, in response to reported incidents some countries in Europe such as France, Sweden, and Denmark have mandated *in vivo* dosimetry in some form for all patients. *In vivo* dosimetry functions as an independent end-to-end test of treatment delivery by measuring the dose delivered to patients as they are treated. Detectors positioned in the target volume can verify that the correct treatment dose was delivered. Detectors positioned adjacent to organs at risk can verify that the dose delivered does not exceed what is planned. Gross errors can be detected rapidly and staff can intervene before patients are harmed.

Plastic scintillation detectors are in many ways ideal detectors for *in vivo* dosimetry on the basis of their distinctive collection of dosimetric properties (Beddar *et al.* 1992a, 1992b). They are capable of real-time measurement, allowing errors to be detected as they occur. They are water equivalent and very small, allowing point measurements of dose without perturbing the radiation field being measured. They suffer minimally from radiation damage, and so can be used for a long time without

recalibration or replacement. Finally, they require minimal correction factors and exhibit a high level of accuracy. Other detectors commonly used for *in vivo* dosimetry lack this comprehensive set of characteristics.

The rationale for the research presented in this work is the clear benefit of *in vivo* dosimetry coupled with the theoretical advantages of plastic scintillation detectors for *in vivo* dosimetry. Prior to this work, plastic scintillation detectors have not been used for *in vivo* dosimetry of external beam radiation. In doing so for the first time, it has been demonstrated that they are excellent *in vivo* detectors. They are capable of measuring *in vivo* dose with high accuracy and can be used without significantly altering the clinical workflow.

1.3 Specific Aims

The research performed for this work consisted of three specific aims, each dealing with a separate aspect of using plastic scintillation detectors for *in vivo* dosimetry.

The first aim was to fully characterize the unexpected temperature dependence of plastic scintillation detectors and provide accurate methods to correct for it during *in vivo* dosimetry. The effect of temperature on measured dose, total light output, and spectral shape for two common plastic scintillating fibers and their optical train components was quantified. This characterization was used to suggest a correction method and evaluate its efficacy.

The second aim was to carry out *in vivo* measurements of the rectal wall dose for a small group of prostate cancer patients undergoing intensity modulated radiation therapy, a form of external beam radiation using photons to deliver dose. The data

generated during this study was used to evaluate the performance of plastic scintillation detectors as *in vivo* detectors in terms of accuracy, precision, and practicality.

The final aim was to characterize the response of plastic scintillation detectors used for absolute entrance dosimetry in proton beams. Specifically, the effects of ionization quenching and Cerenkov light contamination were quantified and the necessity of correcting for each effect was evaluated, as well as methods to implement corrections.

1.4 Organization

The remaining five chapters of this work consist of one chapter of background information helpful in understanding the presented research, three addressing the specific aims listed in the previous section, and a final chapter summarizing the findings and discussing future directions of the presented research.

CHAPTER 2

BACKGROUND

2.1 Physical Mechanisms of Scintillation

Scintillation is the production of light by certain materials following energy deposition by ionizing particles. Scintillators are broadly categorized as organic or inorganic depending on their atomic composition and mechanism of light production (Birks 1964). For the purpose of this work only organic scintillators are considered, though inorganic scintillators have broad applications in medical imaging.

As the name suggest, organic scintillators are composed of organic molecules (carbon containing molecules), and more specifically, hydrocarbons (chains of carbon atoms bonded to hydrogen atoms). Ring shaped hydrocarbon structures known as aromatic hydrocarbons (Figure 2.1) are responsible for the luminescent properties of organic scintillators (Bross 1991).

The nature of the bonds in aromatic hydrocarbons determines their light emitting properties. In the s^3p^1 bonding configuration, each carbon atom forms three sigma bonds with two adjacent carbon atoms and a hydrogen atom, and a weak pi bond with a neighboring carbon atom. The pi bonds lie parallel to the plane of the ring, and by quantum mechanical superposition of possible pi bonding configurations, form a continuous ring within which the pi electrons from each carbon atom are free to move (Figure 2.2). The excitation and de-excitation of pi electrons within this ring is responsible for the luminescence of the molecule.

The energy levels of the pi electrons can be approximately calculated by solving the Schrödinger equation assuming the electrons are moving in an equipotential continuous circle (this assumption is known as the free perimeter electron model, the full

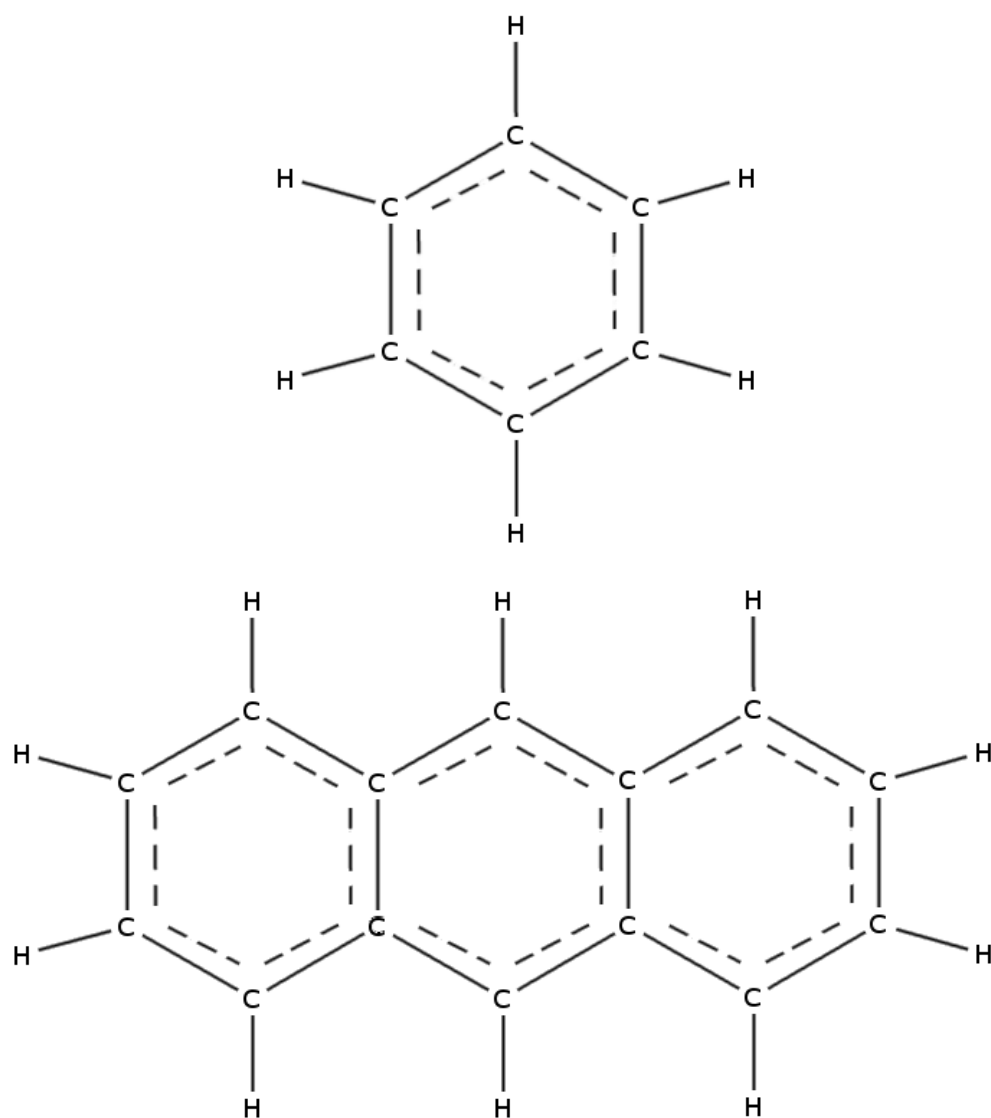


Figure 2.1. Diagram of the bonds of the aromatic hydrocarbons Benzene (top) and Anthracene (bottom), to scale. The solid lines represents sigma bonds, and the dashed lines represents the weaker pi bonds. Each ring in an aromatic hydrocarbon consists of six carbons. By definition, multiple rings may be joined together, but three rings may not be directly joined.

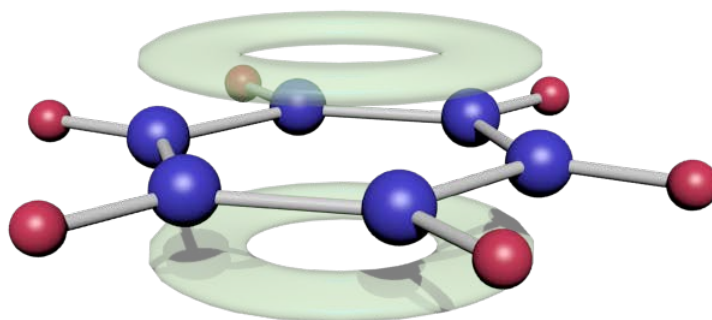


Figure 2.2. A representation of the benzene molecule with the delocalized electron rings represented as transparent green toroids. These rings are the result of the quantum superposition of all possible pi bonding configurations. The blue and red spheres are carbon and hydrogen respectively. Pi electrons, or the fourth valence electron from each carbon atom, are free to move within the rings parallel to the plane of the molecule. The resulting energy levels of these electrons are responsible for the luminescent properties of their parent molecules.

calculation is contained in section A of the appendix). This calculation reveals that the energy difference between the base state and the first excited state is on the order of a few eV, the energy of ultraviolet photons. Thus, when a pi electron is promoted to the first excited state by ionizing radiation, it can produce an ultraviolet photon as it de-excites. This process is in competition with thermal de-excitation (the excited state gives up its energy as heat rather than light), and conversion into a lower energy metastable state with a long decay time (Birks 1964). A Jablonski diagram of possible excitational states and transitions of scintillating molecules is displayed in figure 2.3.

Excitation of higher energy states is possible, but such states decay rapidly and non-radiatively to the first excited state, which then decays to the base state as described above. Other possible processes include ionization of the pi-electrons, and excitation or ionization of the sigma electrons. When sigma electrons are excited, the excess energy is dissipated as heat. Ionization of pi or sigma electrons renders the molecule incapable of scintillation. If a free electron rejoins the ionized molecule, it will regain the ability to produce scintillation light. Sometimes the ionized molecule will bond with impurities present in the scintillator material, rendering it permanently incapable of scintillation. This is the mechanism responsible for radiation damage, a loss of scintillation efficiency resulting from exposure to radiation (Birks 1964).

For the purpose of detection, photons in the visible range are desirable. To accommodate this, most scintillators are doped with secondary fluors that absorb energy from the scintillating molecules directly and emit photons of lower energy,

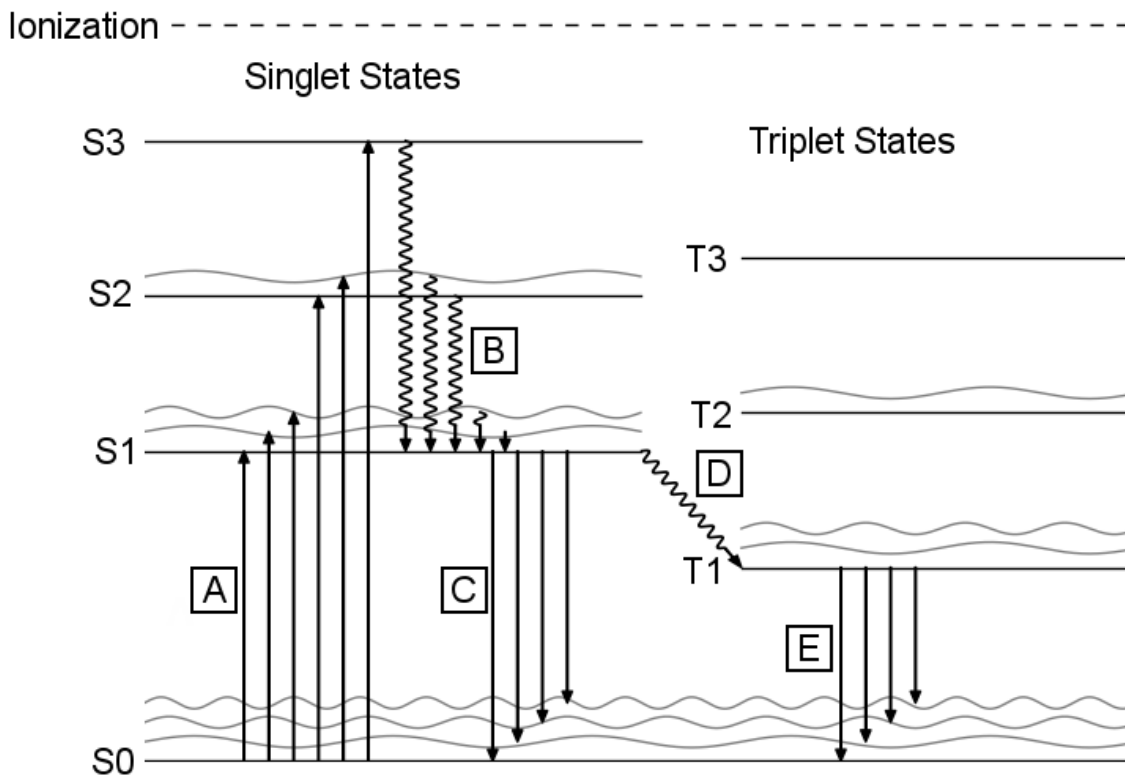


Figure 2.3. A representative diagram of the energy states of a scintillating molecule. Electronic states are represented as solid lines, and vibrational sub-levels as oscillating grey lines. Straight arrows correspond to radiative transitions, and wavy lines represent non-radiative transitions. Upon energy absorption a pi electron is promoted to one of the excited singlet states (A). Direct excitation to a triplet state is forbidden. Excitation to a state other than S1 (including the vibrational sub-levels) results in rapid decay to the S1 level, with excess energy being thermally dissipated (B). From state S1 the molecule may decay to the ground state (C), a process known as fluorescence. It may also transition to a triplet state via inversion of the pi electron's spin (D) in a process known as inter-system crossing. This process is less common than fluorescence. The first excited triplet state decays (E) on a much longer time scale, a process known as phosphorescence. Process C is responsible for scintillation light.

a phenomenon known as stokes fluorescence (Kulkarni *et al.* 1997). A third fluor may be used to further increase the wavelength of the emitted light by absorbing photons from the secondary fluor and emitting still lower energy photons. Selectively choosing the primary scintillator and the fluors allows different properties to be achieved such as specific emission wavelengths, efficiency (i.e. light produced per unit energy deposited in the scintillator), resistance to radiation damage, and more.

2.2 Design of Plastic Scintillation Detector Systems

Scintillators produce light in response to irradiation, and the light produced can be used as a measure of the dose deposited in the scintillator. This is the fundamental idea that underlies scintillation dosimetry (Beddar *et al.* 1992a, 1992b). A plastic scintillation detector system is designed to isolate and quantify scintillation light. How it does that is described in this section.

As mentioned previously, scintillation is a property of individual aromatic hydrocarbons; as a result, organic scintillators can retain their luminescent properties in solid, liquid, and gaseous states (Birks 1964). This allows the production of arbitrarily shaped plastic scintillators. Plastic scintillator can in turn be used to produce plastic scintillating fibers by the addition of a thin layer of cladding, the purpose of which is to improve light collection and transmission. Plastic scintillator and plastic scintillating fiber are easy to work with because they are chemically inert and solid. A system that uses plastic scintillator or plastic scintillating fiber for radiation dosimetry will henceforth be denoted a plastic scintillation detector system, or PSD system.

The light produced by a scintillator must be transferred to a photodetector for quantification. When used for measurement the scintillator is directly exposed to radiation, which would either damage a photodetector or render its measurements errant, so the scintillator is coupled to optical fiber to transmit the scintillation light elsewhere for quantification. To form a secure connection and maximize the transmission of light, cyanoacrylate, epoxy or other adhesive optical coupling materials are used between the scintillator and optical fiber (Ayotte *et al.* 2006). The fiber is often plastic optical fiber but the use of other fibers is reported in the literature, such as silica or air-core fibers (Beddar *et al.* 1992b, Lambert *et al.* 2008).

The scintillator and optical fiber are enclosed in opaque jacketing such as polyethylene or a similar material. This is to prevent external light from entering the system. Total light-tightness is essential, as any external light entering the system cannot be distinguished from scintillation light.

A photodetector is used to collect and quantify the light produced by the scintillator. Photomultiplier tubes (PMTs), photodiodes, charged couple device cameras (CCDs), complementary metal-oxide semiconductor cameras and other photodetecting devices may be used, so long as they accurately quantify the light produced (Beddar *et al.* 2001, Liu *et al.* 2012, Beierholm *et al.* 2014). The terminal end of the optical fiber and the photodetector are typically fitted with an optical connector, so that different optical fibers (with different scintillators) can be connected interchangeably. For this reason, the combination of a scintillator and optical fiber is denoted a plastic scintillation detector (PSD), to distinguish it from a plastic scintillation detector system which consists of one or more PSDs connected to a photodetector. Note that the PSDs of a PSD system can be

connected simultaneously or consecutively. An example of the former would be a CCD camera imaging the light produced by several PSDs at once (Archambault *et al.* 2007). The latter would be a photodiode which can only quantify the light from one PSD at a time, but the PSD can be exchanged for another between measurements (Theriault-Proulx *et al.* 2011b).

Most PSD systems require a method for discriminating Cerenkov light from scintillation light (Beddar *et al.* 1992c, Beddar *et al.* 2004). Cerenkov light is light produced by a charged particle traveling faster than the phase velocity of light in that medium. The spectral distribution of Cerenkov light is continuous and is most intense in the blue and ultraviolet regions of the spectrum. Cerenkov light produced within the scintillator itself is minimal in comparison to scintillation light, but a significant amount of Cerenkov light may be generated in plastic optical fiber used to transmit the light from the scintillator.

Various methods are used to account for Cerenkov light. The simplest method uses a second line of optical fiber without scintillator as a control. If the second line is adjacent to the first, it will generate an essentially identical amount of Cerenkov light (by virtue of being subjected to the same conditions). The signal from the control is subtracted from the PSD to isolate scintillation light (Beddar *et al.* 1992a). Another method is to use a filter to eliminate the portions of the spectrum where Cerenkov light is strongest (Clift *et al.* 2000). This works best with a scintillator that emits light at longer wavelengths: the green or red region of the visible light spectrum for example. However, there will still be a Cerenkov component at these wavelengths (Theriault-Proulx *et al.* 2011a), which prevents this method from being precisely accurate. The current favored

method is chromatic removal. In this method the light emitted from the PSD is spectrally separated into two components (using a dichroic mirror for example). The relative intensities of the two components are used to mathematically extract the scintillation (Fontebonne *et al.* 2002, Frelin *et al.* 2005, Archambault *et al.* 2006). Further explanation of this technique is available in part B of the appendix.

Finally, calibration is necessary to establish a relationship between the scintillation light and dose. When using the chromatic removal technique, calibration consists of subjecting a PSD to well-known doses under two or more different conditions. Two conditions are considered different if the ratio of scintillation to Cerenkov light changes between them. This is most easily accomplished by increasing the quantity of exposed optical fiber. Using equation 2.1, a pair of calibration factors that convert PSD signal to dose can be recovered from the calibration measurements.

$$\mathbf{F} = \mathbf{S}^+ \mathbf{D} \quad (2.1)$$

In this equation, \mathbf{D} is a Nx1 matrix of known doses, \mathbf{S}^+ is the inverse of the Nx2 matrix of signals from the PSD (Nx2 rather than Nx1 because the light is split into two channels for each measurement, as explained in the previous paragraph), and \mathbf{F} is the resulting 2x1 matrix of calibration factors. In the case that the matrix \mathbf{S} is not square, the Moore-Penrose pseudoinverse is used instead of the true inverse. Once the calibration factors are determined, the dose corresponding to a given PSD measurement can be determined with equation 2.2.

$$D = \mathbf{S} \mathbf{F} \quad (2.2)$$

\mathbf{S} is a 1x2 matrix of the PSD signals, \mathbf{F} is a 2x1 matrix of the calibration factors, and D is a scalar corresponding to the dose.

In the case that chromatic removal is not used, calibration consists simply of determining the ratio of dose to signal under known conditions. This ratio would then be multiplied with the measured signal to determine dose.

2.3 Dosimetric Properties of Plastic Scintillation Detectors

With the theory underlying the design of a plastic scintillation detector presented, the practical properties of such a detector as relates to dosimetry will now be explored.

As mentioned earlier, PSDs are composed of hydrocarbons. Because of this, their composition is very similar to tissue and water. Polystyrene for example, the main component of plastic scintillating fiber, has a density of 1.060 g/cc, just 6% higher than water. It has an electron density of 3.238×10^{23} e-/g, 3% below water. The mass collision stopping power and mass angular scattering power are very similar to that of water over a broad range of energies (Beddar *et al.* 1992a). Radiation therefore interacts with PSDs as it would with water or tissue. As a result, no correction factor is needed to convert from the dose deposited in the detector to the dose that would be deposited in water. Furthermore, charged particle equilibrium is not necessary for accurate dosimetry with a PSD, unlike with an ion chamber.

PSDs are energy independent above a threshold of approximately 200 keV (Beddar *et al.* 1992a, Beddar *et al.* 2005). This is due both to water equivalence and the fact that the light yield of plastic scintillator is linear with the energy of charged particles interacting with the scintillator (Brannen and Olde 1962). This allows the use of PSDs in radiation beams of different energies (photon or electron) or at different depths without factors to account for changes in the beam's energy distribution.

Another important property of PSDs is that the light produced by a PSD is linear with the quantity of dose deposited (Beddar *et al.* 1992b). Thus a doubling of scintillation light corresponds exactly to a doubling of dose deposited in the scintillator. This makes measurement simpler in comparison to mediums like film that respond non-linearly to the dose deposited. A closely related property is dose rate independence. The production of light in a PSD is a linear function of dose rate. If dose is deposited twice as quickly, light will be produced twice as quickly as well.

The PSD response is independent of the orientation of the detector relative to the radiation field (Wang *et al.* 2010). Scintillation light is emitted isotropically (that is, photons are emitted from the scintillating molecules with equal probability in all directions), which is responsible for this property. As such, there is no need to take into account the orientation of the PSD when performing measurements.

PSDs possess exceptional spatial resolution depending on the size of scintillator or scintillating fiber used. 1 mm and 0.5 mm diameter scintillating fibers are common. The length of fiber used is more variable, but 2 mm is a reasonable representative value. This corresponds to an active volume of approximately 1.6×10^{-3} cubic centimeters (for a 1 mm diameter fiber). This makes PSDs ideal for measuring small fields or in steep dose gradients where volume averaging is a concern (Beddar *et al.* 2001).

PSDs are capable of real time dosimetry because the decay rate from an organic scintillator's first excited state to the base state is on the order of nanoseconds. The limiting factor in temporal resolution is typically the photodetector (for example, CCD cameras have a minimum exposure length that is orders of magnitude longer than the

decay rate of the scintillator). Real time dosimetry provides time-resolved detail of the delivered radiation (Archambault *et al.* 2010).

Finally, scintillators convert absorbed dose to light with high efficiency. Thus even with a small active volume, a high signal is produced in response to small amounts of dose. As a result PSDs are highly precise detectors (Lacroix *et al.* 2009).

2.4 *In Vivo* Dosimetry

The dosimetric properties of PSDs make many useful applications possible such as small field dosimetry (Beddar *et al.* 2001, Klein *et al.* 2010), quality assurance (Gagnon *et al.* 2012), and *in vivo* dosimetry. Among these applications, *in vivo* dosimetry has attracted great interest. The benefits of *in vivo* dosimetry will be laid out in the rest of this section.

In vivo dosimetry is of interest primarily for its potential to improve patient safety and verify correct delivery of treatment. Patient safety is imperative in radiation therapy. Patients are exposed to high levels of radiation and both over- and under-exposure can have severe consequences as illustrated in figure 2.4. These consequences have been highlighted by recently reported accidents. In Panama 28 patients received excessive dose during treatment between August 2000 and March 2001 due to an error in the way the treatment planning system digitized shielding blocks. Eight of the patients subsequently died, with five deaths attributed to the overdose. The remaining patients were expected to develop complications (IAEA 2001). In Glasgow in 2006, human error induced by a change in the way dose was specified resulted in a medulloblastoma patient receiving 55 Gy in 19 fractions instead of the intended 35 Gy in 20 fractions. This overdose eventually

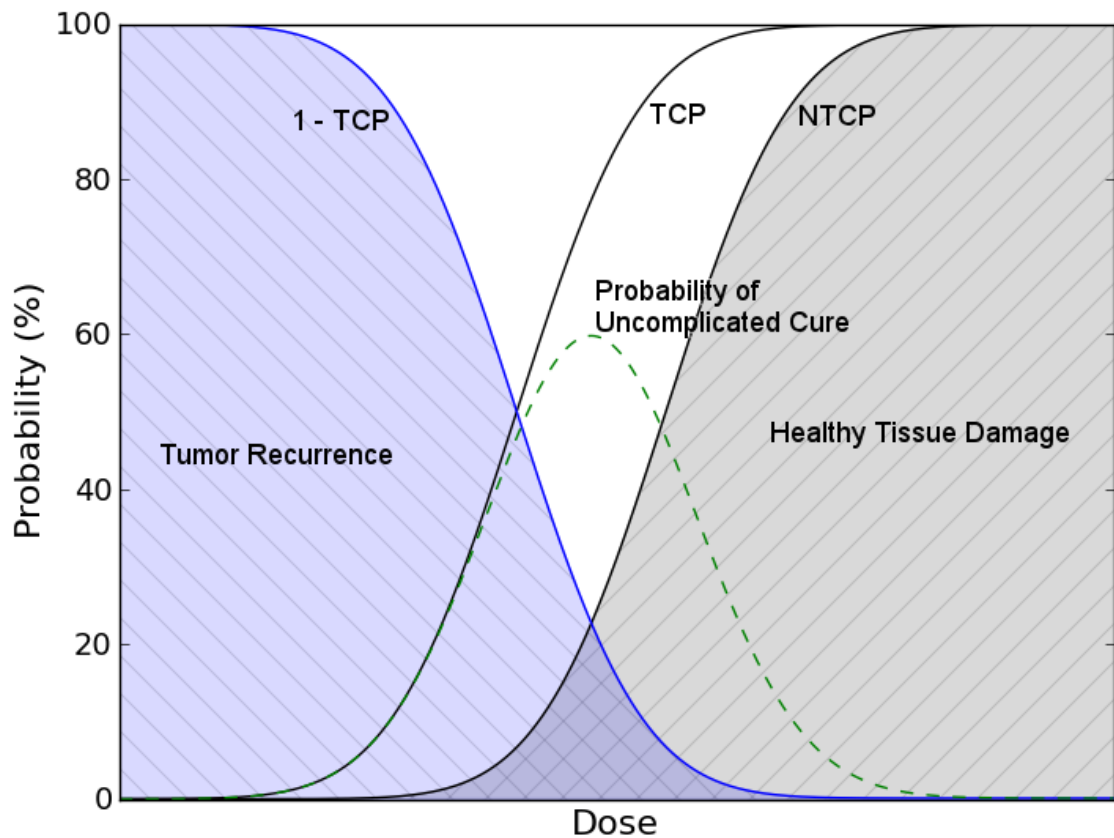


Figure 2.4. Hypothetical tumor cure probability (TCP) curve and normal tissue complication probability (NTCP) are plotted in black. Successful radiation therapy maximizes the difference between the tumor cure probability and normal tissue complication probability to achieve the highest likelihood of uncomplicated cure (green dashed curve). The likelihood of tumor recurrence is plotted in blue to illustrate that deviation from the optimal dose in either direction can significantly increase the likelihood of either recurrence (caused by under-dose) or healthy tissue damage (caused by over-dose).

resulted in the patient's death (Mayles 2007). Some errors are less severe but affect far more patients. For example, at a French center between 2001 and 2006, 397 patients received 8% overdoses because the dose resulting from MV portal imaging was not included in planning. No patients died, but the population exhibited an abnormally high rate of radiation induced complications (Derreumaux *et al.* 2008). In each of these cases, *in vivo* dosimetry could have detected errors early in the course of treatment, sparing patients undue injury through timely corrective action.

In vivo dosimetry also has the potential to improve the patient experience. The promulgation of reports of radiation therapy accidents by the media produce anxiety in some patients undergoing treatment (The Royal College of Radiologists 2008). *In vivo* dosimetry can reassure patients that errors will be caught and mitigated if they occur, and bolster the patient's confidence in the clinic. Thus, the perceived quality of care is improved even when no deviations in treatment occur.

Another motivation to adopt *in vivo* dosimetry is that it may be legally required in the future. Some European governments have begun mandating *in vivo* dosimetry in response to accidents similar to those cited above. It is required by law in France, Sweden, and Denmark. The National Health Service in Britain recommended in 2008 that routine *in vivo* dosimetry be implemented for all patients undergoing radiation therapy. While *in vivo* dosimetry is not required on a routine basis in America, it is reasonable to assume regulation could move in that direction in the future.

Finally, *in vivo* dosimetry is of scientific interest as well, because it generates data useful for toxicity studies. Tumor control probabilities and normal tissue risks are evaluated by correlating outcomes with planned doses as calculated by a treatment

planning system (TPS). While TPSs generally do an excellent job of accurately calculating dose distributions, the TPS calculated dose cannot account for day to day variations in setup and other external factors that affect the delivered dose distribution. *In vivo* dosimetry can be used to evaluate such effects, and may therefore be useful when used in conjunction with TPS calculated dose for evaluating toxicity risks.

2.5 Challenges of *In Vivo* Dosimetry

The potential benefits of *in vivo* dosimetry are clear, but its routine practice is rare. When *in vivo* dosimetry is performed, it is largely limited to special circumstances such as total body irradiation (to identify areas receiving too little radiation for local boosts), the treatment of pregnant patients, or the treatment of patients with implantable cardiac devices. A large majority of radiation therapy patients do not receive *in vivo* dosimetry in any form. In light of the clear benefits, it is obvious that there are obstacles to implementing *in vivo* dosimetry. The main obstacle is the labor intensive nature of *in vivo* dosimetry relative to the perceived benefits.

The feasibility of implementing routine *in vivo* dosimetry has been much debated in the literature lately (Harrison and Morgan 2007, Williams and McKenzie 2008). Routine *in vivo* dosimetry would be costly, primarily in terms of the time required of staff to properly implement it (Edwards *et al.* 2007, Munro 2007). This includes the time required to prepare detectors, the time required to perform the measurements, and the time to analyze the data. Given that data from countries where misadministration reporting is mandatory indicates that severe incidents are rare (The Royal College of Radiologists 2008), the cost of preventing one major incident is potentially huge.

A significant portion of the resistance to *in vivo* dosimetry stems from the fact that detectors typically used for *in vivo* dosimetry have a variety of drawbacks that either make their use labor intensive and/or limit their usefulness (Mijnheer *et al.* 2013). An ideal detector should be largely independent of the need for correction factors so it will be easy to use. Real-time feedback is highly desirable in order to detect treatment deviations as soon as possible to mitigate any harm done. Finally, an ideal detector should not need to be replaced or recalibrated often in the interest of time. The detectors that are commonly used for *in vivo* dosimetry do not meet all of these requirements. Thermoluminescent dosimeters (TLDs) and optically stimulated luminescent detectors (OSLDs) cannot be used for real time measurement (and will therefore detect problems well after they occur), they require a number of correction factors to achieve high accuracy, can only be read out with expensive dedicated machinery, and are labor intensive (DeWerd *et al.* 2009). Diodes are capable of real time dosimetry with high spatial resolution, but are sensitive to a number of conditions such as energy, orientation, and temperature, and exhibit a significant loss of signal over time due to radiation damage (Saini and Zhu 2007a, 2007b). MOSFETS are similar to diodes in that they are capable of real time operation, but are sensitive to energy, orientation, temperature and generally have shorter useful lifetimes than diodes (Jornet *et al.* 2004, IAEA 2013). The shorter lifetime is a particularly limiting factor as the continual calibration of new detectors requires a significant time investment.

2.6 Plastic Scintillation Detectors for *In Vivo* Dosimetry

Plastic scintillation detectors are good candidates to address the challenges cited above. As described previously, PSDs possess an array of unique dosimetric characteristics that fit the profile of an ideal *in vivo* detector well. The most notable characteristics of PSDs with regards to *in vivo* dosimetry are their water equivalence; a response independent of energy, dose rate, and other factors; a high ratio of signal to dose; a response time on the order of nanoseconds; and a low cost. The benefits of each characteristic in the context of *in vivo* dosimetry are examined in this section.

Water equivalence is a highly desirable characteristic for *in vivo* dosimetry. It allows the dose to tissue to be measured directly without the use of a conversion factor. Additionally, water equivalence ensures that detectors do not perturb the radiation field being measured. Accordingly, a PSD can be placed in the center of a treatment field in a patient without compromising the treatment. A final benefit of water equivalence is that it allows the use of PSDs in very small fields, such as those encountered in radiosurgery, without the need for correction factors due to a loss of lateral electronic equilibrium or source occlusion.

PSDs can measure dose with great accuracy in part due to a response independent of factors such as energy, dose rate, and angle of incidence. The effect of such factors will sometimes be difficult to determine and correct *in vivo*, even if they are well characterized *ex vivo*. Furthermore, any correction will necessarily involve some uncertainty which will contribute to the overall uncertainty of the detector. Therefore a minimal need for correction factors when using PSDs is an important advantage.

The high signal and nanosecond response time of PSDs makes real-time dose monitoring feasible. The fast response time eliminates blurring of the measured dose profile in time. The high signal allows a PSD system to maintain a reasonable signal to noise ratio (SNR) even when measuring in the short time intervals with commensurately small doses. Real-time dosimetry is essential if one wishes to be able to detect errors as they occur in order to interrupt treatment and rectify the situation. Temporal information can also be useful when investigating errors. For example, treatment can be investigated on a beam-by-beam basis.

Finally, PSDs are more resistant to radiation damage than other available detectors. As such they may be reused for long periods of time without replacement or recalibration, saving time and money (Beddar *et al.* 1992a).

Like any detector, PSDs do have a few unfavorable characteristics. First, some PSDs exhibit temperature dependence (Wootton and Beddar 2013, Buranurak *et al.* 2013), a fact unknown before the work presented in chapter 3 was performed. This subject will be covered in depth in that chapter. By way of a brief overview however, the signal of BCF-60, a common scintillating fiber used in PSDs, exhibits as much as an 8% decrease in measured dose at body temperature relative to room temperature. Clearly this must be corrected for to perform accurate *in vivo* dosimetry. The stem effect (non-scintillation signal in the form of Cerenkov light), is another drawback. However, this can be overcome with the highly effective chromatic removal technique.

Overall, PSDs compare favorably with other detectors commonly in use for *in vivo* dosimetry. Their size is equal to or smaller than diodes and MOSFETS. They do not require build up or correction for factors such as energy, angle, or dose rate. They are far

more radiation resistant than either MOSFETs or diodes, giving them a comparatively longer lifetime and requiring less time for calibration. Finally, they are capable of real time dosimetry.

CHAPTER 3

TEMPERATURE DEPENDENCE OF PLASTIC SCINTILLATION DETECTORS

This chapter is based on material published by the author of this dissertation in Physics in Medicine and Biology in 2013:[Wootton LS and Beddar AS 2013 Temperature dependence of BCF plastic scintillation detectors. Phys. Med. Biol. 58 2955-67]. It is reproduced here with permission of IOP Publishing. Wording in the introduction and discussion has been modified to conform to the overall style of this dissertation.

3.1 Introduction

The plastic scintillation detector (PSD) is a thoroughly studied detector notable for a unique collection of characteristics that make it well suited for dosimetry. For example, previous studies have established that PSDs are water equivalent; exhibit a linear relationship between scintillation light and deposited dose; are energy, dose rate, and angularly independent; have a high spatial resolution; and are temperature independent (Beddar *et al.* 1992a, 1992b). Some of these characteristics, most notably temperature independence, have been accepted as fact without independent validation by other groups.

Twenty years have passed since the initial studies were conducted that established these characteristics, and the design and construction of PSDs has changed in that time. Specifically, the first PSD described in the published literature was constructed with a BC-400 scintillator coupled to a silica light guide using silicon optical coupling grease (Beddar *et al.* 1992a). It is now not uncommon to use different materials; SCSF-3HF(1500), SCSF-78, BCF-12, and BCF-60 scintillating fibers often replace BC-400 owing to their superior light collection and/or spectral properties. Plastic optical fibers are commonly substituted in place of the silica light guide to achieve better water

equivalence. Cyanoacrylate or epoxies are regularly used for optical coupling (Archambault *et al.* 2005, Ayotte *et al.* 2006).

New generations of PSDs have been shown to possess almost all of the dosimetric characteristics of the original PSDs from the 1992 study, including response linearity, water equivalence, and energy, dose rate, and angular independence, as evidenced by their successful use in increasingly advanced dosimetric studies (Archambault *et al.* 2010, Klein *et al.* 2010, 2012, Lacroix *et al.* 2010, Wang *et al.* 2012). However, to the best of our knowledge, temperature independence has not been independently validated or investigated for either the original PSD or any subsequent generations of PSDs.

We were prompted to investigate temperature dependence in response to a systematic error exhibited by PSDs employed in an *in-vivo* dosimetry protocol (the subject of chapter 4) at our institution. These PSDs were regularly subjected to both *in-vivo* dose measurements in patients and in-phantom validation designed to replicate the *in-vivo* conditions. The dose measured by the PSDs in the phantom agreed excellently with the calculated dose in the treatment planning system; however, the dose measured *in-vivo* differed from that calculated by the treatment plan. Because the phantom was at room temperature during validation, we concluded that temperature dependence was an important avenue of investigation.

A brief initial investigation, reported in a letter to the editor previously (Beddar 2012), confirmed that the PSDs did indeed exhibit temperature dependence. This investigation indicated that the measured dose decreased by an average of 0.6% per C increase, relative to room temperature, for PSDs made with BCF-60 scintillating fibers. This prompted us to conduct a more thorough systematic investigation of the effects of

temperature on PSDs built with BCF-12 and BCF-60 scintillating fibers, which are two of the most common scintillating fibers used in PSDs. In this article, we present our investigation and report the results.

3.2 Methods and Materials

3.2.1 Detectors

The PSDs used for this study were constructed according to the following method. A 2-mm length of either BCF-60 or BCF-12 scintillating fiber (Saint-Gobain Crystals, Hiram, OH) was optically coupled to an Eska GH-4001-P clear plastic optical fiber (Mitsubishi Rayon Corporation, Japan) with cyanoacrylate glue. The abutting ends of the scintillating fiber and the optical fiber were polished with fine grit polishing paper to facilitate high optical transmission efficiency (Ayotte *et al.* 2006). The entire assembly was light-shielded in black polyethylene jacketing. Additionally, an opaque, black, alcohol-based adhesive was used to conceal exposed portions of scintillating fiber and optical fiber (e.g. at the end of the PSD where the scintillating fiber terminated) to prevent the admission of external light that would contaminate the PSD signal. Approximately 20 m of optical fiber was used to span the distance between the linac and the outside of the vault. The optical fiber was connected either to a Luca S CCD Camera (Andor Technology, Belfast, Northern Ireland) via a ST optical connector for dose measurements or to an Andor Shamrock 163 spectrometer via a SMA optical connector for spectral analysis. The connectors ensured a secure and reproducible connection.

Calibration was performed under cobalt-60 irradiation using the chromatic removal technique (Fontebonne *et al.* 2002, Frelin *et al.* 2005, Archambault *et al.* 2006)

to distinguish scintillation light from contaminating Cerenkov light (Beddar *et al.* 1992c). In order to implement this technique, a dichroic mirror (model NT47-950, Edmund Optics Inc., Barrington, NJ) was used to split the light produced by the PSDs into 2 spectrums prior to imaging by the CCD.

3.2.2 *Experimental Setup*

To subject PSDs to a variety of stable temperatures, PSDs were placed into a 250-mL beaker filled with water that was placed on top of a hotplate. A cap of dense blue Styrofoam was fashioned to fit tightly into the top of the beaker to insulate the water, and small perforations in the Styrofoam cap allowed the PSDs access to the water. A thermometer was also inserted through the center of the Styrofoam cap into the water to monitor the temperature. The bulb of the thermometer was placed at the same depth as the active volume of the PSDs to provide the most accurate assessment of the PSD temperatures.

The hotplate (model PC-620D; Corning Incorporated, Corning, NY) included a magnetic stirring device which was used to facilitate a homogeneous temperature distribution of the water. The hotplate was placed on a lateral edge of a linac couch. The gantry head was rotated to 270 degrees to position the beam perpendicularly to the PSDs, and the couch was then moved laterally as close to the linac head as possible to maximize the signal from the PSDs (Figure 3.1).

Prior to obtaining each set of measurements, we filled the beaker with a combination of water and crushed ice. The cap with the PSDs and thermometer was then

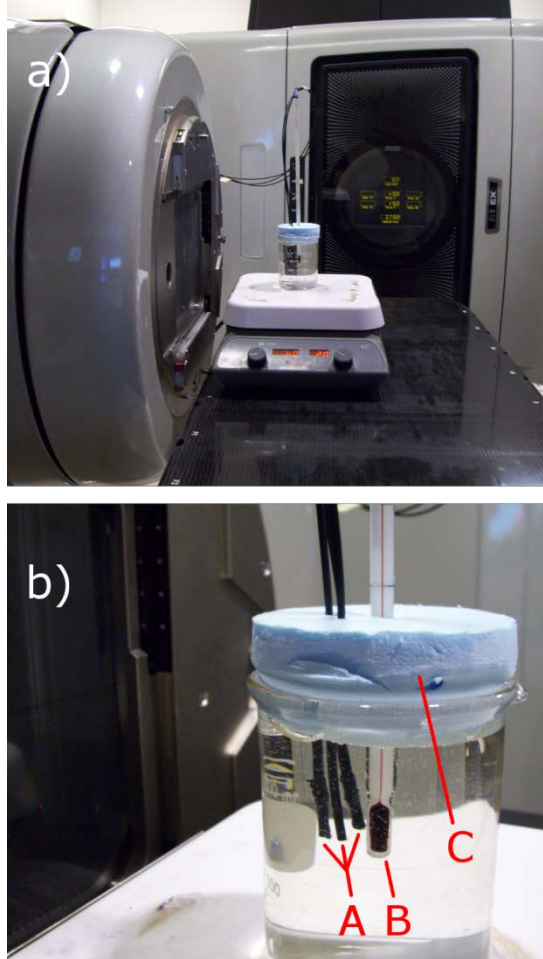


Figure 3.1. Experimental setup. a) The gantry was rotated to irradiate the plastic scintillation detectors (PSDs) perpendicularly and the couch was shifted laterally to maximize the signal from the PSDs by placing them as close as possible to the radiation source. A beaker of water was placed on the center of a hotplate to position it above a magnetic stirrer, and the PSDs and a thermometer were held in place in the beaker by a Styrofoam cap. The optical fiber transmitting scintillation light was taped to the linac to prevent motion in and out of the field, which would alter the Cerenkov contribution to the PSD signal. b) Three PSDs (one for spectrometry and two for dose measurements, label A) were inserted through the Styrofoam cap (label C) into the water. The bulb of the thermometer (label B) was placed near the active volume of the PSDs to provide the most accurate assessment of the PSD temperatures.

affixed to the top of the beaker, and the stirrer used to bring the water to thermal equilibrium. The beaker was filled completely with water, so that no air gap was present between the water and the bottom of the Styrofoam cap.

Each data point was acquired using the following protocol. First, the hotplate setting was adjusted to bring the water to the desired temperature. After the temperature stabilized but before the irradiation, the water temperature was held constant for an additional 10 minutes to allow the PSDs to come to thermal equilibrium with the water. Although less time was likely required (the jacketing consisted of polyethylene, the scintillator of polystyrene, and the optical fiber of PMMA, each of which have a thermal conductivity similar to water), 10 minutes was chosen to ensure that the water temperature measured by the thermometer accurately reflected the PSD temperature. After this waiting time, the detectors were irradiated with 100 monitor units (MU) 3 times, for statistical purposes, and the output was captured with either the CCD or the spectrometer as described below.

It was not possible to stabilize the water temperature below room temperature; no means of cooling the setup without disturbing it were available. Therefore, for these measurements, we averaged the temperature measured before and after the irradiation (typically differing by 0.5°C) and assumed that this accurately reflected the PSD temperature.

3.2.3 Dose Measurements

Dose was measured with a pair of BCF-60 PSDs and a pair of BCF-12 PSDs to quantify the effect of temperature on measured dose. Measurements spanned a range from

approximately 15°C to 40°C. Twenty-second CCD light-integrating acquisitions were used to measure the light output resulting from each 100 MU irradiation. An average background image was subtracted from the measurement images, from which dose values were subsequently obtained via analysis in ImageJ (Archambault *et al.* 2008). The resulting dose values were normalized to the dose measured at room temperature, here defined as 22°C. If no measurement was made at 22°C, the value was obtained by interpolating between the 2 closest points.

3.2.4 Spectrometry

The effect of temperature on the intensity and spectral distribution of light of 4 different PSD configurations was quantified with a spectrometer. The following PSD configurations were used: a PSD built with BCF-60 scintillating fiber, a PSD built with BCF-12 scintillating fiber, a bare fiber (i.e. an optical fiber without a scintillating element or cyanoacrylate, thus capable only of generating Cerenkov light), and a PSD with an isolated cyanoacrylate optical coupling.

For measurements involving the bare fiber, only the submerged portion of the fiber that was subject to temperature changes was irradiated. This was done to ensure that any temperature dependence of the production and transmission of Cerenkov light would not be masked by Cerenkov generated elsewhere in the optical fiber.

To create an isolated optical coupling, the optical fiber of a BCF-60 PSD was cut 2 m below the scintillating element and reattached with cyanoacrylate. More cyanoacrylate than would typically be used in the fabrication of a PSD was employed to exaggerate any effects. Only this optical coupling was submerged in the water and

subjected to temperature changes, while the scintillating element of the PSD was maintained at room temperature outside of the beaker and irradiated to generate a light signal that would be transmitted through the isolated coupling.

Twenty-second acquisitions were used for each 100-MU irradiation. An average background spectrum was subtracted from each measurement. To distinguish between the Cerenkov light and the scintillation contributions to the spectral measurements, a pure Cerenkov spectrum and a pure BCF-60 or BCF-12 scintillation spectrum were fitted to the total spectral output at room temperature for each configuration using the least squares method. The fitted Cerenkov spectrum was then subtracted from measurements at other temperatures, leaving only the scintillation spectra (the Cerenkov spectrum was demonstrated to be unchanged by changing temperature). The fitted room temperature Cerenkov spectrum needed to be subtracted at non-room temperatures because fitting the pure scintillation spectrum would not correctly determine the scintillation signal if the spectral distribution of the scintillator was temperature dependent. The pure Cerenkov spectrum was obtained from the bare fiber. The pure scintillation spectra were obtained at room temperature by irradiating the scintillators on a kV irradiation unit; the low-energy radiation of the kV irradiator produces a negligible amount of Cerenkov light (Therriault-Proulx *et al.* 2012).

The spectra of each PSD configuration were analyzed to determine the wavelength at which the maximum intensity change occurred and the magnitude of that change, the change in the total intensity of the spectrum, and the change in the distribution of the spectrum. As a metric to quantify the change in the distribution, we calculated the ratio of the change in intensity of the portion of the spectrum that would be

reflected by the dichroic mirror used in our CCD setup (520-550 nm) to the change in intensity of the portion that would be transmitted by it (the remaining visible spectrum).

3.2.5 Detector Stabilization

An additional experiment was performed to determine whether the temperature-dependent response of the PSDs at non-room-temperatures stabilized, and if so, how quickly. The water-filled beaker was heated to 29°C while a BCF-60 PSD was maintained at room temperature outside the beaker. After the water temperature stabilized at 29°C, the PSD was inserted through the Styrofoam cap and measurements of 100-MU irradiations were immediately commenced at a frequency of 1 per minute for 40 minutes. The first measurement was made approximately 50 seconds after introducing the PSD into the beaker. This delay was necessary to exit the room and close the vault door.

For comparison, these measurements were repeated in air (i.e., the beaker was not filled with water) and without the application of heat. This was done to eliminate the possibility that changes in output were due to other effects such as fatigue of the CCD camera.

3.3 Results

3.3.1 Dose Measurements

The measured dose for each pair of PSDs decreased with increasing temperature across the entire temperature range (Figure 3.2). The relationship between the BCF-60 PSD measured dose and temperature was predominantly linear, although a small nonlinear

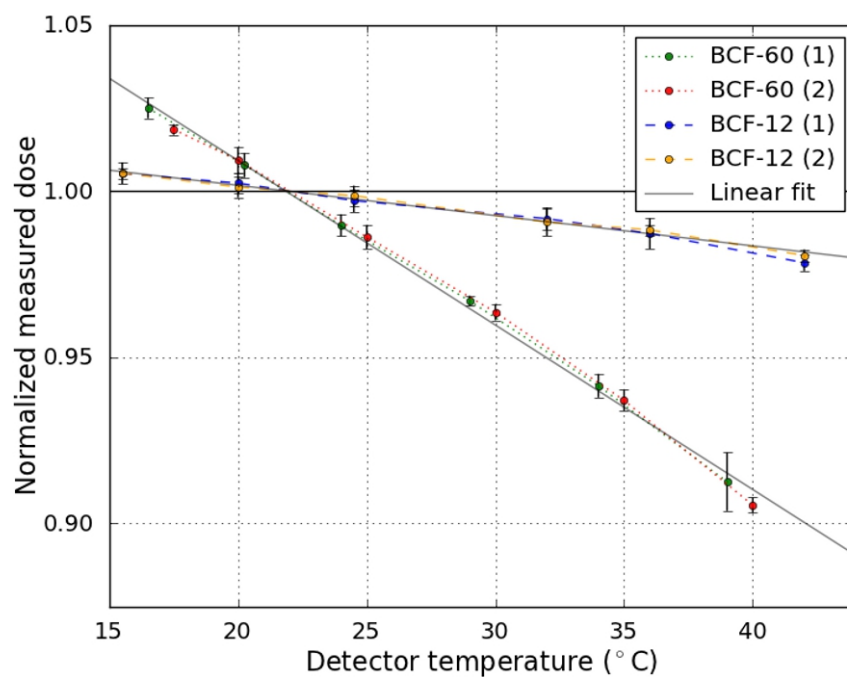


Figure 3.2. Dose measurements obtained under changing temperature conditions from 2 pairs of plastic scintillation detectors made with BCF-12 and BCF-60 scintillating fibers. A steady decrease in the measured dose was observed with increasing temperatures. Each point is the average of 3 measurements, and the error bars represent 2 standard deviations of those measurements. Linear fits show that BCF-60 exhibited slightly nonlinear temperature dependence, whereas the BCF-12 temperature dependence pattern was entirely linear.

component was present. The measured dose for the BCF-60 PSD decreased by approximately 0.50% per °C increase relative to room temperature. The relationship between the BCF-12 PSD measured dose and temperature was linear, with the measured dose decreasing by 0.09% per °C increase.

3.3.2 Spectrometry

Spectrometry data for irradiation of the bare fiber revealed that neither the total intensity nor the distribution of the Cerenkov spectrum changed as a function of temperature (Figure 3.3).

However, considerable change in the intensity of the BCF-60 PSD output was observed for wavelengths between 475 nm and 650 nm, with no discernible change in output outside of that range (Figure 3.4). Between 475 nm and 650 nm, the maximum intensity loss occurred at 510 nm and was equal to 0.60% per °C relative to room temperature. The total light output of the BCF-60 PSD decreased at a rate of 0.32% per °C in a dominantly linear fashion, with a small nonlinear component. The portion of the spectrum that would be reflected by the dichroic filter decreased in intensity at a rate of 0.59% per °C increase, whereas the rest of the spectrum intensity decreased at a rate of only 0.43% per °C increase, a ratio of 1.37 (i.e., the reflected portion decreased in intensity 37% more rapidly than the rest of the spectrum).

A markedly less severe loss of intensity was observed in the spectrum of the BCF-12 PSD, this time constrained to the regions between 375 nm and 500 nm (Figure 3.5). The maximum intensity loss occurred at approximately 410 nm: a 0.30% decrease per °C

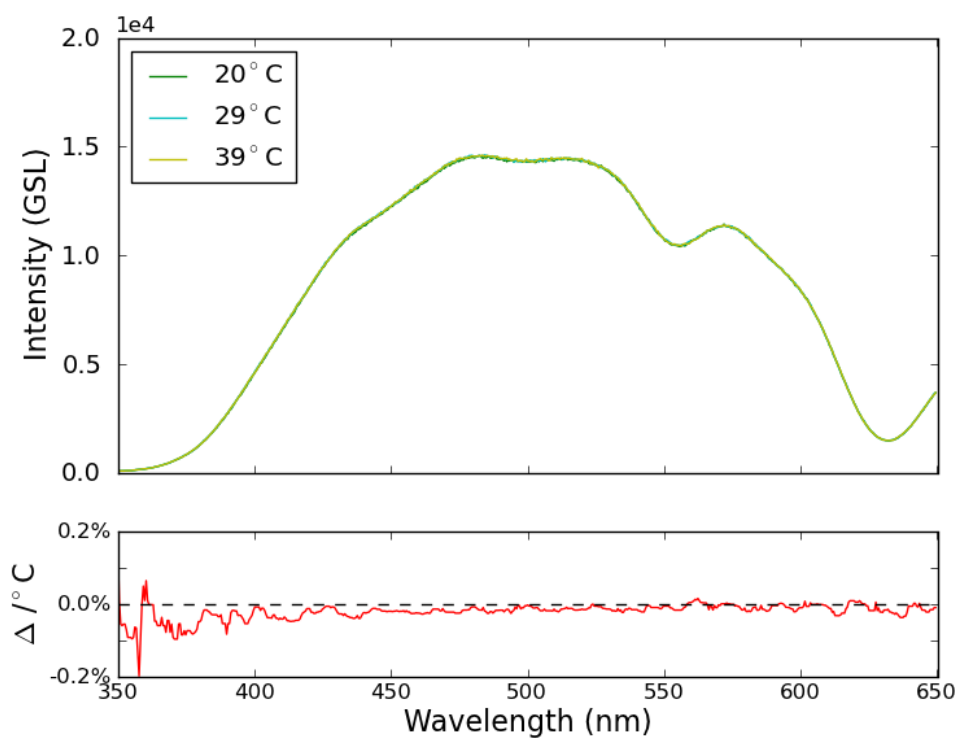


Figure 3.3. Cerenkov spectra. In the top plot, the intensity vs. wavelength of the Cerenkov spectrum is displayed for a staggered selection of temperatures. The bottom plot displays the percent change in the spectrum per $^\circ\text{C}$ as a function of wavelength relative to the 20°C spectrum. The shape and intensity of the Cerenkov spectrum did not change discernibly with rising temperatures. Note that the two plots share the same x-axis.

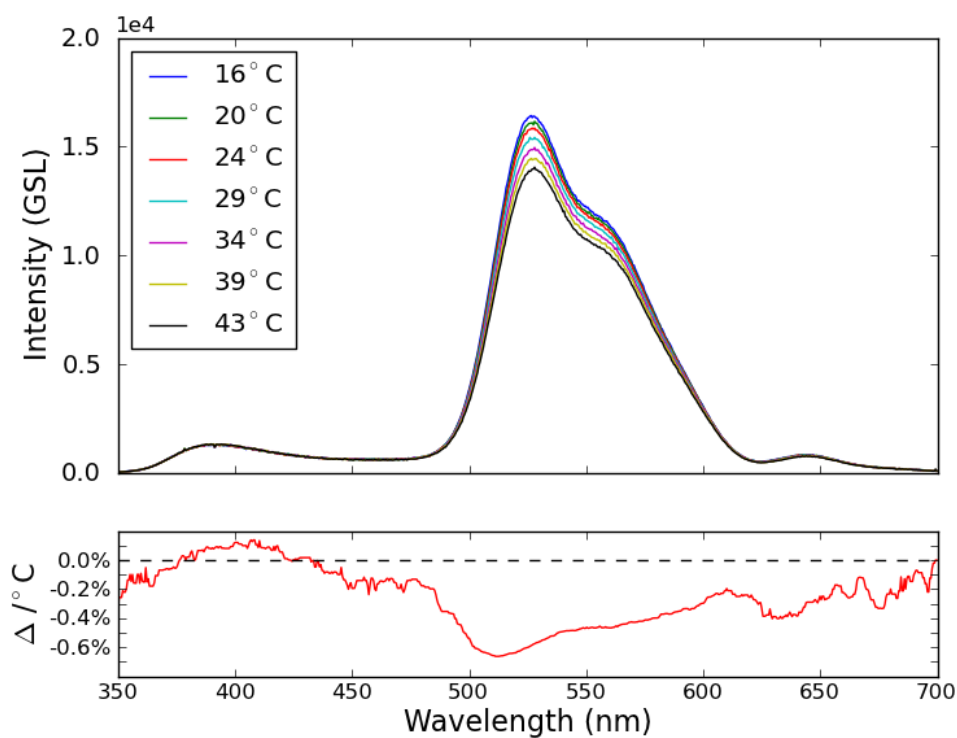


Figure 3.4. BCF-60 spectra. In the top plot, the BCF-60 spectrum is displayed for a range of temperatures. The bottom plot displays the percent change in the spectrum per °C as a function of wavelength, relative to the 20°C spectrum. The spectrum intensity decreased substantially between 475 nm and 600 nm. A small decrease is observed from 600 nm to 650 nm. It is difficult to evaluate the change outside of this range due to a poor signal to noise ratio (SNR), but it appears negligible. Note that the two plots share the same x-axis.

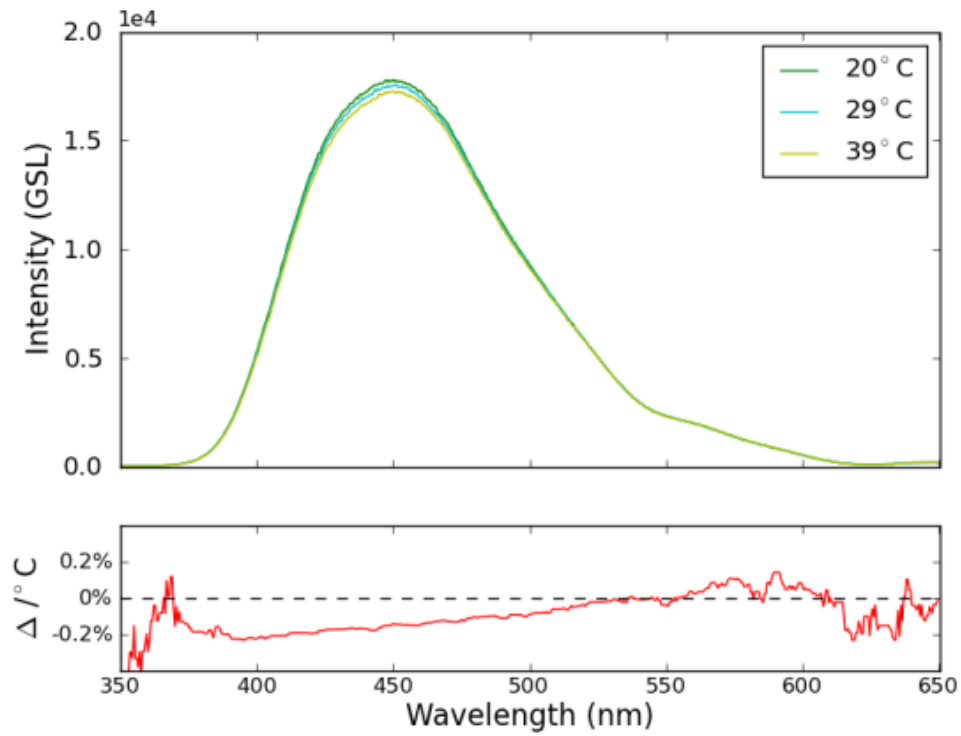


Figure 3.5. BCF-12 spectra. In the top plot, the BCF-12 spectrum is displayed for a staggered selection of temperatures. The bottom plot displays the percent change in the spectrum per °C as a function of wavelength, relative to the 20°C spectrum. The spectrum intensity decreased slightly between 375 nm and 500 nm. Outside of this range no change is observed, though the low SNR makes it difficult to evaluate. Note that the two plots share the same x-axis.

increase relative to room temperature. The total light output of the BCF-12 PSD decreased by 0.13% per °C in a linear fashion. The intensity of the portion of the spectrum corresponding to light reflected by the dichroic filter decreased at a rate of 0.02% per °C, whereas the intensity of the remaining spectrum decreased at a rate of 0.12% per °C, a ratio of 0.13.

For the cyanoacrylate coupling, a nonlinear decrease in transmitted light was observed with increasing temperature. Note that because the change was nonlinear, all values presented are the difference between the intensity at 38°C and 22°C. Intensity loss occurred primarily between 500 nm and 600 nm (Figure 3.6). The maximum intensity loss of 4.2% occurred at 550 nm. A 2.5% loss in total light intensity was observed. The intensity of the reflected portion of the spectrum decreased by 3.6%, whereas the intensity of the remaining spectrum decreased by only 2.5%, a ratio of 1.4.

The total light output for each PSD configuration is plotted in figure 3.7.

3.3.3 Detector Stabilization

All measurements made with the PSD maintained at 29°C were within 0.50% of the average measured value. The measurements did increase very slightly over the course of the experiment; at the conclusion of the experiment it was noted that the water temperature had decreased by 1.5°C, which accounted for the increase in the measured values.

When the experiment was repeated in air, all measured values fell within approximately 0.50% of the average measured value, and no trend was observed. These results are displayed in figure 3.8.

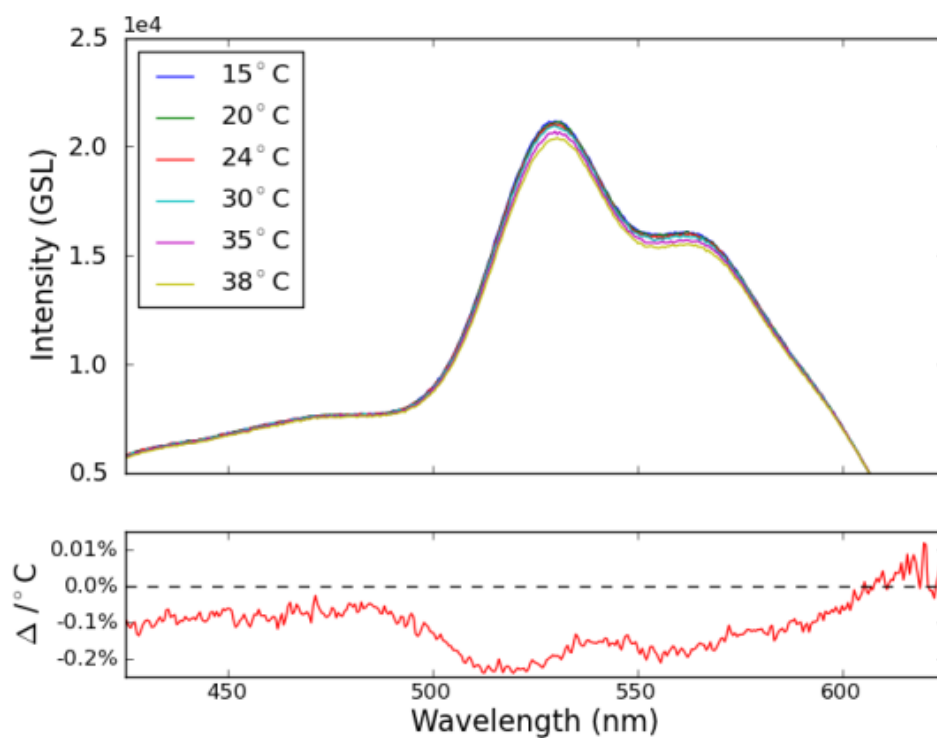


Figure 3.6. Isolated optical coupling. A small temperature-dependent decrease was observed in the light transmitted through the cyanoacrylate coupling. The bottom plot displays the average percent change in the spectrum per °C between 38°C and 20°C. A small decrease between 500 nm and 600 nm is observed. Note that the limits of the x and y axis here differ from those of other spectra figures to give a magnified view of this spectrum, and the two plots share the same x-axis.

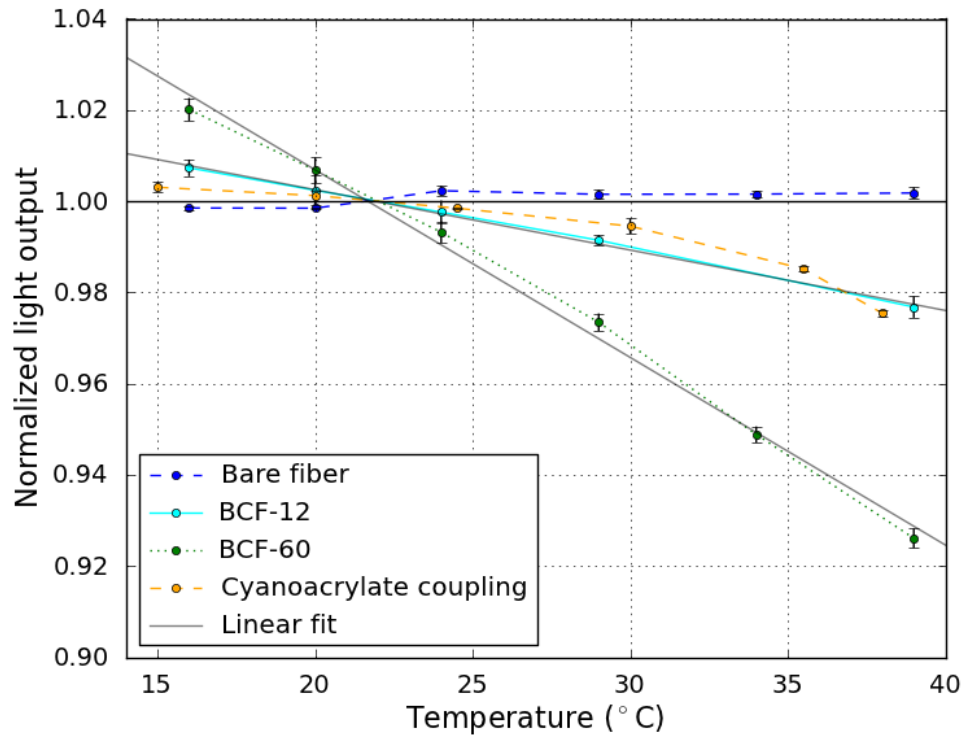


Figure 3.7. Total light output of each detector configuration as measured with a spectrometer. A more severe decrease in light output was observed for the BCF-60 PSD than for the BCF-12 PSD. Cerenkov light did not exhibit any temperature dependence. The cyanoacrylate coupling exhibited a temperature-dependent transmission. Each point is the average of 3 measurements, and the error bars represent 2 standard deviations of those measurements. Linear fits demonstrate that the intensity change of the BCF-60 PSD had a small nonlinear component, whereas the temperature dependence pattern for the BCF-12 PSD was entirely linear.

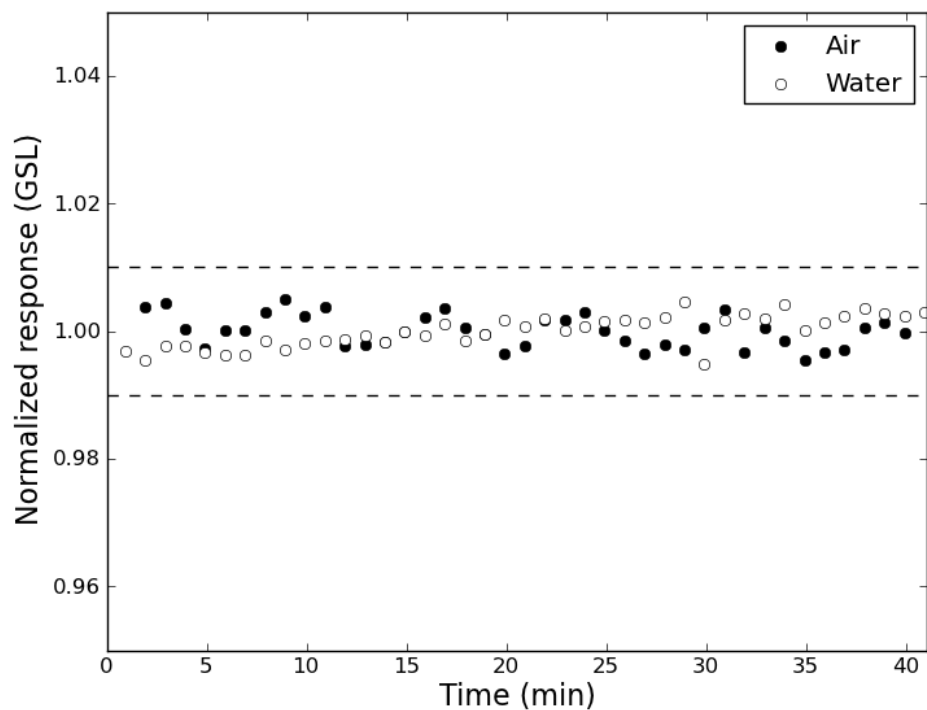


Figure 3.8. Stabilization. A room-temperature plastic scintillation detector immersed in 29°C water displayed a stable response over 40 minutes, from the first measurement at 50 seconds after immersion (dashed lines indicate $\pm 1\%$ from the average response). A slight upward trend owing to a small decrease in the temperature of the water over the 40 minutes was observed. Identical measurements in air confirmed that the plastic scintillation detector was stable under normal conditions.

3.4 Discussion

Contrary to widely accepted knowledge, our results indicate that PSDs are not universally temperature independent. The temperature dependence of BCF-60 PSDs is on the order of 1% within a few degrees of room temperature and on the order of 10% at human body temperature. The effect of temperature on BCF-12 PSDs is much smaller but would still contribute a systematic error in measured dose at noncalibration temperatures if uncorrected. Clearly the effect of temperature must be accounted for in current PSDs and minimized in future PSDs if possible.

Measurements with pairs of PSDs revealed nearly identical temperature dependence for PSDs built with like scintillating-fibers. From these results, we conclude that the temperature dependence of one PSD is sufficient to characterize the dependence of a large number of PSDs if care is taken to standardize the construction.

Our spectrometry data revealed several points of interest. First, neither the intensity nor the spectral distribution of the Cerenkov light collected from the bare fiber was temperature dependent. From this, we conclude that Cerenkov production and attenuation of light in the range of wavelengths spanned by the Cerenkov light in the optical fiber are temperature independent. The Cerenkov spectrum spans both the BCF-12 and the BCF-60 spectrum, so the temperature-independent attenuation of the optical fiber holds for both types of scintillators. Accordingly, any temperature dependence of the PSDs must be caused by changes in the light emitted from the scintillator or the transmission of light through the optical coupling. Additionally, the temperature independence of Cerenkov light is important because the chromatic removal technique

assumes that only the intensity and not the spectral distribution of Cerenkov light changes as irradiation conditions change.

Second, the distributions of the scintillators' spectra were observed to change slightly in addition to the total intensity. This is problematic because the chromatic removal technique requires the spectral distribution of scintillation light to be constant to extract the dose from the total light output correctly. Our implementation of this technique using a dichroic mirror specifically requires that the ratio of the portion of scintillation light reflected to the portion transmitted is constant. As stated in the results, this was not the case. This means that not only will the dose measured be incorrect owing to the change in scintillation light produced per unit dose, but the error will also be compounded by the incorrect extraction of dose from the total light.

We became aware after starting this research that Buranurak *et al.* had independently started similar work on scintillator temperature dependence. They reported changes in the light output and spectral distribution of BCF-12 and BCF-60 very similar to those found in our study, corroborating our results. Their findings were presented at the 2012 Luminescent Detectors and Transformers of Ionizing Radiation (LUMDETR) conference (September 2012).

Lastly, our spectrometry data showed that the transmission of light through cyanoacrylate optical coupling exhibited a nonlinear temperature dependence. The temperature dependence was largely confined to the wavelengths between 500 nm and 600 nm, which is why the relationship between light output and temperature was partially nonlinear for BCF-60 PSDs (most of the BCF-60 emission spectra fell in this range) but not for BCF-12. Because the quantity of cyanoacrylate used in our experiments was

greater than that used in a typical PSD, it is not possible to determine how much of either the BCF-12 or BCF-60 temperature dependence stems from the use of a cyanoacrylate coupling. However, given the relatively small nonlinearity of the BCF-60 PSDs compared with the cyanoacrylate transmission, it is safe to say that the cyanoacrylate contributes only a small amount to the BCF-60 detectors' temperature dependence.

The stability tests revealed that the PSD output stabilizes very rapidly when the temperature changes, reaching equilibrium in the first minute. This is likely due to the small size of the PSD, which has a diameter of only 2.3 mm, and the water-like thermal conductivity of the materials that make up the PSD. This is ideal for time-sensitive applications (e.g., integrating *in-vivo* dosimetry into the treatment workflow).

The disparity between the responses of BCF-60 and BCF-12 PSDs to temperature increases yields insight into an additional possible source of the temperature dependence. The key difference between these 2 scintillators is the wavelength shifting fluors used to convert the scintillation light, which is emitted primarily in the ultraviolet spectrum, to the visible spectrum. One fluor shifts ultraviolet light to blue light in BCF-12 and BCF-60 scintillators. In BCF-60 scintillators, a second fluor is responsible for shifting blue light to green light. This suggests that the wavelength shifting fluors may be partially responsible for the temperature dependence. Published data support this conclusion. Rozman and Kilin (1960) found that when a variety of fluors were incorporated into polystyrene scintillator, each combination exhibited temperature dependence and the dependence differed greatly depending on the fluor used. Surprisingly, Rozman and Kilin also observed temperature dependent emission of light in pure polystyrene.

Several methods to correct for the temperature dependence are possible. The simplest method is to determine the ratio of the measured dose at various temperatures to the measured dose at the temperature at which the detector was originally calibrated and use the inverse of these ratios as temperature-specific correction factors. However, this method does not account for the change in the spectral distribution. As stated previously, the changing distribution of the scintillation spectrum compromises the chromatic removal technique. Thus, this correction will only be exactly correct when irradiation conditions (e.g., field size, depth) are identical to the conditions used to determine the ratios. The change in distribution of the spectrum is small for both detectors, so this may introduce an acceptably small error into measurements. However, our study did not test this and cannot confirm that this is in fact the case; thus, further research is warranted.

A more effective but much more cumbersome solution would be to calibrate detectors at the temperature(s) at which they will be used. Any of the published calibration techniques could be used (Fontebonne *et al.* 2002, Archambault *et al.* 2006, Guillot *et al.* 2011), the only difference being that the scintillator would need to be heated to and maintained at a temperature of interest during the calibration. A separate calibration would need to be performed for each temperature at which the PSD will be used. The set of calibration coefficients resulting from a calibration would then be based on a temperature-specific intensity and spectral distribution of scintillation light. As such, no temperature correction would be necessary when using the calibrated PSD, provided measurements were performed at the same temperature as the calibration.

For *in-vivo* applications, a single correction factor or calibration for 37°C should be sufficient. The temperatures that might be encountered in the healthy adult population

range from 35.6°C to 38.2°C (Mackowiak *et al.* 1992), a 2.6°C difference. Thus one could assume the temperature of any individual is 37°C with a 1.3°C uncertainty. Based on our results, for a detector corrected/calibrated to measure at 37 °C this uncertainty would contribute a 0.41% and 0.17% uncertainty in total light output per unit dose for BCF-60 and BCF-12 respectively. Both are below 0.5% and small compared to other uncertainties that might be encountered in *in-vivo* dosimetry (for example, uncertainty in the detector location due to the difficulty of reproducibly placing the detector and due to anatomical motion).

Perhaps the best solution would be to construct a PSD that is minimally affected by temperature. To accomplish this, a scintillator with less intrinsic temperature dependence must be found. Rozman and Kilin's (1960) finding of a broad range of temperature dependence patterns for different wavelength shifting fluors suggests that this is possible. The BC-400 scintillator may be a good candidate, because Beddar *et al.* (1992a) found that it had no temperature dependence. Additionally, cyanoacrylate should not be used as optical coupling for scintillators emitting primarily in the green region of the visible spectrum. Other couplings need to be investigated before a recommendation can be made. Ayotte *et al.* (2006) found that a detector with no optical coupling is feasible if well polished, outputting approximately the same amount of light that a coupled scintillator might. Unfortunately, this may result in a less robust detector because of the impermanent connection between the scintillator and the optical fiber. It does not appear to be necessary to replace the plastic optical fiber.

3.5 Conclusion

We have found that PSDs built with BCF-60 or BCF-12 scintillating fiber exhibit non-negligible temperature dependence, with BCF-60 PSDs exhibiting greater temperature dependence than BCF-12 PSDs. For BCF-60 PSDs calibrated at room temperature, the dependence is on the order of 1% near room temperature and on the order of 10% at human body temperature. The exact mechanism of this temperature dependence is not known, but the wavelength shifting fluors and temperature-dependent transmission through cyanoacrylate appear to be at least partially responsible. We have suggested that a temperature-specific correction factors derived by characterizing the temperature dependence may be sufficient to account for this effect, although further research is required to validate this assertion. Alternatively, temperature-specific calibrations would account for the effect. In addition, carefully selecting the scintillator and optical coupling used in new PSDs may reduce the temperature dependence. Further research is needed to determine the optimal materials to use in a PSD to reduce or eliminate the temperature dependence.

CHAPTER 4

INTERNAL IN VIVO DOSIMETRY FOR PROSTATE INTENSITY MODULATED RADIATION THERAPY

This chapter is based on material published by the author of this dissertation in Physics in Medicine and Biology in 2014:[Wootton LS, Kudchadker RJ, Lee AK, and Beddar AS 2014 Real-time in vivo rectal wall dosimetry using plastic scintillation detectors for patients with prostate cancer. Phys. Med. Biol. 58 2955-67]. It is reproduced here with permission of IOP Publishing. Wording in the introduction and discussion has been modified to conform to the overall style of this dissertation.

4.1 Introduction

With the increasing complexity of radiation treatments, a commensurate increase in quality assurance procedures is important to ensure the safe and effective delivery of radiation to patients. An important aspect of a comprehensive quality assurance program is *in vivo* dosimetry (Yorke *et al.* 2005, Edwards and Mountford 2009, Mijnheer *et al.* 2013, Tanderup *et al.* 2013). Historically, *in vivo* dosimetry has been limited to skin dose measurements because only a few avenues have been available for internal *in vivo* dosimetry.

A fully developed internal *in vivo* dosimetry system would provide multiple benefits, including a direct verification of treatment and the ability to detect potential treatment variances immediately (e.g., incorrect plan delivery, incorrect monitor unit settings) and halt delivery to minimize deleterious effects. Internal *in vivo* dosimetry could also detect systematic errors over the course of treatment if, for example, the patient alignment used for treatment differed from the alignment used in simulation. Finally, *in vivo* dosimetry could provide measured data to supplement calculations for toxicity studies.

Relatively few detectors have been previously employed for *in vivo* dosimetry. Thermoluminescent dosimeters (TLDs) have been used because of their small size and tissue equivalence (Hsi *et al.* 2013). However, thermoluminescent dosimeters can provide only a cumulative dose and require a complicated readout process with expensive specialized equipment (DeWerd *et al.* 2009). As a result, the delivered dose is not known instantaneously, but rather with some delay after the treatment. Metal oxide semiconductor field effect transistors (MOSFETs) have also been used for internal *in vivo* dosimetry (Den *et al.* 2012). They are capable of real-time measurement and are very small, providing excellent spatial resolution and perturbing the beam minimally. Unfortunately, MOSFETs have short lifespans and must be replaced relatively often. Furthermore, they require a number of corrections, are expensive, and possess poorer intrinsic precision than other detectors (Jornet *et al.* 2004).

The plastic scintillation detector (PSD) is a good candidate for *in vivo* measurements. PSDs are extremely small, water-equivalent (eliminating the need for dose-to-water corrections and making them non-beam-perturbing detectors), and independent of angular, energy, and dose-rate effects (Beddar *et al.* 1992a 1992b). Furthermore, PSDs are capable of providing real-time data because they have a response time on the order of nanoseconds. Finally, PSDs are resistant to radiation damage and can be reused (Beddar 2006).

Substantial research has been directed toward developing PSDs for *in vivo* use. Archambault *et al.* (2010) demonstrated the feasibility of using PSDs for real-time measurements, with better than 1% accuracy. Subsequently, Klein *et al.* (2012) used PSDs to make real-time measurements of volumetric modulated arc therapy and

intensity-modulated radiation therapy (IMRT) treatment plans delivered to an IMRT phantom and an anthropomorphic pelvis phantom. The difference between the measured dose and the expected dose was less than 1%.

We have built on these results to develop a fully functional *in vivo* dosimetry system using PSDs for use in patients undergoing treatment for prostate cancer. The purpose of this chapter is to describe the real-time *in vivo* dosimetry system designed and constructed in our laboratory. Additionally, we will present the results generated by using this system to perform *in vivo* measurements of dose to the rectal wall in a small cohort of patients treated for prostate cancer with IMRT. Finally, we will compare the measured results with the treatment planning system (TPS) generated calculations to demonstrate the accuracy of this system.

4.2 Methods and Materials

4.2.1 Detector Design

Two millimeters of BCF-60 scintillating fiber 1 millimeter in diameter (Saint-Gobain Crystals, Hiram, OH) was optically coupled to Eksa GH-4001-P plastic optical fiber (Mitsubishi Rayon Corporation, Japan) with cyanoacrylate. BCF-60 was chosen for its high signal and spectral separation from signal-contaminating Cerenkov light (Beddar *et al.* 1992c). The plastic optical fiber was chosen for its water equivalency and robustness compared with silica or glass fibers. Approximately 25 m of optical fiber extended between the scintillating fiber and an ST optical connector that interfaced with a panel in a black box containing a Luca S charge-coupled device (CCD) camera (Andor Technology, Belfast, Northern Ireland). This length of optical fiber allowed the CCD to

be outside the treatment vault in the treatment console area. A dichroic mirror (model NT47-950; Edmund Optics Inc., Barrington, NJ) split the light delivered by the optical connector into 2 distinct spectra for decomposition via the chromatic removal technique (Fontbonne *et al.* 2002, Frelin *et al.* 2005, Archambault *et al.* 2006).

The Luca S CCD camera was chosen specifically for its suitability for performing real-time measurement. The Luca S is extremely fast, and when operating in frame transfer mode, has a dead time less than 300 μ s. Thus negligible signal (<0.1%) is lost to dead time. It is also extremely sensitive, capable of single photon detection. The detector elements are 10 x 10 μ m² each, and there are a total of 658x496 pixels for an imaging area of 6.58x4.96 mm. The average readout noise per pixel in frame transfer is 15 electrons. The signal (and thus the signal to noise ratio) depends on many factors such as the volume of scintillating fiber, the efficiency of the transmission of scintillation light, and the focusing of the camera. However, scintillating fibers are highly sensitive and when used in conjunction with the Luca S CCD high SNRs are easily achievable as a result (Archambault *et al.* 2010).

Three ceramic fiducials were attached to the detector as surrogates to aid the visualization of the detectors on computed tomographic (CT) images. One fiducial was attached to the distal tip of the detector and the other 2 were attached on either side of the fiber proximal to the sensitive volume of the detector (Figure 4.1). A carbon spacer of known dimensions was used to separate the scintillator from the distal fiducial. Carbon was chosen because of its similarity to tissue.

All detectors were calibrated in a cobalt 60 beam using the chromatic removal technique for Cerenkov correction using 3 dose conditions (Archambault *et al.* 2012).

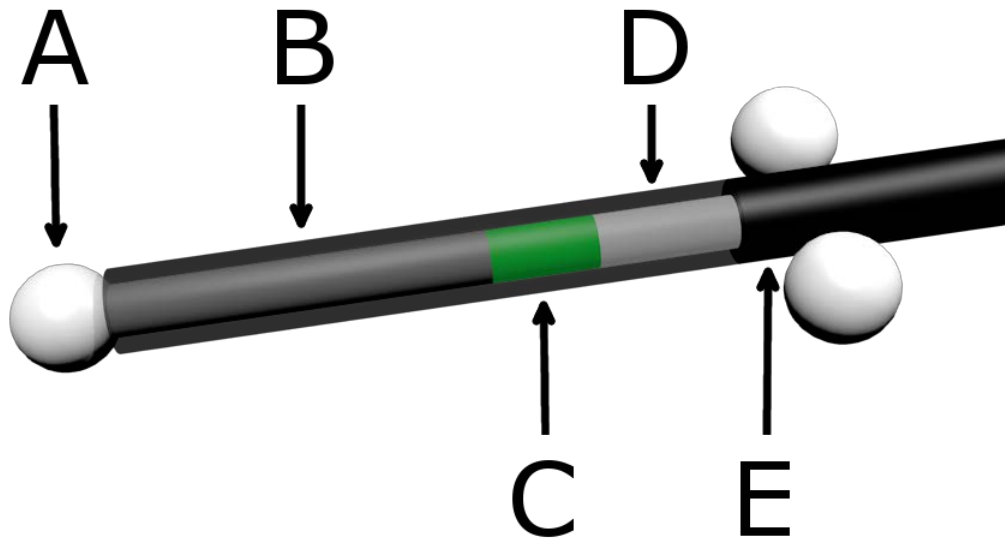


Figure 4.1. Scale model of an *in vivo* plastic scintillation detector. A) Ceramic fiducials of 2.3-mm diameter were used for visualization on daily computed tomographic images. B) A 7-mm-long carbon spacer provided separation between the scintillator and the distal fiducial to avoid potential dose shadows. C) Two millimeters of BCF-60 scintillating fiber was used. D) Plastic optical fiber transmitted emitted light to a photodetector. E) A polyethylene jacket prevented the admission of contaminating external light. The jacket covered the entire assembly, but is partially transparent here to reveal the inner components of the plastic scintillation detector.

4.2.2 Protocol Design

This research was conducted in accordance with an Institutional Review Board–approved protocol. The protocol stipulated that patients must have been diagnosed with prostate cancer (either with an intact prostate or after prostatectomy) to be eligible. Furthermore, only patients undergoing radiation therapy with the concurrent use of an endorectal balloon for prostate immobilization were eligible. No radiation modality was specified. However, we enrolled only patients undergoing IMRT for consistency and relevance, considering the widespread use of IMRT.

The data presented here were collected from the first 5 patients enrolled in the protocol. The patients ranged in age from 62 to 70 years and were diagnosed with T1c, T2b, or T3c prostate cancer with no nodal or metastatic involvement. Four patients were treated with a course of radiation to the prostate, seminal vesicles, and lymph nodes collectively followed by a boost to the prostate alone. The fifth patient was treated with radiation only to the prostate. *In vivo* measurements were performed twice weekly for the duration of each patient’s course of treatment, barring extraneous circumstances (e.g., CT scanner not functional). Approximately 14 treatments were monitored with 2 *in vivo* PSDs for each patient, resulting in a total of 142 *in vivo* measurements.

Each *in vivo* fraction proceeded as follows. Prior to the patient’s arrival, the system was prepared for use by connecting the CCD camera to a laptop for data acquisition and cooling the CCD to an operating temperature of -20°C via a built-in peltier element. A patient-specific PSD duplex (i.e., 2 PSDs attached to one another) was taken into the treatment vault on a spool. The distal end of the detector duplex was mounted to an endorectal balloon. The spool was unrolled and the proximal ends of the

PSD duplex connected to the CCD camera via ST connectors. Inside the vault, the treating therapists placed a latex sheath around the balloon and detectors. The sheath served to isolate the detector from direct contact with the rectal wall to facilitate reuse and to ensure that if a fiducial detached from the detector it would not remain in the patient.

After the patient was positioned on the couch, the rectal balloon was inserted by the therapist, and the patient was aligned using external marks. During this alignment a series of background images was acquired by the CCD camera. The treatment couch was then rotated 180 degrees to obtain a CT scan using a CT-on-rails linear accelerator (Varian Medical System, Palo Alto, CA; GE Healthcare, United Kingdom), with a slice thickness of 2.5 mm. This slice thickness is standard for CT-on-rails measurements obtained from patients with prostate cancer at our institution. The CT scan allowed accurate localization of the detector within the patient, as described in section 4.2.3. An example of a CT slice containing PSDs *in vivo* is displayed in figure 4.2.

After the CT scan, the patient was rotated back to the original position and then shifted using soft tissue alignment on the basis of the CT images. Megavoltage portal images were taken to confirm the isocenter position prior to turning the beam on, for consistency with non-protocol days on which the patients did not undergo a CT scan.

After the final port film was acquired, real-time data acquisition was initiated. The course of radiation was delivered normally, and after delivery of the final beam, the data acquisition was halted. The entire workflow is graphically summarized in figure 4.3. The balloon was then removed by therapists, and the latex sheath was removed and the

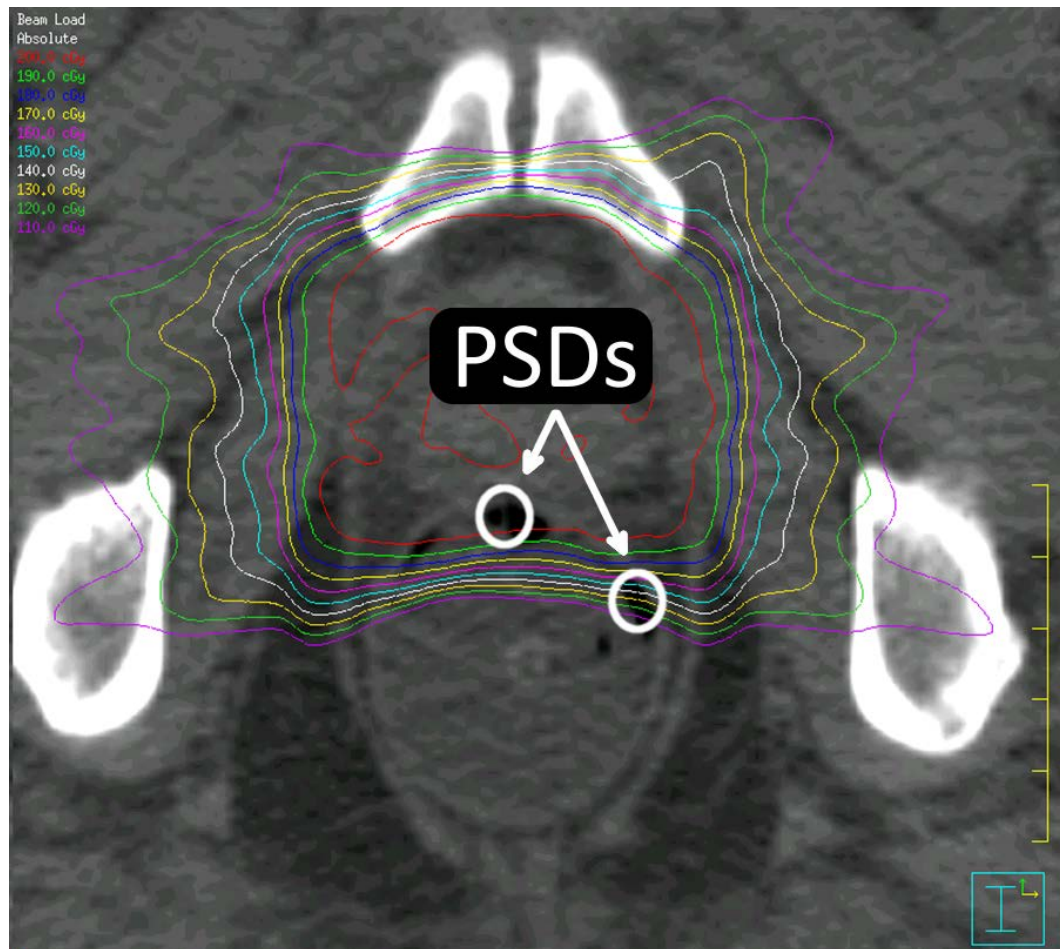
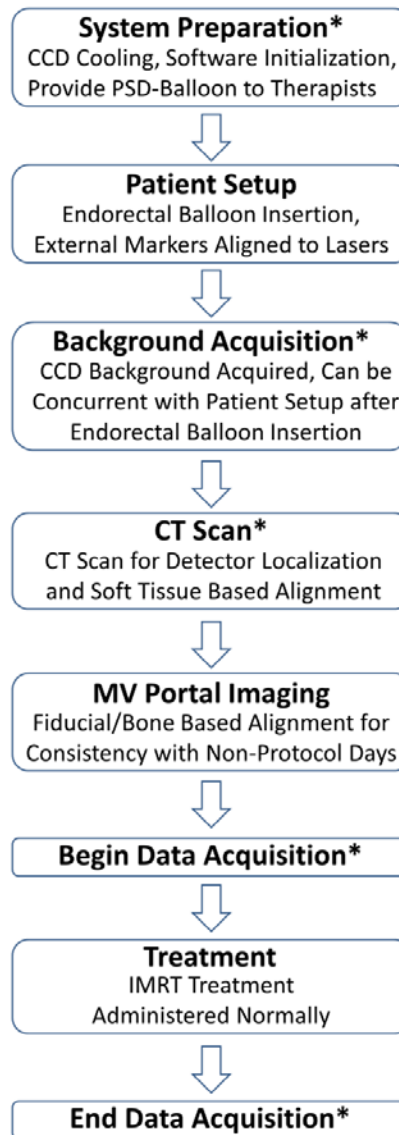


Figure 4.2. Plastic scintillation detectors (PSDs) *in vivo*. The active volume of 2 PSDs is contained in this axial slice. Isodose lines are also displayed, starting at 200 cGy with intervals of 10 cGy for each successive isodose line.



*Denotes Step Specific to *In Vivo* Protocol

Figure 4.3. Workflow diagram of the *in vivo* protocol workflow for a treatment fraction. Steps that would not occur during routine prostate IMRT treatment are denoted with asterisks. Most of the *in vivo* specific steps can occur in parallel with the normal workflow such that it need not be altered. For example, system preparation can occur before the patient arrives while another patient is treated. The background acquisition can occur while the patient is aligned to external markers as long as the rectal balloon with detectors has already been inserted. The exception is the CT scan. However, some patient are aligned with soft tissue each fraction, rather than using MV portal images. For these patients the CT scan would be a routine part of treatment, and the *in vivo* workflow would not disrupt or alter the treatment workflow in any way.

detectors were detached from the balloon. The balloon was then discarded and the PSD duplex was cleaned with medical-grade sanitary wipes.

Finally, each day that patient measurements were obtained, the PSDs were irradiated in a phantom using a simple fixed geometry to confirm that they were measuring dose as expected. This simple validation served to check for any damage or any change in response. The detectors were centered in a $10 \times 10 \text{ cm}^2$ field under 1.5 cm of tissue-equivalent bolus with 5 cm of acrylic back-scattering media and irradiated with 200 cGy. Any deviations $>2\%$ were considered indicative of damage or loss of functionality. In the rare case that such a deviation was observed, the detector was recalibrated.

4.2.3 Imaging Methodology

To calculate the expected dose to the detector, we needed to accurately identify the location of the detector on the CT image dataset. However, because the PSD is a water-equivalent detector, this cannot be done directly (i.e., the PSD is indistinguishable from tissue). This was the motivation to use fiducials attached to the detector as surrogates for localizing the PSD.

The fiducials attached to the detector were used to contour a region of interest (ROI) corresponding to the detector's active volume using a combination of manual input and scripting in the Pinnacle TPS (Philips Healthcare, Andover, MA), although the method is generalizable to any TPS with scripting capability. We assumed a rigid geometry between the 3 fiducials and the scintillating fiber. Operating under this assumption, it was straightforward to calculate the location of the scintillating fiber by

providing the location of each fiducial to a script as a point of interest. A 1-mm-diameter ROI centered on the scintillating fiber was contoured on the slice containing the largest portion of the fiber, because the fiber was not guaranteed to reside solely on one slice. If consecutive slices each contained more than a third of the scintillating fiber, contouring was performed on both slices.

To validate this method and its assumptions, we constructed detectors with CT-opaque metal wire substituted for scintillators, and we attached the detectors to endorectal balloons and imaged them in an anthropomorphic prostate phantom. The above method was used to automatically contour the wire and the resultant ROI compared with the position of the center of the wire, providing a quantitative measure of the accuracy of this method. This experiment was repeated 10 times with independent setups, using 2 detectors each time.

4.2.4 Data Acquisition

Data was acquired during each monitored treatment starting immediately after the final port film and continuing through the entire treatment. The data acquisition rate was set to 10 seconds (0.1 Hz) — that is, the CCD sequentially acquired 10-second integrations of the light output of the scintillator. Ten seconds was ideal because the longer integration time improved the signal-to-noise ratio of the measurements primarily by increasing the signal per image (the dominant noise was the readout noise of the CCD image, which was independent of integration times) while still allowing the temporal resolution necessary to distinguish between individual beams, the smallest portion of treatment for which dose information is easily retrievable from the Pinnacle TPS.

A temperature dependence correction factor was also applied to each detector. The correction factor was determined by performing repeated irradiations at varying temperatures, as described by Wootton and Beddar (2013), and assuming an idealized body temperature of 37°C for all patients. Small variations from 37°C would have a negligible effect on the final measured dose.

To quantify the agreement between planned dose and measured dose, the location of each detector was first contoured on the daily CT image dataset. Then the beam parameters were imported from the patient's treatment plan and used to calculate the dose distribution on the daily CT image dataset. Because the treatment couch rotated between the CT scanner (imaging) and the linac (treatment), the setup in the daily CT image dataset was identical to the setup used during treatment, with the exception of any patient movement occurring after the CT scan. The isocenter in the CT image was confirmed to be correct by comparing digitally reconstructed radiographs with daily port films. The expected dose for each detector was simply the mean dose in the corresponding ROI.

4.2.5 Data Analysis

For each fraction, the percent difference between the measured and expected dose was calculated (relative to the calculated dose). For each patient, a mean difference, a standard deviation, and a 95% confidence interval of the mean were computed. The confidence interval was computed using the *t*-distribution with degrees of freedom equal to 1 less than the number of measurements. Finally, the mean of the mean differences was computed over all 5 patients, as well as a standard deviation and a 95% confidence

interval. The confidence interval was again computed using a t -distribution, this time with 4 degrees of freedom (1 less than the number of patients).

Only 3 measurements were excluded from this analysis, owing to physical damage to the termination of the optical fiber at the CCD interface, resulting in severely compromised light transmission. The damage was revealed by visual inspection prompted by detectors failing the post-treatment validation. Aside from these 3 measurements, all 139 remaining data points were included in the analysis.

4.3 Results

4.3.1 Imaging Methodology

The mean difference between the center of the contours and the center of the wires in the axial plane in the phantom study was 0.1 mm in the anterior direction. The standard deviation of the differences was 0.4 mm, and 100% of the contours were within 0.7 mm of the wire. 65% of the contours were on the correct axial slice and 35% were one slice off (Figure 4.4).

4.3.2 In Vivo Results

The results for each patient are listed in table 4.1. The mean difference between measured and calculated dose ranged between -3.3% and 3.3%. For 4 of the 5 patients, the standard deviation was between 5.6% and 7.1%. The standard deviation for the fifth patient was 14.0%. Eighty-two percent of the measurements agreed with the Pinnacle TPS calculated dose to within 10%. The percent differences are plotted in a histogram shown in figure 4.5, and the patient-specific results are plotted in a boxplot in figure 4.6.

Patient	No. of measurements	Mean dose difference	95% confidence interval	Standard deviation	Validation
1	30	-2.6%	-4.7%, -0.5%	5.6%	-0.1%
2	28	-1.1%	-3.9%, +1.6%	7.1%	0.5%
3	30	1.5%	-1.0%, 4.0%	6.7%	0.3%
4	28	3.3%	-2.1%, 8.7%	14.0%	0.5%
5	21	-3.3%	-5.9%, -0.6%	5.8%	-0.5%

Table 4.1. *In vivo* dosimetry results for each patient. The 95% confidence interval of the mean was computed using a *t*-distribution with (measurements – 1) degrees of freedom. Validation is the mean discrepancy between the known and measured dose delivered to the plastic scintillation detector during the detector's performance validation after patient treatments.

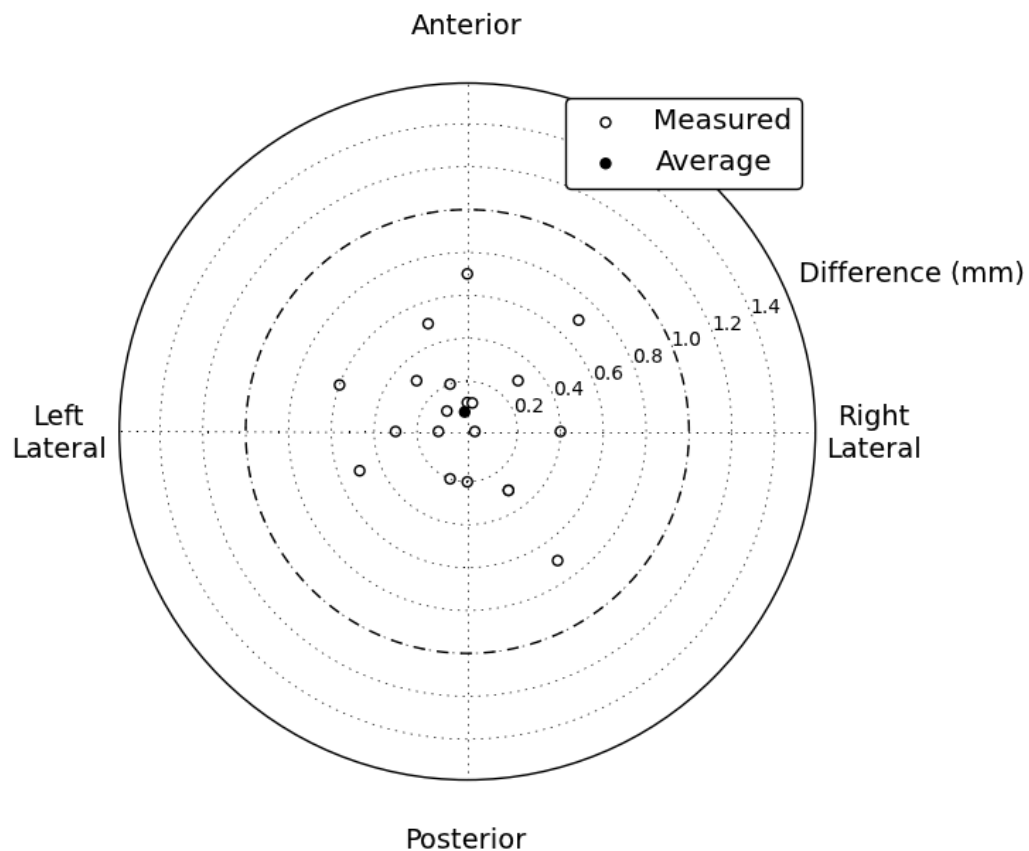


Figure 4.4. Axial discrepancies between script-contoured locations and actual locations. All 20 contoured locations were within 0.7 mm of their actual location, and the mean difference was 0.1 mm in the anterior direction.

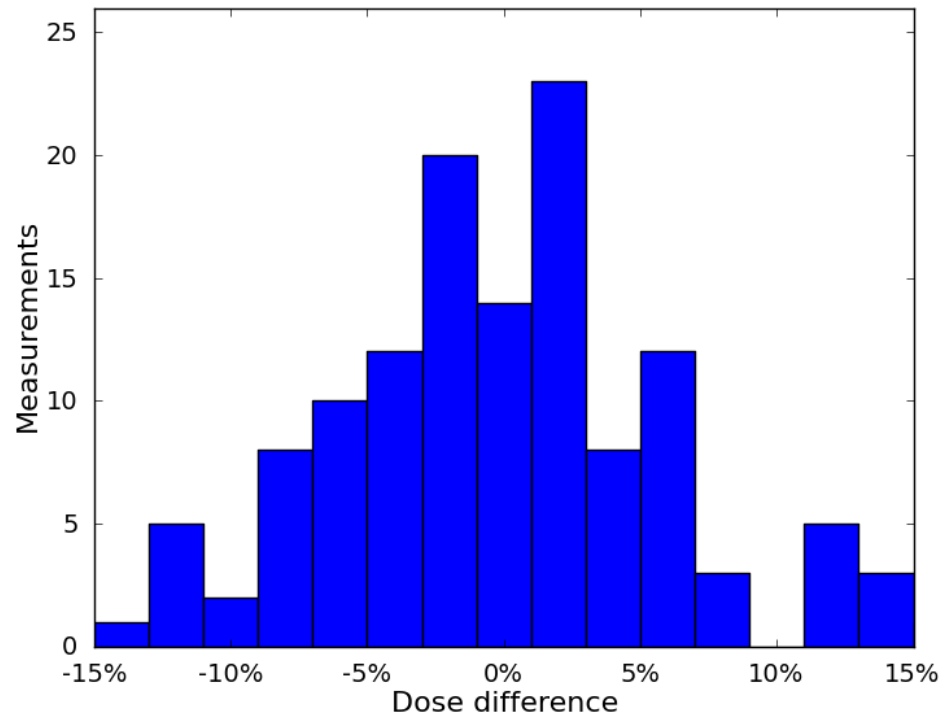


Figure 4.5. Distribution of differences between measured dose and calculated dose. The distribution was centered near 0 and was mostly contained within $\pm 10\%$.

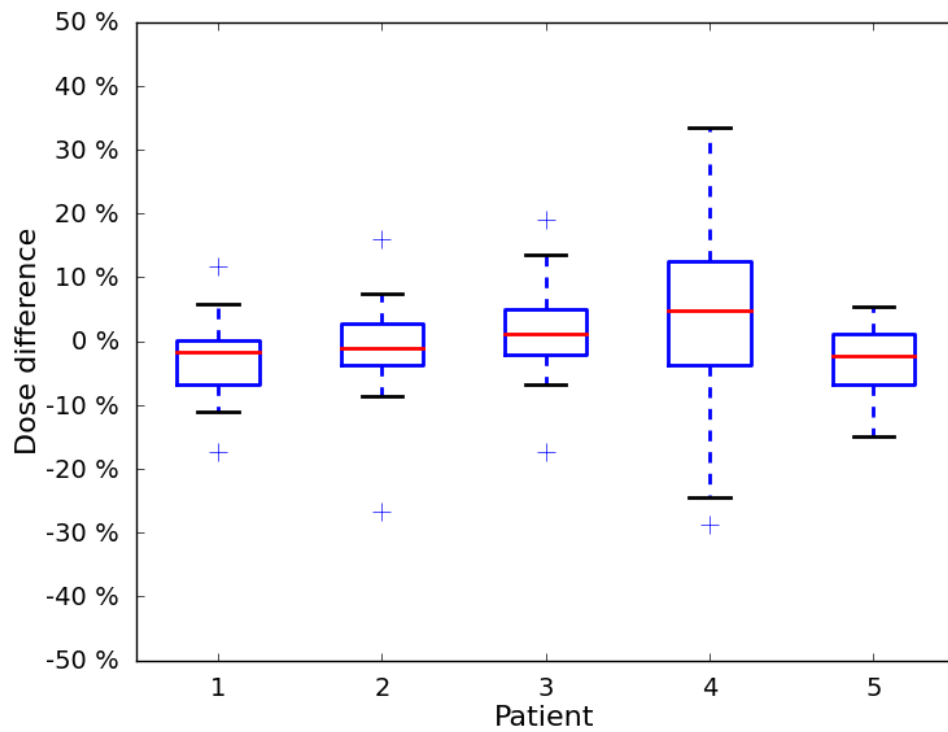


Figure 4.6. Boxplot of patient-specific results. The mean difference between measured dose and calculated dose was near 0 for all 5 patients. Patients 1-3 and 5 exhibited very similar distributions, and patient 4 exhibited a relatively larger spread.

When the patient-specific results were analyzed, the overall mean difference between measured dose and calculated dose was -0.4%. The standard deviation was 2.8% (standard deviation of the 5 mean differences). The 95% confidence interval of the mean extended from -3.9% to 3.0%.

The temporal resolution of the system was consistently sufficient to identify dose from individual beams during treatment for comparison with the dose for each beam calculated by the Pinnacle TPS. This is demonstrated in figure 4.7.

Each patient was questioned regarding the use of the probes, and 4 of the 5 patients reported not noticing any difference between the balloon with and without the detectors. The remaining patient reported that he noticed a difference but that it was tolerable. All patients tolerated the PSD attached to the balloon through the entirety of their treatment.

4.4 Discussion

Our results demonstrate that PSDs can be successfully used to measure rectal wall dose in real time and *in vivo* during prostate IMRT. We have developed a simple, effective visualization methodology for locating these water-equivalent detectors on CT images and integrated the use of these detectors into normal clinical workflow.

The imaging methodology performed exceptionally well in the axial plane when tested in an anthropomorphic phantom. The detector active volume was identified with submillimeter accuracy and precision. However, the methodology exhibited reduced accuracy in the superior-inferior (SI) direction. This can be attributed to inherent limitations resulting from slice thickness; the location of the fiducials cannot be specified

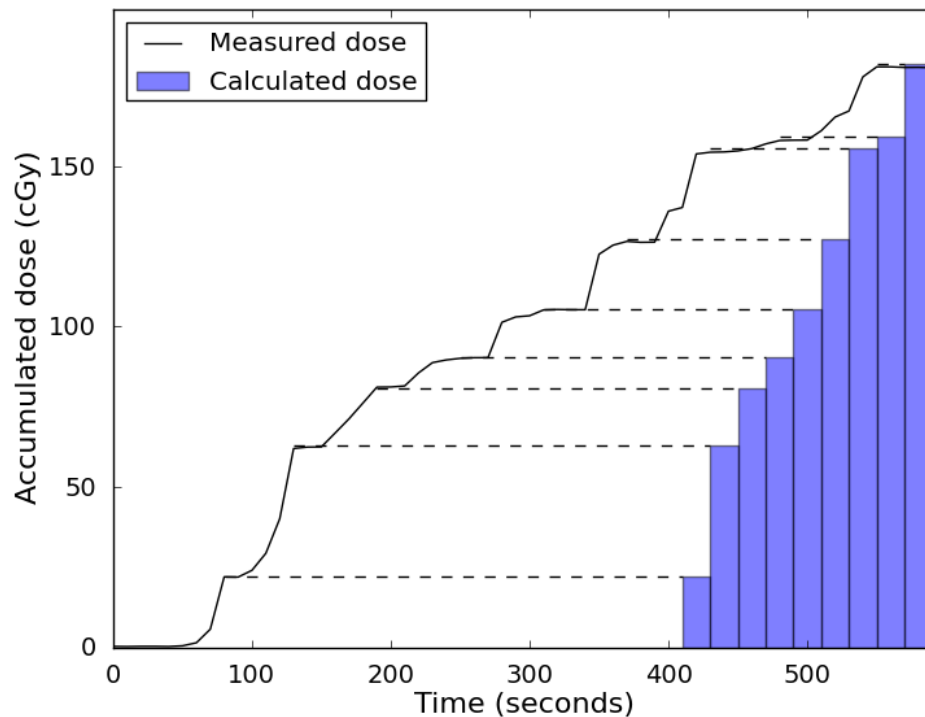


Figure 4.7. PSD measured real-time dose. The accumulated dose measured by one of the plastic scintillation detector is plotted in black. The treatment planning system allows the cumulative dose-per-beam to be extracted (represented by blue bars at right), but not the cumulative dose as a function of time. Dashed lines between the measured dose and the bars are meant to facilitate comparison. Between beams when there is no radiation, the measured dose profile is flat. If the detector is measuring dose accurately, these plateaus in the dose profile should agree with the cumulative beam-by-beam dose. As can be seen, these plateaus agree excellently with the cumulative doses calculated by the treatment planning system, indicating good beam-by-beam agreement between the plastic scintillation detector and treatment planning system.

with precision better than the magnitude of the slice thickness. Smaller slices could be used to improve the localization of the detector in the SI direction. However, SI accuracy was deemed far less important than axial accuracy for this study because the dose gradient posterior to the prostate was steep in the anterior-posterior direction in the axial plane and essentially flat in the SI direction. Thus, the results presented were sufficient for our study.

This study is subject to statistical limitations. Ideally more patients should have been included in the study. However, owing to the large number of fractions monitored for each patient with *in vivo* dosimetry, this was not possible without greatly extending the time required to complete this study. Because of the limited number of patients, the results generated from the 5 patient mean differences theoretically may not be representative of the PSD system's performance in the general population. However, few variables might affect how a detector performs for a given patient, given that this is an entirely physical process; that is, radiation transport is not affected by biological factors. A possible variable would be the magnitude of patient-specific intrafractional movement. The system would exhibit a loss of precision in patients prone to extreme intrafractional movement. Assuming this movement was not significant in any given direction, the accuracy should not be compromised. Given the highly similar performance of the system for 4 out of the 5 patients (Figure 4.6), we believe that our results are representative of the performance that could be expected from this type of detector system. The reasons for the erratic performance of the detector for the remaining patient are addressed below.

Our data indicate that most measurements that deviated largely from the calculated dose occurred when the PSDs were located either laterally or posteriorly in the rectum. This occurred as a result of twisting of the endorectal balloon as the balloon was inserted into the rectum. The reasons for the larger deviations are twofold. The first is the magnitude of the dose gradient. The dose gradient is relatively shallow in the anterior rectum owing to the need for complete coverage of the prostate, which is immediately adjacent to the rectum. However, because the rectum is an organ at risk, the dose decreases rapidly away from the prostate, resulting in a far steeper dose gradient in the anterior-posterior direction within the rectal balloon and at the lateral rectal walls (refer to figure 4.2). This means that intrafractional motion will have a disproportionately large effect on the dose measured by laterally positioned detectors. The second reason is that the reference dose (the Pinnacle calculated dose) is lower for lateral and posterior measurements than for other measurements, inflating the percent difference (for example, an absolute discrepancy of 10 cGy is 5% relative to 200 cGy and 10% relative to 100 cGy). The combination of these 2 effects is illustrated in figure 4.8. The position of the detector depends on the insertion of the balloon. Occasionally the balloon twisted during insertion. After insertion, it was not possible to adjust it without removing it because of the latex sheath. Removing the balloon and reinserting it to achieve better detector positioning was not considered worthwhile at the cost of causing the patient additional discomfort and extending the overall treatment time.

As mentioned previously, the system produced results characteristically different for one of the patients. There are several identifiable reasons for this, all of which relate

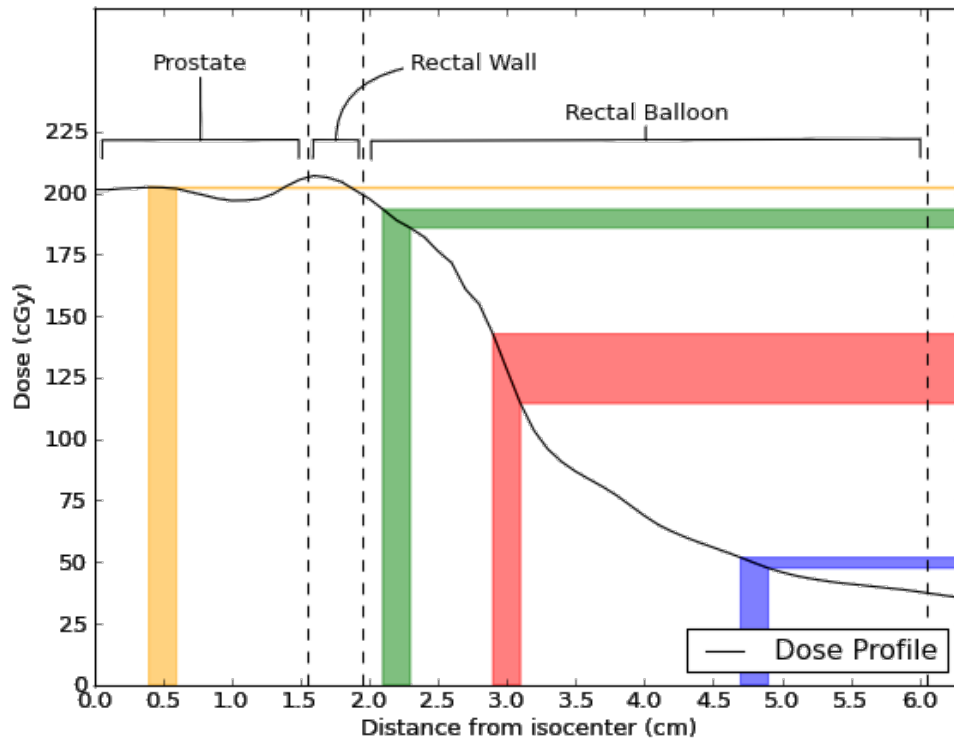


Figure 4.8. Dose profile taken from patient data starting at the isocenter in the prostate and extending to the posterior rectal wall. Different regions of anatomy are labeled and demarcated by dashed lines. Uncertainties in the expected dose to be measured by a hypothetical detector with a positional uncertainty of ± 1 mm are displayed as colored bars. At the anterior rectal wall (green), the positional uncertainty translates to an uncertainty in expected dose of $\pm 2\%$. A laterally positioned detector (red) exhibits an uncertainty of $\pm 11\%$ owing to the steep gradient and lower absolute dose. A detector positioned posteriorly (blue), although in a shallow gradient, exhibits an expected dose uncertainty of $\pm 4\%$ owing to the very low absolute dose. Finally, a hypothetical detector positioned in the urethra (yellow) is completely unaffected by positional uncertainty (expected dose uncertainty of $\pm 0.1\%$).

to the patient's size. This patient was obese, whereas the other 4 patients had average weight. This decreased the image quality of the CTs acquired for this patient (we measured the signal-to-noise ratio of the patient's CT images to be roughly half that of the other patients), making detector localization more difficult. Additionally, because of the patient's large size, the patient was truncated from the CT field of view. As a result, some tissue was missing from the image and artifacts were present where tissue was cut off (Figure 4.9). Finally, the balloon was twisted out of position in this patient far more often than in other patients. This subjected the PSD system to the gradient-related difficulties discussed in the previous paragraph with higher regularity, increasing the overall variability of the agreement between measured dose and calculated dose. We suspect that the patient's size made correct insertion of the balloon more difficult or caused increased twisting of the balloon during insertion. We also at first considered increased intrafractional movement in this patient as a possibility, but literature indicates that the magnitude of intrafractional movement is unchanged or possibly decreased in obese patients relative to the general population (Butler *et al.* 2012).

An important question is the feasibility of implementing this system in a clinical setting. The system was integrated easily into the treatment workflow. Therapists did not have to alter their procedure at all from that used for patients receiving CT-on-rails guided IMRT, save for stepping over the optical fiber and sheathing the balloon with latex. This suggests that clinical implementation is possible. Another important consideration is the feasibility of using this system without a CT-on-rails, because most



Figure 4.9. A computed tomographic scan from a patient for whom the plastic scintillation detector system exhibited poor precision. The image quality was compromised and patient tissue was truncated from the computed tomography field of view (at right). However, the primary source of the lost precision was the difficulty of placing the balloon correctly in this patient.

institutions do not have CT-on-rail units. Two possibilities exist: either cone beam CT could be used or perhaps MV/kV orthogonal imaging could be used. For cone beam CT, it would be straightforward to adopt the methodology described here. Using portal imaging would be more difficult, but the success of Hsi *et al.* (2013) using portal imaging to locate thermoluminescent detectors for *in vivo* dosimetry suggests that it is possible. More research along this avenue is warranted.

4.5 Conclusion

We have successfully used PSDs for *in vivo* dosimetry of the rectal wall of patients with prostate cancer undergoing IMRT, with good results. The accuracy (mean difference between measured and expected dose) was excellent, at -0.4%. The precision of the system was good for *in vivo* dosimetry, at 5.6% to 7.1% for 4 of the 5 patients. We have also presented a simple but effective method for localizing water-equivalent detectors *in vivo*. Overall, the PSD has proven to be an excellent detector for *in vivo* use, with promising future applications (e.g., *in vivo* dosimetry of stereotactic radiosurgery, volumetric modulated arc therapy, etc.).

CHAPTER 5

PASSIVELY SCATTERED PROTON BEAM ENTRANCE DOSIMETRY WITH PLASTIC SCINTILLATION DETECTORS

5.1 Introduction

The popularity of proton therapy as a treatment modality is growing rapidly owing to advantageous characteristics of protons such as a finite range and a characteristic dose depth curve wherein dose is concentrated at the end of that range. As a result, protons are useful for highly targeted therapy with low integral dose to normal tissue. However, these unique benefits bring with them important considerations when treating patients.

One such consideration is the lack of skin sparing. Whereas therapeutic photon beams exhibit a skin sparing effect owing to a buildup of secondary electrons over a small distance, protons interact directly and do not have this quality. Furthermore, proton treatments typically use fewer beams than photon treatments (particularly compared with intensity-modulated radiation therapy and volumetric modulated arc therapy), which exacerbates the lack of skin sparing. As a result, patients commonly experience skin reactions such as radiation dermatitis (Chang *et al.* 2011, Sejpal *et al.* 2011, Zenda *et al.* 2011). Skin dose is therefore an important consideration in proton therapy and can even be a limiting factor when planning treatment for sites such as the lung or breast (Whaley *et al.* 2013).

In vivo entrance dosimetry (also called skin dosimetry) can be used to investigate skin reactions. Comparing accurate measurements of delivered skin dose with skin reactions in individual patients can help physicians better quantify risks of toxic effects. These risks could then be used to refine treatment strategies and evaluate treatment plans. As an added benefit, *in vivo* entrance dosimetry can catch gross errors in treatment administration, such as incorrect SSD, malfunction of the delivery system dose monitor, or interlock failures.

A few detectors have already been used to measure skin dose during treatment. The commercial MOSFET detector, OneDose, has been used with success (Cheng *et al.* 2010). However, OneDose has a few drawbacks, including the single-use nature of each detector (requiring calibration of a few detectors from each batch to account for detector variability) and variation in response depending on the angle and radiation energy. Thermoluminescent dosimeters have also successfully been used to measure proton dose (Zullo *et al.* 2010), but the necessity of waiting 2 to 3 days before reading the dose is not ideal.

Plastic scintillation detectors (PSDs), however, do not suffer from any of the shortcomings listed above. They can be reused extensively, do not exhibit an orientation-dependent response, and provide real-time results. PSDs can be very small (~1 mm in diameter) and are water-equivalent (Beddar *et al.* 1992a, 1992b). PSDs can therefore make measurements in a beam without significantly perturbing it (Beddar *et al.* 2001). Finally, PSDs have been used for *in vivo* dosimetry in photon-based therapy already (Wootton *et al.* 2014). Although there are some drawbacks to using PSDs, such as ionization quenching, which we address in the current study, PSDs are nonetheless promising candidates for *in vivo* entrance dosimetry in proton therapy.

The aims of this study are threefold, with the overall goal of establishing the feasibility of using PSDs for *in vivo* entrance dosimetry for a passively scattered proton beam. The first is to evaluate the effect of ionization quenching on a PSD used for entrance dosimetry. Ionization quenching is an under-response of the PSD due to high linear-energy transfer associated with heavy charged particles (Birks 1964). Previous PSD studies have evaluated this effect in the context of relative dosimetry using Monte

Carlo and measurements (Torrise 2000, Archambault *et al.* 2008, Wang *et al.* 2012), but measurements have not been performed to establish the effect of quenching on absolute dosimetry and the practicality of correcting it. The second is to determine whether the generation of Cerenkov light in the PSD can be safely ignored. Cerenkov light is most intense at the entrance of a proton beam (Glasser *et al.* 2014), so although previous studies have found that Cerenkov light can be ignored for measurements at depth, measurements at the entrance of the beam merit investigation. The final aim is to investigate general dosimetric characteristics of PSDs used for entrance dosimetry, such as accuracy and precision.

5.2 Methods and Materials

5.2.1 Detectors

A PSD was fabricated from 3 mm of BCF-12 scintillating fiber (Saint-Gobain Crystals, Hiram, OH) with a diameter of 1 mm; the scintillating fiber was optically coupled to 3 m of clear plastic optical fiber. A photodiode was used to convert the scintillation light transmitted by the optical fiber into electrical charge. The photodiode had dual channels sensitive to different wavelength so that it could quantify the signal in the blue and green portions of the spectrum separately. This allowed for analysis via the chromatic removal technique (Fontbonne *et al.* 2002, Frelin *et al.* 2005, Archambault *et al.* 2006), which is necessary for eliminating the light contribution from Cerenkov light in the plastic optical fiber (Beddar *et al.* 1992c). The photodiode was chosen because it could be placed in the treatment vault, thus converting scintillation light to an electric signal near the point of measurement. This offered an advantage over charge-coupled device cameras and

photomultiplier tubes, 2 other devices commonly used for light quantification, which are more sensitive to radiation and should be placed outside of the vault. In such a setup, a significant loss of signal would result from attenuation of scintillation light as it passed through the long optical fiber required to reach outside the vault. In contrast, minimal signal is lost over a triaxial cable, as was used in our setup. The signals from the photodiode were measured using a SuperMax electrometer (Standard Imaging, Madison, WI).

The PSD was calibrated on a Cobalt 60 unit, chosen for the high degree of accuracy and precision achievable owing to the highly stable and well-characterized output of Cobalt 60, using the chromatic removal technique. The resulting calibration was independently verified by irradiating the PSD with a known dose on a Varian linear accelerator, and the calibration was found to be accurate to within 1%.

For absolute dose comparison in the proton beam, a calibrated parallel plane ion chamber (PTW, Freiburg, Germany) was used (International Atomic Energy Agency TRS 398 Report 2001), with an entrance window thickness of 0.9 mm (acrylic) and an active volume of 0.02 cm^3 . All ion chamber readings were corrected for ambient pressure and temperature. The ion chamber was operated at +300V and the charge was read out using a Scanditronix/Wellhofer electrometer (Scanditronix Wellhofer North America, Bartell, TN). Background subtraction was used for both the SuperMax and Wellhofer electrometers to ensure accuracy. The absolute dose was calculated using the method described in the International Atomic Energy Agency TRS 398 Report (2001).

Finally, radiochromic film was used to measure lateral profiles of proton beams for comparison with profiles measured using the PSD (Vatnitsky 1997, Niroomand-Rad

et al. 1998, Zhao and Das 2010). Gafchromic EBT3 film (Ashland Inc., Covington, KY) was chosen for its large dynamic range and ease of use (i.e., no development necessary). Calibration curves were generated for each energy at which film was used to measure profiles. Films were scanned before irradiation and 48 hours after irradiation on an Epson flatbed scanner (Epson Corp., Suwa, Japan) in transmission mode at a resolution of 400 dpi. The pre-irradiation film images were used for background subtraction. Per manufacturer specifications, only the red channel of the scanned image was used because of its high sensitivity in the range of doses used in the study.

5.2.2 Setup

The passive scattered beam in the fixed beamline treatment vault at our institution's proton center was used. A brass aperture with a 12×12 cm cutout in the center shaped the field for all measurements.

Acrylic blocks were placed on the treatment couch with the surface of the blocks at an SSD of 270 cm. For measurements using the ion chamber, an acrylic block with a custom-milled cavity designed to hold the ion chamber surface flush with the surface of the block was used. For measurements with film, a plain acrylic block was used and the film was affixed to it with tape. When these blocks were switched out or other adjustments were made that might disturb the setup, the SSD was re-verified using the treatment positioning lasers.

When direct comparisons were made between ion chamber measurements and PSD measurements, the ion chamber was centered on the beam's central axis and the PSD was attached to the surface of the block immediately adjacent to the ion chamber

(rather than directly in front of the ion chamber). This was done because the charge measured by the ion chamber increased by 1% when the PSD was placed in front of it, relative to the charge measured when the PSD was placed adjacent to the ion chamber, for a 140-MeV beam. The PSD response was the same in both positions. For a 250-MeV beam, no change was observed in the PSD or ion chamber signal between the 2 scenarios (i.e., PSD in front of the ion chamber or adjacent to it). Placing the PSD adjacent to the ion chamber allowed concurrent measurement of the entrance dose and eliminated fluctuations in beam output as a contributor to differences between the dose measured with the ion chamber and the dose measured with the PSD.

5.2.3 Ionization Quenching Characterization

First, absolute entrance dose on the central axis of the beam was measured using the ion chamber and the PSD for a range of nominal proton energies between 140 MeV and 250 MeV, with a fixed spread out Bragg peak (SOBP) width of 8 cm. The purpose of this was to quantify the effect of ionization quenching on the PSD as a function of beam energy. Three irradiations of 50 MU were performed at each energy. The difference between the dose measured with the ion chamber, considered to represent the correct dose, and the dose measured with the PSD was calculated for each irradiation. The mean and standard deviation of these differences were then calculated. The difference was also used to calculate correction factors for the dose measured with the PSD.

Next, absolute entrance dose was measured for a variety of SOBP widths at fixed energies of 225 MeV and 140 MeV. The purpose of this was to determine what effect the introduction of low-energy protons, necessary for widening the SOBP, had on the

quantity of ionization quenching in the PSD. SOBP widths of 1, 4, 8, 12, and 16 cm were used for the 225 MeV beam, and widths of 1, 2, 4, 8, and 10 cm were used for the 140 MeV beam. (One centimeter is the minimum SOBP width allowed by our system, 16 cm is the maximum SOBP width allowed for the 225 MeV beam, and 10 cm is the maximum SOBP width for the 140 MeV beam.) Again, 3 irradiations of 50 MU each were performed for each setting, and the mean difference and standard deviation were computed.

5.2.4 Cerenkov Light Removal

Next, the contribution of Cerenkov light was investigated. The PSD was first irradiated in the normal setup and then irradiated again with extra optical fiber coiled into the beam to increase the generation of Cerenkov light. All other conditions were held constant. The normal setup had approximately 6 cm of fiber in the field, whereas roughly 20 cm of fiber was coiled into the field for the second irradiation. This was done at 225 and 140 MeV, and the increase of signal in each channel was quantified as an indicator of Cerenkov light produced in the clear optical fiber.

To quantify the effect of neglecting Cerenkov production on the accuracy of the system, the PSD was calibrated at the lowest energy assuming no Cerenkov light (i.e., a single calibration factor was generated, equal to the ratio of the dose delivered to the total light output). This calibration was used to recalculate the dose for the measurements performed in section II.C. The dose calculated at each energy level was then corrected for ionization quenching using the results from the previous section; the remaining discrepancy was therefore assumed to be an artifact of Cerenkov light contamination.

5.2.5 Accuracy and Precision of Relative Dose Measurements

Lateral half profiles were measured using the PSD for the 225 MeV and 140 MeV beams and compared with profiles measured using film. The purpose of this measurement was to validate the relative accuracy of the PSD, specifically in the steep dose gradient of the beam penumbra. The PSD profile was acquired by centering the detector's active volume on the central axis of the beam using the lasers. The PSD was oriented vertically so that the lateral resolution corresponded to the diameter of the scintillating fibers (1 mm) and not the length (3 mm). At each position, 3 separate irradiations of 50 MU were measured, and then the couch was translated laterally to move the PSD through the field with high accuracy and precision.

The radiochromic film was cut into long strips approximately 4 cm tall and 20 cm wide to encompass the entire lateral extent of the beam. A vertical mark was placed on the film with marker above the central axis of the beam, and 2 lateral marks were placed on either side of the central axis of the beam using the gantry lasers. The lateral marks were used in analysis to account for rotation of the film strip relative to the beam. The vertical mark indicated the precise center of the profile, to facilitate direct comparison between the film profile and the PSD profile. As mentioned previously, the film was scanned before irradiation and 48 hours after irradiation. The red channel of the pre-irradiation image was subtracted from the post-irradiation red-channel, and the pixel values were converted to dose using a previously acquired calibration curve with a python script. Pixel-by-pixel dose values were averaged in a narrow vertical band, approximately 2 cm tall, centered on the lateral plane to improve the signal-to-noise ratio

(SNR). No smoothing was done along the profile. The central mark on the film and the scanner resolution were used to assign absolute locations (i.e., distance from 0) for each point in the profile. The PSD measurements were normalized to the measurement on the central axis, and the film measurements were normalized to the flat region at the center of the profile.

Finally, the SNR of the PSD was measured as a function of dose at 225 MeV and 140 MeV. Three sets of 3 irradiations were measured using 1, 10, and 100 MU, for a total of 9 irradiations at each energy. The SNR was calculated as the standard deviation of the measurements divided by the average value.

5.3 Results

5.3.1 Response vs Range

The difference in doses measured by the PSD and the ion chamber is shown in figure 5.1. For energies between 200 and 250 MeV, the PSD under-responded by 7% with an average uncertainty of $\pm 1\%$ (with uncertainty expressed in percentage points, i.e., the under-response of the PSD is between 6% and 8%). The under-response increased to approximately $10\% \pm 1\%$ of the dose measured by the ion chamber for energies between 180 and 140 MeV. Within these energy ranges, the loss of signal owing to ionization quenching was fairly stable.

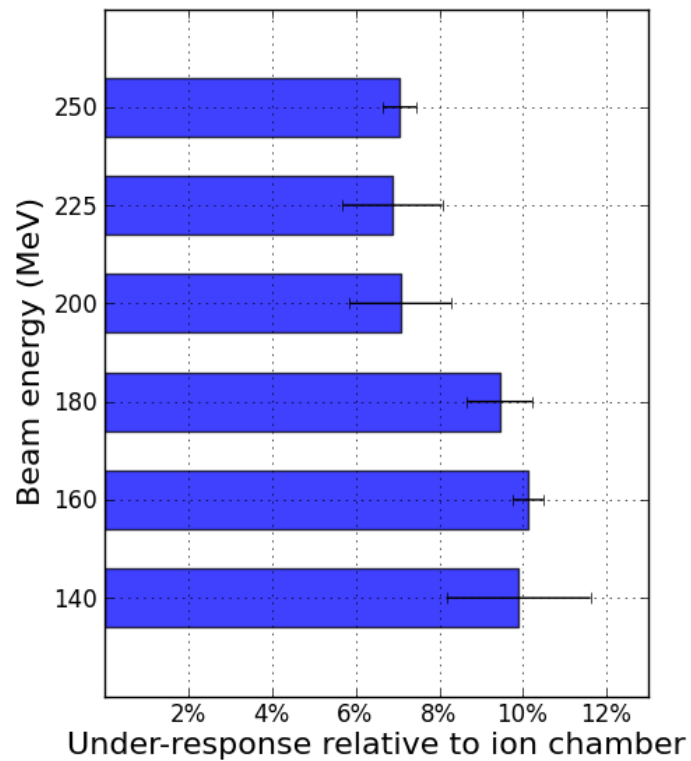


Figure 5.1. Plastic scintillation detector under-response relative to the dose measured with a plane-parallel ion chamber at the surface of an acrylic block. The under-response increased from 7% at 250 MeV to 10% at 140 MeV and was fairly constant for energies above 200 MeV and below 180 MeV. Error bars indicate 1 standard deviation.

5.3.2 Response vs SOBP Width

The dose measured by the PSD relative to the dose measured by the ion chamber did not change appreciably as a function of SOBP width for either the 225 MeV beam or the 140 MeV beam, with one possible exception. The dose measured by the PSD for the 10 cm wide SOBP configuration of the 140 MeV beam, which has a 10 cm range in water, decreased to 89% of the dose measured by the ion chamber, compared with 90% of the dose measured by the ion chamber for other SOBP widths. However, given the uncertainty of the measurements, the decrease to 89% may not be due to the SOBP width. The dose measured by the PSD was approximately 93% of the dose measured by the ion chamber for the 225 MeV beam and 90% of the dose measured by the ion chamber for the 140 MeV beam, in good agreement with the measured values from the previous section. Detailed results are presented in figure 5.2.

5.3.3 Cerenkov Light Contribution

Increasing the optical fiber in the proton field from 6 cm to approximately 20 cm resulted in a small change in the channel readings for the 140 MeV beam. A 0.2% increase in blue channel signal, a 2.5% increase in green channel signal, and an overall 0.9% increase in light output was observed. The same procedure resulted in a slightly larger change for the 250 MeV beam: a 1.7% increase in blue channel signal, a 3.1% increase in green channel signal, and an overall 2.1% increase in light output. These results are presented in figure 5.3. The absolute signal of the blue channel was about twice that of the green channel, which is why the blue channel contributed more to the overall increase in signal.

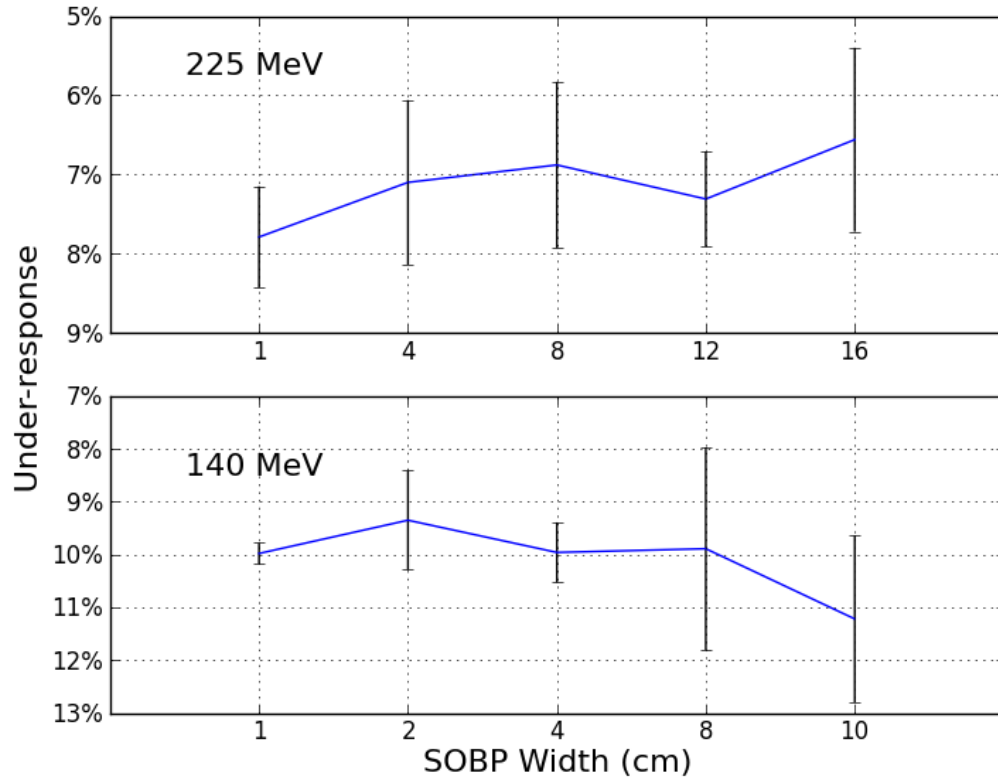


Figure 5.2. Plastic scintillation detector (PSD) under-response relative to a plane-parallel ion chamber for a variety of spread out Bragg peak (SOBP) widths. No meaningful change was observed in the PSD response for the 225 MeV beam. For the 140 MeV beam, the under-response was consistently 10% for all but the 10-cm SOBP, for which it increased to 11%. However, the uncertainty in the measurements precludes definitively concluding that this effect is real.

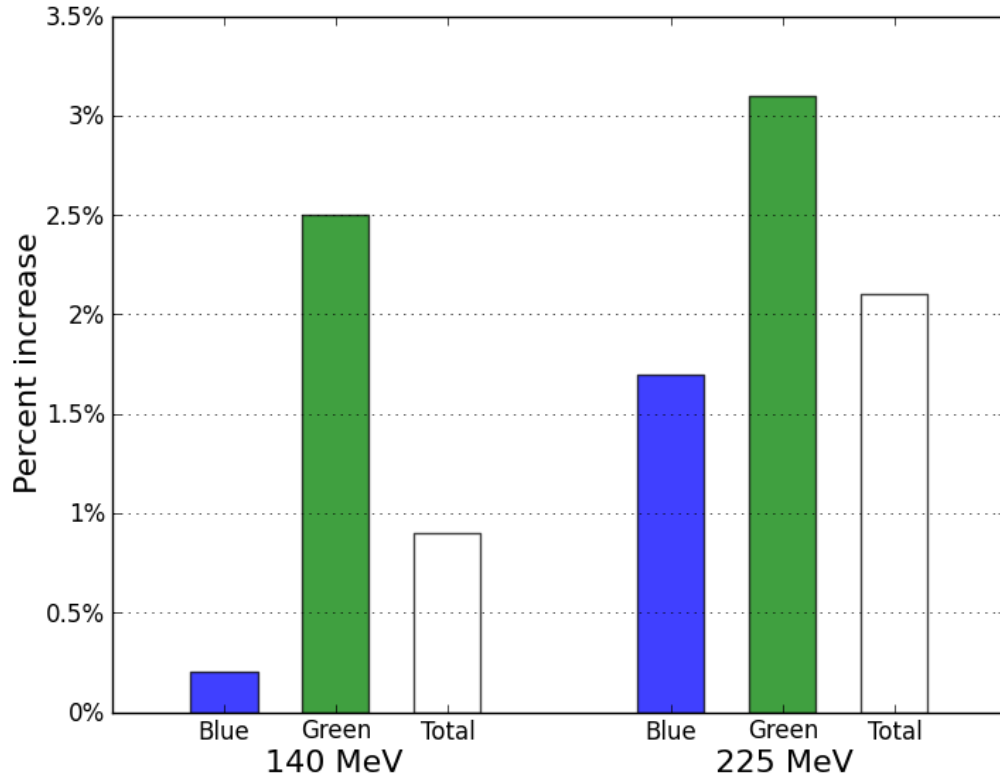


Figure 5.3. Percent change in the blue and green channel output and overall light output when approximately 3 times as much fiber is irradiated (20 cm vs 6 cm). Although the total increase in light output doubled between the 140 MeV and 225 MeV beams, the increase was small in both cases (2% and 1%), indicating that although Cerenkov light was present, it contributed very little to the total light signal.

Calibrating the PSD on the basis of total light output (i.e., assuming no Cerenkov light) per dose revealed that the contribution of Cerenkov to measured dose was very small. This calibration factor was used to calculate dose measured at higher energies, and after ionization quenching was accounted for, the measured dose did not deviate from the actual dose by more than 1% at any energy (Figure 5.4).

5.3.4 Profile Measurements

The lateral beam profiles measured using the PSD were in excellent agreement with those measured using film for both the 225MeV beam and the 140 MeV beam; the film measurements fell within the uncertainty of the PSD measurements. Both profiles are plotted in figures 5.5 and 5.6.

5.3.5 SNR

For the 250 MeV beam, the SNR value (calculated as the standard deviation of repeated measurements divided by the average signal) was 7 for the 1-MU irradiation, 30 for the 10-MU irradiation, and 385 for the 100-MU irradiation, with 1 MU corresponding to a dose of 0.67 cGy. For the 140 MeV beam, the SNR values were 19 for the 1-MU irradiation, 169 for the 10-MU irradiation, and 294 for the 100-MU irradiation, with 1 MU corresponding to 0.63 cGy. The noise, quantified by taking the standard deviation of sets of 3 measurements, was consistent regardless of the dose delivered (approximately 0.2 cGy). Thus, the SNR of the detector appeared to be largely a function of the dose.

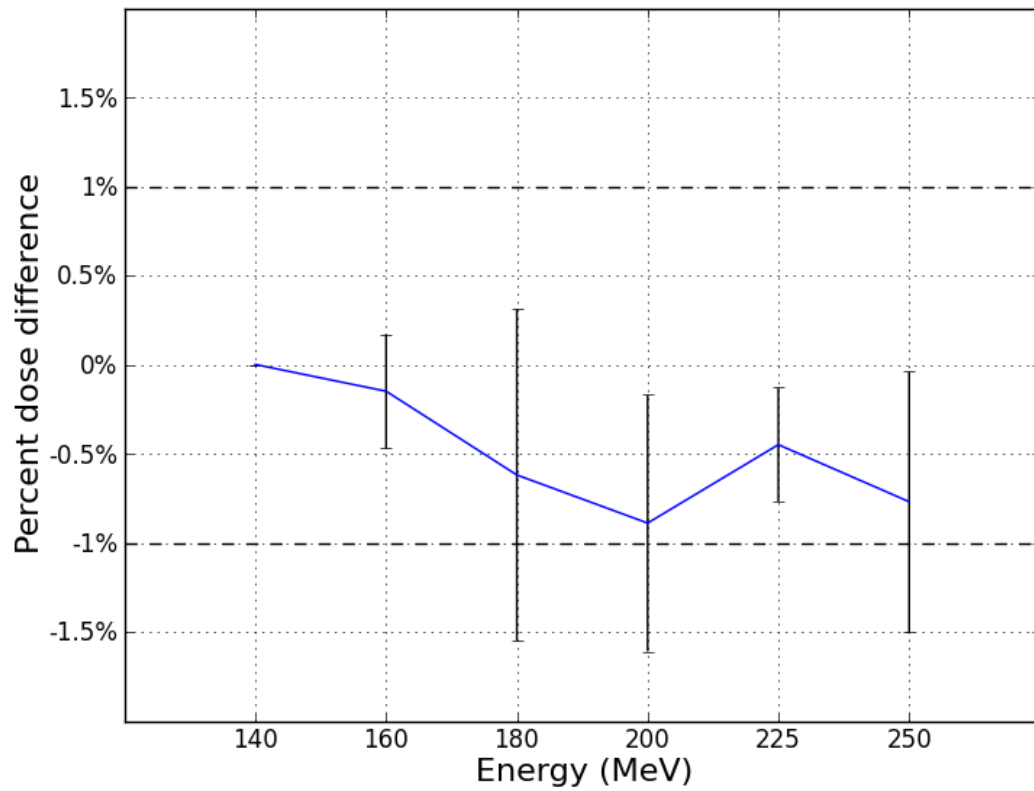


Figure 5.4. Error introduced into dose measurements by ignoring Cerenkov light. A simple total light to dose calibration was performed at 140 MeV and retroactively applied to dose measurements at higher energies. This introduced less than 1% error to the measured dose.

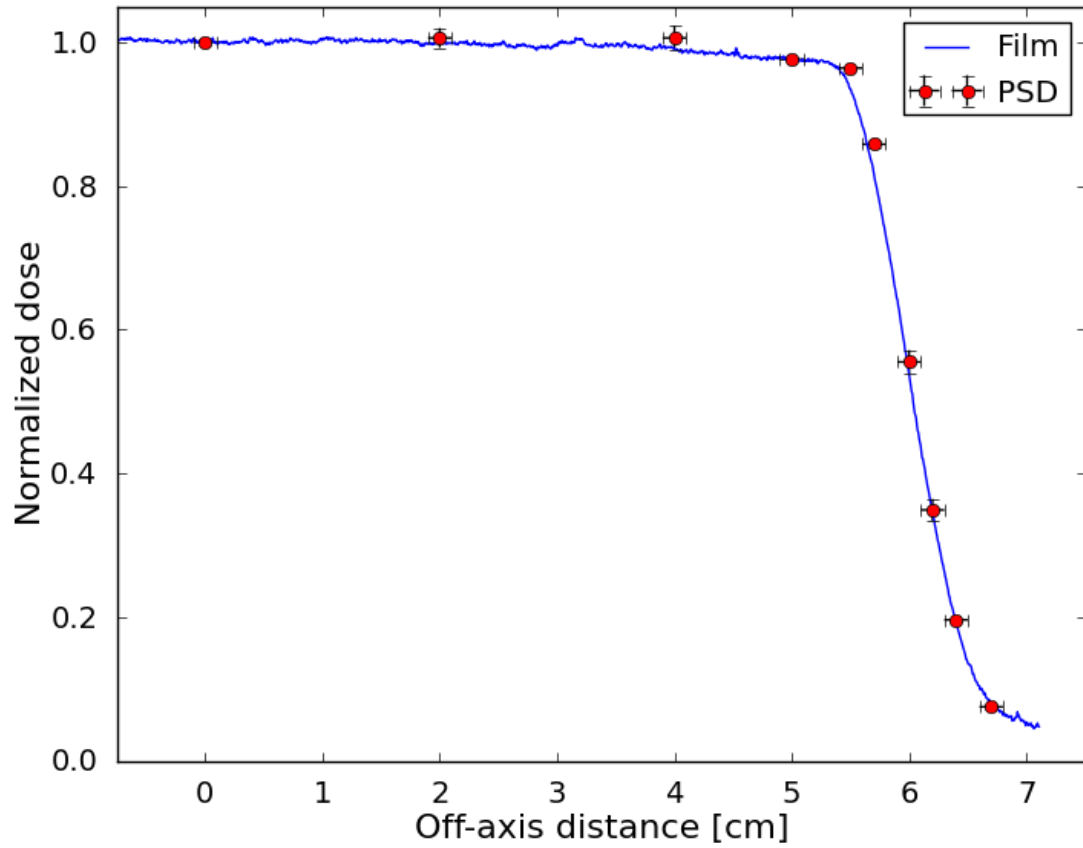


Figure 5.5 Film and plastic scintillation detector (PSD) measurements of the lateral beam profile acquired at 225 MeV. Horizontal error bars represent a ± 1 mm uncertainty in the positioning of the PSD. Vertical error bars are 1 standard deviation of the PSD measurements. The film measurements agree to within the uncertainty of the PSD measurements.

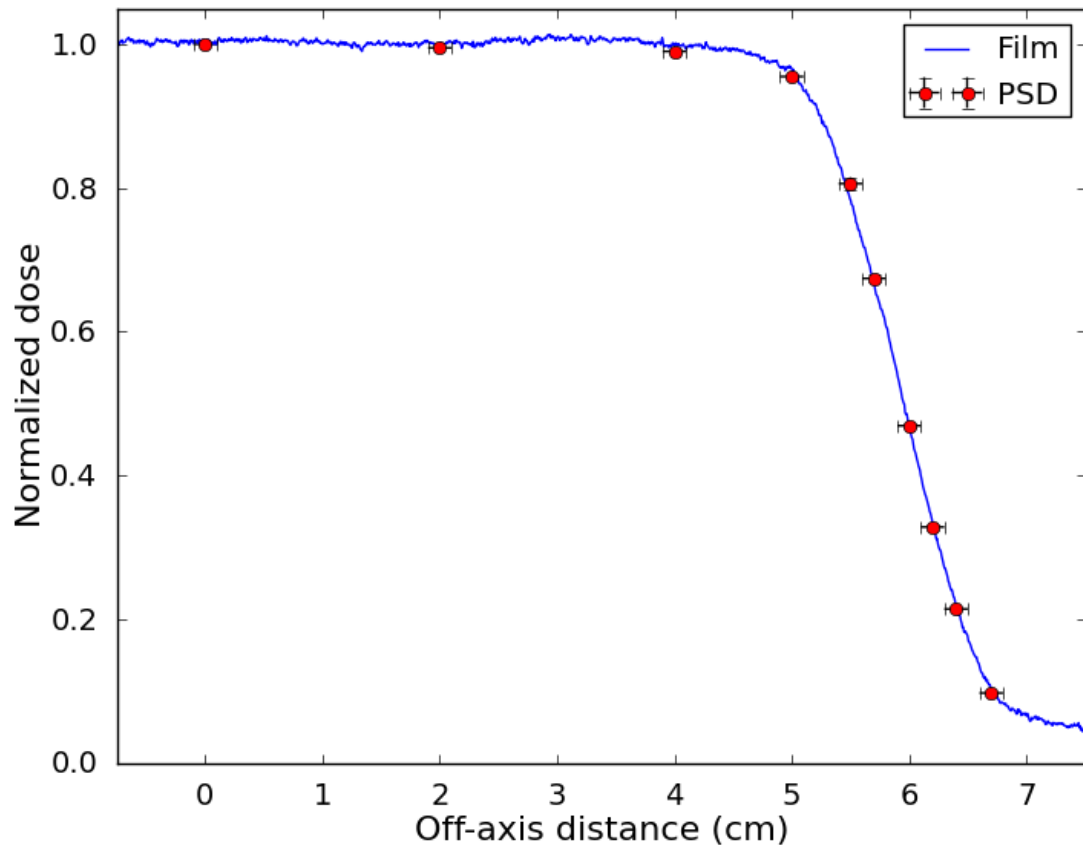


Figure 5.6 Film and plastic scintillation detector (PSD) measurements of the lateral beam profile acquired at 140 MeV. Horizontal error bars represent a ± 1 mm uncertainty in the positioning of the PSD. Vertical error bars are 1 standard deviation of the PSD measurements. The film measurements agree to within the uncertainty of the PSD measurements.

5.4 Discussion

Our results showed that although ionization quenching correction factors were needed for PSD dosimetry, the PSD measured the lateral beam profile accurately and SOBP width variation and Cerenkov light contributed negligibly to the performance of the PSD, indicating that PSDs represent a practical solution for proton entrance dosimetry.

As expected, ionization quenching was found to be responsible for a non-negligible loss of signal in the PSD at all energies. This result is in agreement with the literature; Archambault *et al.* (2008) performed Monte Carlo calculations to determine linear energy transfer in proton beams and used the Birks quenching correction formula to predict an under-response of 13% at the entrance for energies between 150 MeV and 250 MeV on the basis of the Birks formula. This under-response is greater than what we observed. However, Archambault *et al.* applied the semi-empirical Birks formula under different conditions than those used in our study. Thus, some discrepancy in the absolute value of the under-response is not surprising.

Although ionization quenching effects are present at all proton energies, the correction required to determine the entrance dose is straightforward relative to those required to measure depth-dose curves. For depth-dose measurements, Monte Carlo is used to determine linear energy transfer values for a proton beam of interest, and then these values are used to calculate quenching correction factors using the Birks formula. These factors are then applied to measured values. The quenching correction factors increase rapidly at the end of a proton beam, so for measurements to be corrected effectively, the position of the PSD in the beam must be known with a high degree of accuracy. In contrast, our results show that one correction factor could be used with an

accuracy of $\pm 1\%$ for nominal beam energies of 200 MeV to 250 MeV for all SOBP widths. A second correction factor would be sufficient for beams with energies of 140 MeV to 180 MeV with the same 1% accuracy.

Furthermore, the range of correction factors for entrance dosimetry is narrow compared with those required for depth-dose measurements. In our study, ionization quenching at the surface resulted in 7% to 11% loss of signal for all energies and SOBPs considered. In contrast, the ionization quenching calculated by Archambault *et al.* (2008) in a 150 MeV pristine beam resulted in 13% loss of signal at the entrance and 30% loss of signal at the Bragg peak.

Variation in the SOBP width did not have an observable effect on ionization quenching. In the 140 MeV beam, the under-response increased to 11% from 10% for the widest SOBP, but because of the uncertainty in the measurements, it cannot be definitively concluded that this effect is real. However, there is a physical reason to suspect that the effect might be real: the SOBP width was equal to the beam range in water, bringing the most proximal Bragg peak to the surface. Regardless, even if the effect is real, the difference is very small. The likely reason for the lack of influence of the SOBP width on ionization quenching is the energy distribution of protons required to achieve the SOBP. The highest energy protons, corresponding to the most distal portion of the beam, contribute more dose at the surface than any other portion of the beam. This is because the highest energy protons must supply the full dose at the distal end of the beam, whereas lower energy protons (corresponding to more proximal regions of the beam) need only supply the difference between the desired dose and the dose contributed by higher energy protons. For this reason, for very wide beams, the most proximal Bragg

peak, or the lowest energy component of the SOBP, contributes only a very small amount to the entrance dose. This is illustrated in figure 5.7.

Cerenkov light was demonstrated to be essentially negligible for our setup, in agreement with prior studies using PSDs for relative dosimetry. A relatively large field was used and the measurements were performed at the surface, which constitute a worst-case scenario in terms of Cerenkov contamination. Therefore, it is unlikely that Cerenkov light is an important consideration when using PSDs for proton beam dosimetry under any circumstances. The source of the Cerenkov light is not the protons themselves because the threshold energy (determined as the energy necessary for the protons to move faster than the local speed of light in media) for Cerenkov production is approximately 320 MeV. However, the required energy for electrons to produce Cerenkov light is only 0.175 MeV owing to the smaller mass of electrons relative to protons (these calculations assume an index of refraction of 1.5, which corresponds to PMMA, polyethylene, and many other plastics that are used as optical fiber). The maximum secondary electron energy for a given proton energy can be calculated (Beringer *et al.* 2012), and doing so reveals that 250 MeV and 140 MeV monoenergetic proton beams can produce electrons with maximum energies of 0.616 (250 MeV beam) and 0.352 MeV (140 MeV beam). Thus, some of the secondary electrons produced will be capable of producing Cerenkov light. However, most of the secondary electrons produced will be of much lower energy and will not produce Cerenkov light. For this reason, the quantity of Cerenkov light produced in proton beams is much lower than that of photon or electron beams.

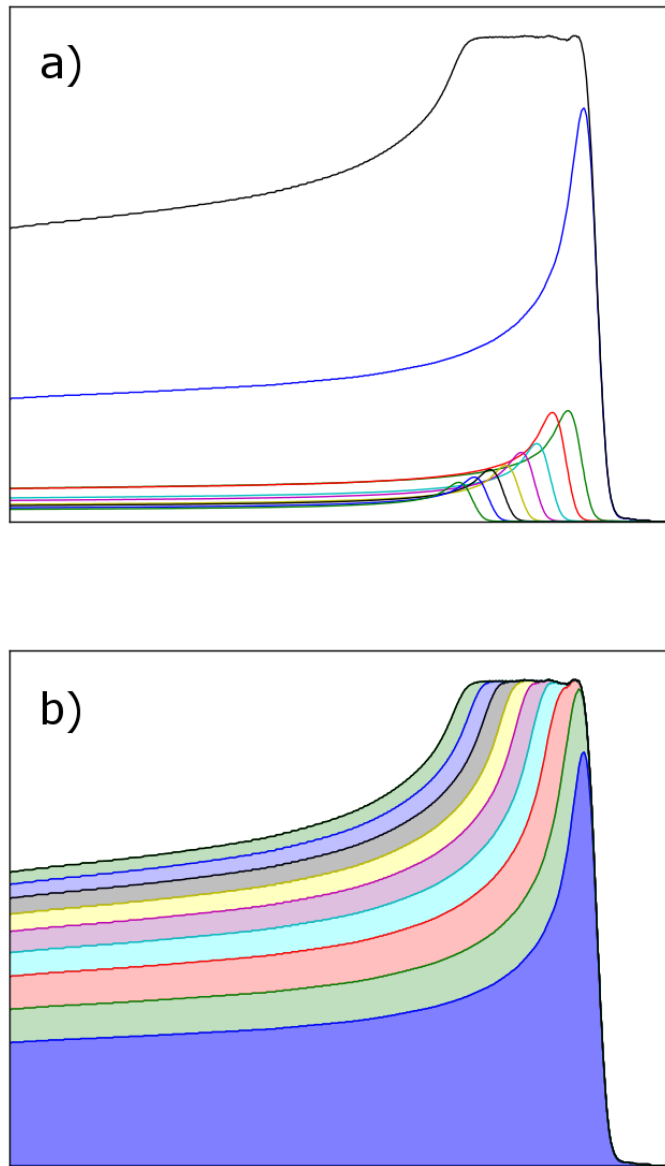


Figure 5.7 Dose deposition curves for a hypothetical SOBP and its constituent pristine Bragg peaks plotted side by side (a) and stacked from most distal to most proximal (b). It can be seen that the most distal Bragg peak contributes disproportionately more entrance dose than other beams (left side of the plot), and that the contribution to entrance dose by each increasingly proximal Bragg peak diminishes.

The profile measurements in our study demonstrate the high spatial resolution and sensitivity of the PSD, without which accurate measurements of the beam penumbra would be difficult. Furthermore, the good agreement between profiles measured using the PSD and those measured using film at all locations implies that the results obtained on the central axis of the beam (with regard to ionization quenching and Cerenkov light) can be generalized to a PSD measuring the entrance dose off axis. If this were not the case, the relative profiles would not be expected to agree.

The SNR of the PSD was reduced by ionization quenching (an unsurprising result given that quenching reduces the scintillation signal), but the SNR was still excellent (>200) at all energies for moderate doses (100 MU corresponded to approximately 60 cGy).

One limiting factor in the current study is that many of the results are differences between 2 measurements, namely the dose measured by an ion chamber and the dose measured by a PSD, increasing the relative uncertainty. Both the ion chamber and the PSD measured dose with high precision, but subtracting the dose measured by the PSD from the dose measured by the ion chamber resulted in a quantity that was both smaller and noisier than the dose measured by either the PSD or the ion chamber. This made obtaining highly precise results difficult and limited the effects that could be observed. For example, if more precise results were obtained, one might expect to see a small but definite increase in ionization quenching for increasing SOBP widths. Nonetheless, the uncertainty in the results obtained was generally $\pm 1\%$, which is adequate for dosimetry.

The possibility of direct calibration in the proton beam should also be considered. Ionization quenching would be directly accounted for in the calibration, and because the

variation in quenching for different energies is slight, a calibration at one energy may be appropriate for measurements at other nearby energies. A direct calibration would also be expected to have an improved SNR, because the total spectrum rather than the difference between 2 portions of the spectrum would constitute the signal. This is possible because of the minimal contribution of Cerenkov light to the total light output.

5.5 Conclusion

Because the PSD has been demonstrated to be a good *in vivo* detector in prior studies and because we have shown here that PSDs can be used for entrance dosimetry for proton fields without undue difficulty, we believe that PSDs are a good candidate for *in vivo* entrance dosimetry in patients undergoing proton therapy. PSDs are small and water equivalent, so the beam should not be perturbed in a clinically significant manner, and skin dose results would be available immediately following treatment. This may prove helpful in assessing the risk of radiation dermatitis for patients undergoing treatment. PSDs for *in vivo* entrance dosimetry would also be capable of detecting gross errors during dose delivery. Unfortunately, other treatment parameters such as beam range could not be verified with such a system. Nonetheless, we believe that PSDs could serve as a useful tool to perform *in vivo* entrance dosimetry.

CHAPTER 6

CONCLUSION

6.1 Summary and Conclusions

The work presented in this dissertation represents a significant step towards implementing plastic scintillation detectors for general use as *in vivo* dosimetry devices in external beam radiation therapy. Three specific projects were undertaken as steps towards this goal: characterization and correction of the temperature dependence of common scintillating fibers, a clinical protocol employing the PSD as an *in vivo* dosimeter for patients undergoing prostate radiation therapy, and a characterization of the performance of PSDs in the context of proton skin dosimetry.

The first study demonstrated that, in contrast with prior knowledge, two scintillating fibers commonly used in PSDs exhibit temperature dependence. The temperature dependence was found to be approximately linear with temperature. The first, BCF-60, was found to lose 0.5% of its signal with each °C increase in temperature, relative to 22°C. BCF-12 was found to lose 0.09% with each °C increase. This corresponds to a 7.5% and 1.4% under-response at body temperature, respectively. The shape of the scintillation spectrum was found to change slightly for each scintillating fiber. This effect was small however, and it was suggested that a simple correction factor consisting of the ratio of dose measured at a given temperature to that at a reference temperature was sufficient to account for this effect.

The second study utilized PSDs to perform *in vivo* dosimetry for patients undergoing IMRT for prostate cancer. Pairs of PSDs were attached to endorectal balloons which were then inserted into patient's rectums for the duration of each fraction of treatment. This positioned the PSD pair in close proximity with the rectal wall where they were used to measure the dose delivered during treatment. Temperature correction factors

derived from the previous study were used to ensure accurate results. Prior to each treatment, a CT image set was acquired for the purpose of locating and determining the expected dose to each detector. This procedure was repeated twice weekly for five patients, generating a total of 142 *in vivo* measurements.

The average difference between the expected dose and the measured dose ranged from -3.3% to 3.3% over the five patient population. The standard deviation fell between 5.6% and 7.1% for four of the five patients, and was 13.9% for the fifth patient for reasons explained in detail in chapter 4. The average difference over all five patients was -0.4% with a standard deviation of 2.8%. The implementation of an *in vivo* dosimetry system did not interrupt or alter the clinical workflow, and the patients reported that the detectors attached to endorectal balloons were as tolerable as the endorectal balloon alone.

During the course of this study, a method of localizing the detector using three ceramic fiducials attached in a rigid geometry was implemented. This was necessary because PSDs are radiographically indistinguishable from tissue as a result of being water equivalent. When experimentally validated in an anthropomorphic phantom, this method localized detectors to within 1 mm in the lateral and anterior-posterior directions, exhibiting an average deviation of just 0.1 mm from the true location.

The final study investigated the use of PSDs for entrance dosimetry in proton beams. Of particular interest was the problem of ionization quenching, an under-response when measuring dose delivered by high LET radiation. Comparisons between ion chamber measurements and PSD measurements revealed that PSDs under-respond by 7% to 10% at the entrance of passively scattered proton beams of energies between 140 MeV

and 250 MeV, with lower energy beams producing a greater under-response. The width of the spread out Bragg peak was found to have a negligible effect on the magnitude of the under-response. In spite of the reduced signal due to ionization quenching, the PSD was found to exhibit excellent relative accuracy and a high SNR. On the basis of this work it is expected that the PSD can be used effectively as an *in vivo* skin dosimeter in proton therapy with the use of empirically determined ionization quenching correction factors or direct calibration in the proton beam of interest.

Overall, this work has demonstrated that two non-negligible response-altering effects can be accurately corrected for, permitting high accuracy *in vivo* dosimetry. Furthermore, it has been demonstrated that PSDs are effective and practical when used for *in vivo* dosimetry, producing accurate results even when placed in a high dose-gradient region such as the rectal wall in prostate intensity modulated radiation therapy.

6.2 Future Directions

Each of the three specific aims carried out for this work suggest future avenues of productive research. Temperature dependence and proton entrance dosimetry will be considered first. The *in vivo* protocol is saved for last because of the large number of rich possibilities to cover.

It has been demonstrated that PSDs using BCF-12 and BCF-60 scintillating fibers exhibit a thermally induced loss of signal that can be accounted for with temperature specific correction factors. This is an effective solution, as demonstrated by the excellent results obtained during the *in vivo* protocol outlined in chapter 4. Ideally however, a PSD would be temperature independent and no correction factor would be needed. The fact

that the original PSD studied by Beddar *et al.* (1992a) exhibited negligible temperature dependence suggests this is possible. This PSD used plastic scintillator (BC-400), rather than scintillating fiber. The theoretical downside of plastic scintillator is inferior light collection properties resulting from a lack of cladding. Therefore a PSD using plastic scintillator may have a somewhat weaker signal. A PSD using BC-400 should nevertheless produce adequate signal to be useful for *in vivo* dosimetry. To this end, the temperature independence of BC-400 should be independently verified. It may also be possible to fabricate a temperature independent scintillating fiber. It would require a base other than polystyrene as pure polystyrene has been found by others to exhibit temperature dependence as well (Rozman and Killin 1960). Polyvinyltoluene is a good candidate, as it is the base in BC-400. Such a scintillating fiber would be ideal for *in vivo* dosimetry with PSDs and warrants further research.

It has also been demonstrated that PSDs are capable of accurate entrance dosimetry in proton beams. An obvious next step is to use PSDs to measure skin dose as part of a clinical protocol. Of particular interest is investigating the claim made by Whaley *et al.* (2013) that a transparent film dressing can lessen the severity of radiation dermatitis. The authors of that study noticed that the radiation dermatitis for two patients treated for prostate cancer was significantly reduced underneath transparent adhesive markers used for alignment. A phantom study was performed and did not detect any change in dose deposition with or without the adhesive dressing. The authors do not posit a mechanism for this effect. PSDs can be used for a larger, systematic study of this effect with *in vivo* measurements of dose with/without dressing rather than phantom measurements.

The entrance dosimetry study also suggests a few more basic avenues of future research. One is the extension of these measurements to spot scanning proton beams. Spot scanning is an increasingly popular proton therapy modality due to a diminished neutron dose and an improved ability to conform the delivered dose to the tumor. Another is investigation of possible solutions to ionization quenching. Currently the use of PSDs in proton beams requires measured correction factors (as put forth in chapter 5), or advance knowledge of the proton beam LET so that correction factors can be calculated. A spectral characterization of quenching could be performed to identify whether the scintillator base or the wavelength shifting fluors are responsible for the loss of signal. This information could be used to formulate a scintillator less sensitive to ionization quenching. Alternatively, if two scintillators are found that under-respond differently for a given LET, the two could be used in concert to determine the quantity of quenching taking place by comparing the ratio of their responses relative to a reference condition. Finally, if progress is made on correcting ionization quenching, an *in vivo* study could be performed using PSDs for internal measurements rather than skin measurements. PSDs placed internally can be in close proximity to the target or organs at risk, providing more useful measurements. This is particularly important in proton therapy, as protons have a finite range and measurements at the surface are not indicative of dose at depth because of the sensitivity of protons to the media they are passing through.

Finally, much work could be done based on the *in vivo* protocol presented in chapter 4. To begin, having demonstrated that PSDs perform well as *in vivo* detectors, it stands to reason that there are many useful *in vivo* applications outside of prostate

radiation therapy. New treatment sites may benefit from *in vivo* dosimetry such as head and neck cancers. Head and neck cancer involves many organs at risk in close proximity to targets, and anatomical changes over the course of treatment (due to weight loss for example) alter the dose distribution, sometimes requiring replanning. An *in vivo* PSD could be used to determine when anatomical changes are significant enough to require replanning or to monitor the dose to organs at risk.

Another use of PSDs for *in vivo* dosimetry of great interest would be in stereotactic radiosurgery or stereotactic body radiation therapy (SRS and SBRT respectively). SRS and SBRT both use high doses spread over fewer fractions, often administered by small fields. High dose gradients are used to achieve sparing of healthy tissue. The success of SRS and SBRT depends on the accurate delivery of radiation through image guidance and patient immobilization. PSDs could be used *in vivo* to verify that radiation is being delivered correctly. Interrupting treatment when an error is detected would be of greater benefit in SRS/SBRT than other modalities. As there are fewer fractions, the consequences of misadministering one fraction is significantly higher.

Lastly, PSDs are a natural candidate to be used with MRI-Linacs *in vivo*. The MRI can be used to track the position of the PSD during treatment delivery, and the PSD to verify the dose delivered.

Another route of research is implementing new PSD technology for use in *in vivo* PSDs. In particular, the multi-point PSD (Therriault-Proulx *et al.* 2012), or mPSD, would be useful as it allows the measurement of dose at multiple distinct points but uses only

one optical fiber. More points of measurement offer a better verification of the dose delivered.

Though not unique to PSDs, additional research on the analysis and interpretation of *in vivo* measurements will be important going forward. For example, establishing action limits for different treatment sites based on the capabilities of the detector will be necessary to maximize the detection of errors while minimizing false positives. The implementation of an automated error detection system for *in vivo* PSDs similar to the one described by Kertzschner *et al.* (2014) may increase the utility of PSDs for *in vivo* dosimetry and decrease the time cost associated with it. Finally, research into what types of error cannot be detected with *in vivo* dosimetry is important. For example, if a dosimetrist creates a plan with the wrong prescription dose and that plan is delivered correctly, *in vivo* dosimetry will not draw attention to this error. As part of improving patient safety, it is vital that the limitations of *in vivo* dosimetry are well understood to preclude a false sense of confidence.

Finally, perhaps the most useful avenue of investigation to move PSDs from the lab into the clinic is the study and characterization of commercial PSDs for *in vivo* applications. A new endorectal balloon with PSDs embedded in the balloon lumen is already available (Klawikowski *et al.* 2014), and warrants investigation.

APPENDIX

A – Derivation of Approximate Energy Level Spacing via the Free Electron

Perimeter Model

The pi-bonds parallel to the plane of an aromatic hydrocarbon allow electrons to move freely along the perimeter of the molecule. If the perimeter of the molecule is approximated as a circle, the wavefunction of the electrons must satisfy the following relationship:

$$\psi(\theta) = \psi(\theta + 2\pi) \quad (\text{A.1})$$

where θ is the angular position of an electron along the circle. This simply means that the wavefunction can take only one value at a given point on the circle. The wavefunction must therefore be either periodic or constant. Equation A.2 satisfies this requirement:

$$\psi(\theta) = C \cdot e^{iq\theta} \quad (\text{A.2})$$

In this equation q is a quantum number to allow any periodicity and C is a normalization constant. The energy levels, E , associated with this wavefunction can be obtained by solving the Schrödinger equation, $E\psi = H\psi$, where H is the Hamiltonian operator. If the circle is assumed to be equipotential, the only term in the Hamiltonian is the kinetic energy. When this Hamiltonian is expressed using quantum mechanical operators in angular coordinates, the Schrödinger equation becomes:

$$E\psi = \frac{-\hbar^2}{2m} \frac{1}{r^2} \frac{\partial^2 \psi}{\partial \theta^2} \quad (\text{A.3})$$

The differential on the right side can be evaluated to determine the energy levels.

$$\frac{\partial^2 \psi}{\partial \theta^2} = \frac{\partial^2}{\partial \theta^2} C e^{iq\theta} \quad (\text{A.4})$$

$$= -q^2 C e^{iq\theta} \quad (\text{A.5})$$

$$= -q^2 \psi \quad (\text{A.6})$$

Substituting this into equation A.3 gives the final expression (note that ψ cancels out):

$$E = \frac{\hbar^2 q^2}{2mr^2} \quad (\text{A.7})$$

With this equation in hand, consider benzene. Benzene has six pi electrons. Since each electron can take on one of two spin values and can move in one of two directions around the perimeter of the molecule (for states with $q > 0$), each state with $q > 0$ is doubly degenerate, and the $q = 0$ state is singly degenerate (Birks 1964). The lowest energy configuration consists of two electrons occupying $q = 0$, and four electrons occupying $q = 1$. This is the base state of the molecule. Excitation of a pi electron from $q = 1$ to $q = 2$ corresponds to the first excited state of the molecule (S_1 in figure 2.3). De-excitation is responsible for scintillation. If the electron mass and approximate radius of benzene are substituted into equation A.7 for $q = 1$ and $q = 2$, the difference in the calculated energies is 6.4 eV. This is close to the actual transition energy of 4.8 eV despite the simplifying assumptions made.

B – The Chromatic Removal Technique

For a rigorous treatment of the chromatic removal technique, the reader is referred to the following three references: Fontebonne et al. 2002, Frelin et al. 2005, and Archambault et al 2006. What is presented here is meant as an aid to understanding why this method works. It assumes familiarity on the part of the reader with linear algebra.

The signal produced by a PSD is a combination of scintillation light, which is directly proportional to the dose delivered, and Cerenkov light, which depends on many factors. The total light output is therefore an inappropriate measure of the dose delivered. The chromatic removal technique overcomes this difficulty using the fact that the spectral distributions of Cerenkov light and scintillation are constant (Figure B.1), and that the intensity of one is independent of the intensity of the other. These facts allow the mathematical extraction of the correct dose from a signal contaminated by arbitrary amounts of Cerenkov light.

To do this, the light generated by a PSD must be split into two spectrally distinct components. This may be accomplished with a dichroic mirror or other optical filter. For the purpose of explanation, consider a dichroic mirror that transmits light between 500 nm and 600 nm and reflects everything else. The transmitted light will be referred to as the ‘green’ signal, and the reflected the ‘blue’ signal for the sake of simplicity. Each measurement made with a PSD in this setup can then be considered a vector in ‘blue-green’ vector space.

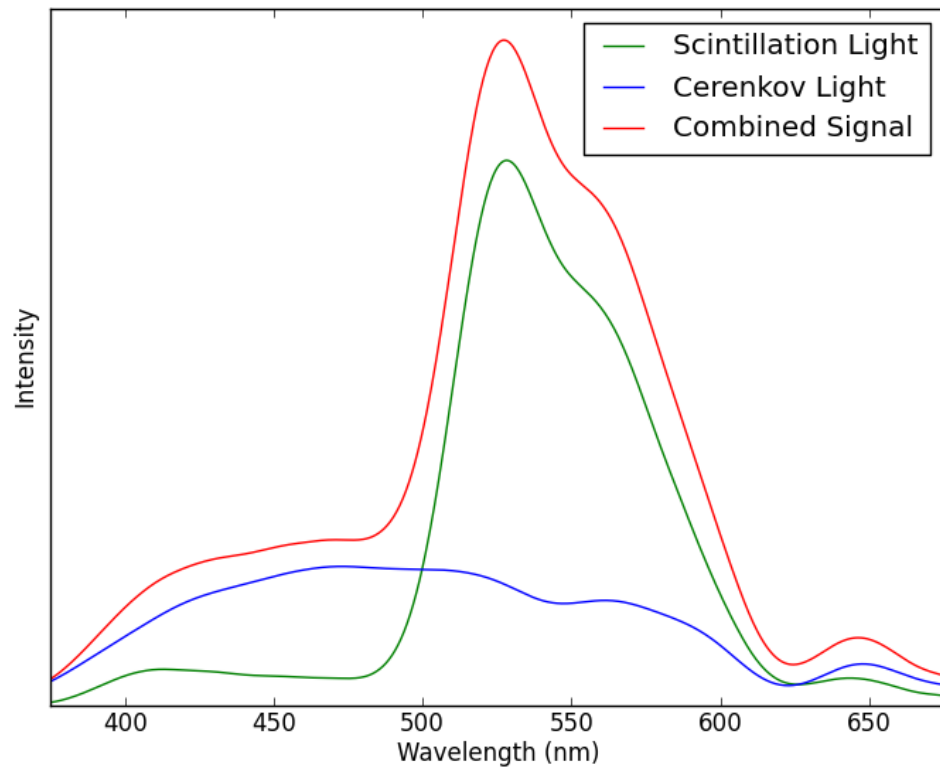


Figure B.1. The signal from a PSD obtained with a spectrometer is plotted in red. The signal is a combination of scintillation light (green) and Cerenkov light (blue). The shape of the scintillation and Cerenkov spectra do not change; the combined signal is always a linear combination of the two.

If the scintillation spectrum were split by our hypothetical dichroic mirror, it would result in a vector in blue-green space. The length of this vector would vary with the intensity of scintillation light, but its direction would be constant because the spectral distribution of scintillation light is constant (Figure B.2). This vector can be considered a basis vector corresponding to scintillation. The same reasoning can be applied to generate a Cerenkov basis vector. It is therefore possible to mathematically transform blue-green space into a space defined by the scintillation and Cerenkov basis vectors. To do so, the blue-green vector space is left multiplied by the inverse of a matrix containing the scintillation and Cerenkov light basis vectors expressed in blue-green coordinates:

$$\begin{bmatrix} S_b & S_g \\ C_b & C_g \end{bmatrix}^{-1} \begin{bmatrix} B \\ G \end{bmatrix} = \begin{bmatrix} S \\ C \end{bmatrix} \quad (\text{B.1})$$

For reasons that will be made clear presently, variables will be substituted for the values of the inverted matrix:

$$\begin{bmatrix} F_{11} & F_{12} \\ F_{21} & F_{22} \end{bmatrix} \begin{bmatrix} B \\ G \end{bmatrix} = \begin{bmatrix} S \\ C \end{bmatrix} \quad (\text{B.2})$$

If the matrix multiplication is carried out in equation B.2 it results in two equations. The first relates the intensity of scintillation light to the measured blue and green components of the total light signal. The second does the same for Cerenkov light can be discarded. The first equation is:

$$F_{11}B + F_{12}G = S \quad (\text{B.3})$$

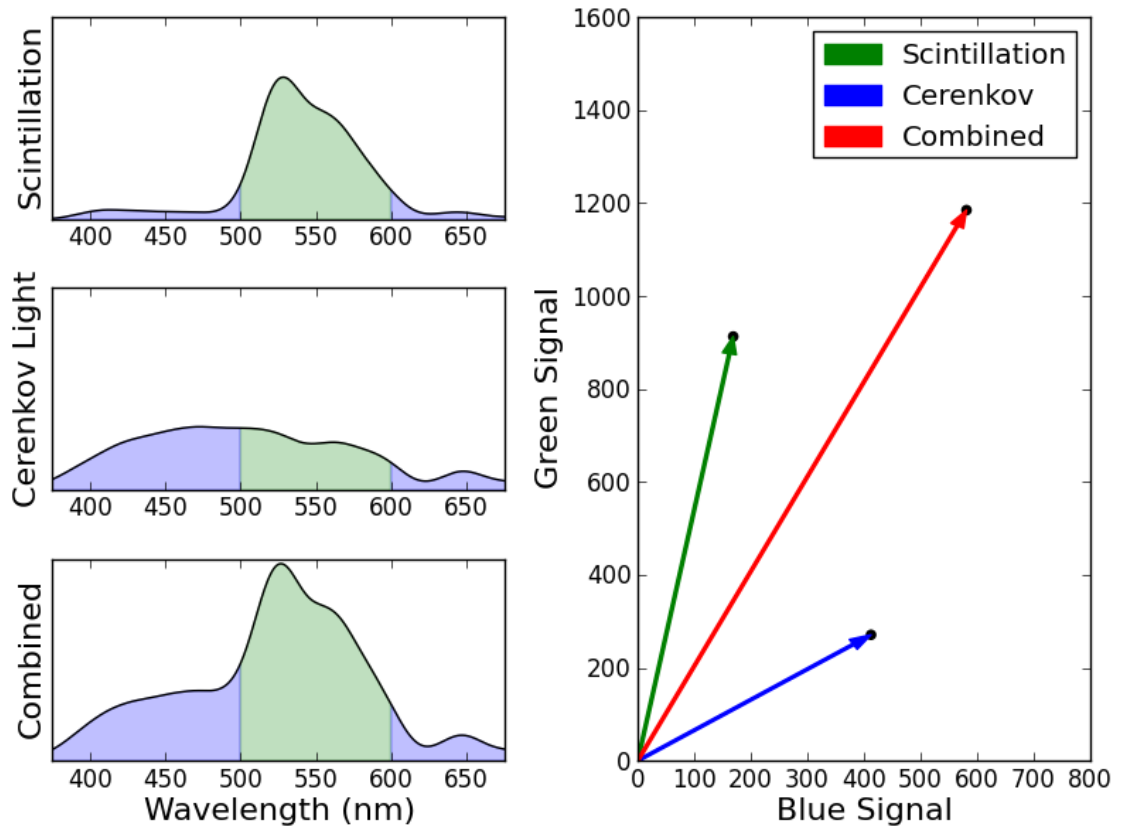


Figure B.2. On the left, the spectra of scintillation light, Cerenkov light, and the combined signal are plotted. The intensity of light between the wavelengths of 500 and 600 nm (the ‘green’ signal) is represented by the green shading in each of the three plots. This corresponds to the light that would be transmitted by a hypothetical dichroic mirror. Likewise, the light that would be reflected is represented by blue shading (the ‘blue’ signal). The blue and green intensities of each spectrum are used to generate vectors in ‘blue-green’ vector space. The direction of the scintillation vector will not change as the intensity of scintillation changes, only the length. The same is true for Cerenkov light. The vector corresponding to the combined signal can take on a range of directions however, corresponding to the relative intensities of the underlying scintillation and Cerenkov components.

If equation B.3 is multiplied by the ratio of dose to scintillation light a new equation is obtained relating the blue and green components of the total light signal directly to dose.

$$\frac{D}{S} (F_{11}B + F_{12}G) = \frac{D}{S} (S) \quad (\text{B.4})$$

$$F'_{11}B + F'_{12}G = D \quad (\text{B.5})$$

Thus it is possible to determine the dose delivered from the blue and green signal. By performing measurements under known dose conditions, the factors F'_{11} and F'_{12} can be empirically determined. Doing so is easier than directly evaluating the value of the 2x2 matrix in equation B.1, as it is difficult to obtain a pure scintillation spectrum without special equipment (Therriault-Proulx *et al.* 2012). Once the factors are obtained, equation B.5 can be used to accurately measure dose with the PSD in the presence of arbitrary quantities of Cerenkov light.

BIBLIOGRAPHY

- Archambault L, Arsenault J, Gingras L, Beddar AS, Roy R, Beaulieu L 2005. Plastic scintillation dosimetry: Optimal selection of scintillating fibers and scintillators. *Med. Phys.* **32** 2271-2278.
- Archambault L, Beddar AS, Gingras L, Roy R, Beaulieu L 2006 Measurement accuracy and Cerenkov removal for high performance, high spatial resolution scintillation dosimetry. *Med. Phys.* **33** 128-135.
- Archambault L, Beddar AS, Gingras L, Lacroix F, Roy R, Beaulieu L 2007. Water-equivalent dosimeter array for small-field external beam radiotherapy. *Med. Phys.* **34** 1583-1592.
- Archambault L, Briere TM, Beddar AS 2008. Transient noise characterization and filtration in CCD cameras exposed to stray radiation from a medical linear accelerator. *Med. Phys.* **35** 4342-4351.
- Archambault L, Briere TM, Ponisch F, Beaulieu L, Kuban D, Lee AK, Beddar AS 2010. Toward a real-time *in vivo* dosimetry system using plastic scintillation detectors. *IJROBP*. **78** 280-287.
- Archambault L, Therriault-Proulx F, Beddar S, and Beaulieu L 2012. A mathematical formalism for hyperspectral, multipoint plastic scintillation detectors. *Phys. Med. Biol.* **57** 7133-7145.
- Ash D, Bates T 1994. Report on the Clinical Effects of Inadvertent Radiation Underdosage in 1045 Patients. *Clin. Onc.* **6** 215-225.

- Ayotte G, Archambault L, Gingras L, Lacroix F, Beddar AS, Beaulieu L 2006. Surface preparation and coupling in plastic scintillator dosimetry. *Med. Phys.* **33** 3519-3525.
- Beddar AS, Mackie TR, Attix FH 1992a. Water-equivalent plastic scintillation detectors for high-energy beam dosimetry: I. Physical characteristics and theoretical considerations. *Phys. Med. Biol.* **37** 1883-1900.
- Beddar AS, Mackie TR, Attix FH 1992b. Water-equivalent plastic scintillation detector for high energy beam dosimetry: II. Properties and measurements. *Phys. Med. Biol.* **37** 1901-1913.
- Beddar AS, Mackie TR, Attix FH 1992c. Cerenkov light generated in optical fibres and other light pipes irradiated by electron beams. *Phys. Med. Biol.* **37** 925-935.
- Beddar AS, Kinsella TJ, Ikhlef A, Sibata CH 2001. A miniature scintillator-fiberoptic-PMT detector system for the dosimetry of small fields in stereotactic radiosurgery. *IEEE Trans. Nucl. Sci.* **48** 924-928.
- Beddar AS, Suchowerska N, Law SH 2004. Plastic scintillation dosimetry for radiation therapy: minimizing capture of Cerenkov radiation noise. *Phys. Med. Biol.* **49** 783-790.
- Beddar AS, Briere TM, Mourtada FA, Vassiliev ON, Liu HH, Mohan R 2005. Monte Carlo calculations of the absorbed dose and energy dependence of plastic scintillators. *Med. Phys.* **32** 1265-1269.
- Beddar AS 2006. Water equivalent plastic scintillation detectors in radiation therapy. *Radiation Protection Dosimetry.* **120** 1-6.
- Beddar AS 2012. On possible temperature dependence of plastic scintillator response. *Med. Phys.* **39** 6522.

- Beierholm AR, Behrens CF, Andersen CE 2014. Dosimetric characterization of the Exradin W1 plastic scintillator detector through comparison with an in-house developed scintillator system. *Rad. Meas.* **69** 50-56.
- Beringer J et al. (Particle Data Group) 2012. *Review of Particle Physics*. *Phys. Rev. D.* **86** 010001.
- Birks JB 1964. *Theory and Practice of Scintillation Counting*. Pergamom Press, New York, USA.
- Bogdanich W. “A pinpoint beam strays invisibly, harming instead of healing,” *New York Times*, December 29, 2010.
- Brannen E, Olde GL 1962. The Response of Organic Scintillators to Electron Energy Deposited in Them. *Radiation Research.* **16** 1-6.
- Bross AD 1991. Scintillating plastic optical fiber radiation detectors in high energy particle physics. *SPIE Proc. On Plastic Optical Fibers.* 108-113.
- Buranurak S, Andersen CE, Beierholm AR, Lindvold LR 2012. Temperature variations as a source of uncertainty in medical fiber-coupled organic plastic scintillator dosimetry. *LUMDETR 2012 Book of Abstracts*. Available from: <http://www.contoo.de/index.php/file/893/en_US> [27 February 2013].
- Buranurak S, Andersen CE, Beierholm AR, Lindvold LR 2013. Temperature variations as a source of uncertainty in medical fiber-coupled organic plastic scintillator dosimetry. *Rad. Meas.* **56** 307-311.
- Butler WM, Morris MN, Merric GS, Kurko BS, and Murray BC 2012. Effect of body mass index on intrafraction prostate displacement monitored by real-time electromagnetic tracking. *IJROBP.* **84** e173-79.

- Chang JY, Komaki R, Wen HY, De Gracia B, Bluett JB, McAleer MF, Swisher SG, Gillin M, Mohan R, Cox JD 2011. Toxicity and patterns of failure of adaptive/ablative proton therapy for early stage, medically inoperable non-small cell lung cancer. *IJROBP*. **80** 1350-1357.
- Cheng CW, Wolanski M, Zhao Q, Fanelli L, Gautam A, Pack D, Das I 2010. Dosimetric characteristics of a single use MOSFET dosimeter for in vivo dosimetry in proton therapy. *Med. Phys.* **37** 4266-4273.
- Clift MA, Sutton RA, Webb DV 2000. Dealing with Cerenkov radiation generated in organic scintillator dosimeters by bremsstrahlung beams. *Phys. Med. Biol.* **45** 1165-1182.
- Den RB, Nowak K, Buzurovic I, Cao J, Harrison AS, Yaacov LR, Dicker AP, and Showalter TN 2012. Implanted dosimeters identify radiation overdoses during IMRT for prostate cancer. *Int. J. Radiat. Oncol. Biol. Phys.* **83** e371-76.
- Derreumaux S, Etard C, Huet C, Trompier F, Clairand I, Bottollier-Depois J, Aubert B, Gourmelon P 2008. Lessons from recent accidents in radiation therapy in France. *Radiation Protection Dosimetry*. **131** 130-135.
- DeWerd LA, Bartol LJ, and Davis SD 2009. "Thermoluminescent dosimetry," Chapter 24 in *Clinical Dosimetry Measurements in Radiotherapy, Medical Physics Monograph #34*, Proceedings of the AAPM Summer School 2009, Colorado Springs, Colorado, June 21-25. Rogers D and Cygler J, eds (Medical Physics Publishing, Madison, Wisconsin, USA), pp 815-840.
- Edwards C, Hamer E, Mountford P, Moloney A 2007. An update survey of UK *in vivo* radiotherapy dosimetry practice. *BJR*. **80** 1011-1014.

- Edwards CR and Mountford PJ 2009. Characteristics of *in vivo* radiotherapy dosimetry. *BJR*. **82** 881-83.
- Fiorino C, Corletto D, Mangili P, Broggi S, Bonini A, Cattaneo GM, Parisi R, Rosso A, Signorotto EV, Calandrino R 2000. Quality assurance by systematic *in vivo* dosimetry: results on a large cohort of patients. *Radiother. Onc.* **56** 85-95.
- Fontebonne JM, Iltis G, Ban G, Battala A, Vernhes JC, Tillier J, Bellaize N, Le Brun C, Tamain B, Mercier K, Motin JC 2002. Scintillation Fiber Dosimeter for Radiation Therapy Accelerator. *IEEE Trans. Nuc. Sci.* **49** 2223-2227.
- Frelin AM, Fontebonne JM, Ban G, Colin J, Labalme M, Batalla A, Isambert A, Vela A, Leroux T 2005. Spectral discrimination of Čerenkov radiation in scintillating dosimeters. *Med. Phys.* **32** 3000-3006.
- Gagnon JC, Thériault D, Guillot M, Archambault L, Beddar S, Gingras L, Beaulieu L 2012. Dosimetric performance and array assessment of plastic scintillation detectors for stereotactic radiosurgery quality assurance. *Med. Phys.* **39** 429-436.
- Glasser AK, Zhang R, Gladstone DJ, Pogue BW 2014. Optical dosimetry of radiotherapy beams using Cherenkov radiation: the relationship between light emission and dose. *Phys. Med. Biol.* **59** 3789-3811.
- Guillot M, Gingras L, Archambault L, Beddar AS, Beaulieu L 2011. Spectral method for the correction of the Cerenkov light effect in plastic scintillation detectors: A comparison study of calibration procedures and validation in Cerenkov light-dominated situations. *Med. Phys.* **38** 2140-2150.
- Harrison R, Morgan A 2007. *In vivo* dosimetry: hidden dangers? *BJR*. **80** 691-692.

- Hsi WC, Fagundes M, Zeidan O, Hug E, and Schreuder N 2013. Image-guided method for TLD-based *in vivo* rectal dose verification with endorectal balloon in proton therapy for prostate cancer. *Med. Phys.* **40** 051715.
- International Atomic Energy Agency 2001a. *Investigation of an Accidental Exposure of Radiotherapy Patients in Panama, Report of a Team of Experts*. International Atomic Energy Agency, Vienna, Austria
- International Atomic Energy Agency 2001b. *TRS 398 Report. Absorbed dose determination in external beam radiotherapy; an international code of practice for dosimetry based on standards of absorbed dose to water*. International Atomic Energy Agency, Vienna, Austria.
- International Atomic Energy Agency 2013. *Human Health Report No. 8. Development of procedures for in vivo dosimetry in radiotherapy*. International Atomic Energy Agency, Vienna, Austria.
- International Commission on Radiological Protection 2000. *ICRP Publication 86. Prevention of Accidental Exposures to Patients Undergoing Radiation Therapy*. Elsevier Science.
- Jornet N, Carrasco P, Jurado D, Ruiz A, Eudaldo T, and Ribas M 2004 Comparison study of MOSFET detectors and diodes for entrance *in vivo* dosimetry in 18 MV x-ray beams. *Med. Phys.* **31** 2534-42.
- Kertzscher G, Andersen CE, Tanderup K 2014. Adaptive error detection for HDR/PDR brachytherapy: Guidance for decision making during real-time *in vivo* point dosimetry. *Med. Phys.* **41** 052102.

- Klawikowski SJ, Zeringue C, Wootton LS, Ibbot GS, Beddar S 2014. Preliminary evaluation of the dosimetric accuracy of the *in vivo* plastic scintillation detector OARtrac system for prostate cancer treatments. *Phys. Med. Biol.* **59** N27-N36.
- Klein DM, Tailor RC, Archambault L, Wang LL, Therriault-Proulx F, Beddar AS 2010. Measuring output factors of small fields formed by collimator jaws and multileaf collimator using plastic scintillation detectors. *Med. Phys.* **37** 5541-5549.
- Klein DM, Briere TM, Kudchadker R, Archambault L, Beaulieu L, Lee AK, Beddar AS 2012. In-phantom dose verification of prostate IMRT and VMAT deliveries using plastic scintillation detectors. *Radiat. Meas.* **47** 921-929.
- Kulkarni PV, Antich PP, Anderson JA, Fernando J, Aminabhavi TM, Harlapur SF Aralaguppy MI, Balundgi RH 1997. Plastic scintillating materials in nuclear medical imaging. *Polym.-Plast. Technol. Eng.* **36** 1-51.
- Lacroix F, Beddar AS, Guillot M, Beaulieu L, Gingras L 2009. A design methodology using signal-to-noise ratio for plastic scintillation detectors design and performance optimization. **36** 5214-5220.
- Lacroix F, Guillot M, McEwen M, Cojocar C, Gingras L, Beddar AS, Beaulieu L 2010. Extraction of depth-dependent perturbation factors for parallel-plate chambers in electron beams using a plastic scintillation detector. *Med. Phys.* **37** 4331-4342.
- Lambert J, Yin Y, McKenzie DR, Law S, Suchowerska N 2008. Cerenkov-free scintillation dosimetry in external beam radiotherapy with an air core light guide. *Phys. Med. Biol.* **53** 3071-3080.

- Liu PZY, Suchowerska N, Abolfathi P, McKenzie DR 2012. Real-time scintillation array dosimetry for radiotherapy: The advantages of photomultiplier detectors. *Med. Phys.* **39** 1688-1695.
- Mackowiak PA, Wasserman S, Levine M 1992. A Critical Appraisal of 98.6°F, the Upper Limit of the Normal Body Temperature, and Other Legacies of Carl Reinhold August Wunderlich. *JAMA*. **268** 1578-1580.
- Mayles W 2007. The Glasgow Incident – a Physicist’s Reflections. *Clinical Oncology*. **19** 4-7.
- Mijnheer B, Beddar AS, Izewska J, Reft C 2013. *In vivo* dosimetry in external beam radiotherapy. *Med. Phys.* **40** 070903.
- Munro AJ 2007. Hidden danger, obvious opportunity: error and risk in the management of cancer. *BJR*. **80** 955-966.
- Niroomand-Rad A, Blackwell CR, Coursey BM, Gall KP, Galvin JM, McLaughlin WL, Meigooni AS, Nath R, Rodgers JE, Soares CG 1998. Radiochromic film dosimetry: Recommendations of AAPM Radiation Therapy Committee Task Group 55. *Med. Phys.* **25** 2093-2115.
- The Royal College of Radiologists, Society and College of Radiographers, Institute of Physics and Engineering in Medicine, National Patient Safety Agency, British Institute of Radiology 2008. *Towards Safer Radiotherapy*. The Royal College of Radiologists, London, UK.
- Rozman IM, Kilin SF 1960. Luminescence of Plastic Scintillators. *Sov. Phys. Usp.* **2** 856-873.

- Saini A, Zhu T 2004. Dose rate and SDD dependence of commercially available diode detectors. *Med. Phys.* **31** 914-924.
- Saini A, Zhu T 2007. Energy dependence of commercially available diode detectors for *in-vivo* dosimetry. *Med. Phys.* **34** 1704-1711.
- Sejpal S, Komaki R, Tsao A, Chang JY, Zhongxing L, Wei X, Allen PK, Lu C, Gillin M, Cox JD 2011. Early Findings on Toxicity of Proton Beam Therapy With Concurrent Chemotherapy for Nonsmall Cell Lung Cancer. *Cancer*. **117** 3004-3013.
- Tanderup J, Beddar AS, Andersen CE, Kertzscher G, and Cygler JE 2013. *In vivo* dosimetry in brachytherapy. *Med. Phys.* **40** 070902.
- Therriault-Proulx F, Beddar S, Briere TM, Archambault L, Beaulieu L 2011a. Technical Note: Removing the stem effect when performing Ir-192 HDR brachytherapy *in vivo* dosimetry using plastic scintillation detectors: A relevant and necessary step. *Med. Phys.* **38** 2176-2179.
- Therriault-Proulx F, Briere TM, Mourtada F, Aubin S, Beddar S, Beaulieu L 2011b. A phantom study of an *in vivo* dosimetry system using plastic scintillation detectors for real-time verification of ¹⁹²Ir HDR brachytherapy. *Med. Phys.* **38** 2542-2551.
- Therriault-Proulx F, Archambault L, Beaulieu L, Beddar AS 2012. Development of a novel multi-point plastic scintillation detector with a single optical transmission line for radiation dose measurement. *Phys. Med. Biol.* **57** 7147-7159.
- Torrise L 2000. Plastic scintillator investigations for relative dosimetry in proton-therapy. *Nucl. Instrum. Methods Phys. Res.* **170** 523-30.
- Vatnitsky SM 1997. Radiochromic film dosimetry for clinical proton beams. *Appl. Radiat. Isot.* **48** 643-651.

- Wang LL, Klein D, Beddar AS 2010. Monte Carlo study of the energy and angular dependence of the response of plastic scintillation detectors in photon beams. *Med. Phys.* **37** 5279-5286.
- Wang LLW, Perles LA, Archambault L, Sahoo N, Mirkovic D, Beddar AS 2012. Determination of the quenching correction factors for plastic scintillation detectors in therapeutic high-energy proton beams. *Phys. Med. Biol.* **57** 7767-7781.
- Whaley JT, Kirk M, Cengel K, McDonough J, Bekelman J, Christodouleas JP 2013. Protective effect of transparent film dressing on proton therapy induced skin reactions. *Radiation Oncology.* **8** 19.
- Williams MV, McKenzie A 2008. Can we afford not to implement *in vivo* dosimetry? *BJR.* **81** 681-684.
- Wootton LS and Beddar AS 2013. Temperature dependence of BCF plastic scintillation detectors. *Phys. Med. Biol.* **58** 2955-2967.
- Wootton LS, Kudchadker RJ, Lee AK, Beddar S 2014. Real-time *in vivo* rectal wall dosimetry using plastic scintillation detectors for patients with prostate cancer. *Phys. Med. Biol.* **59** 647-660.
- World Health Organization 2008. *Radiotherapy Risk Profile*. WHO Press, World Health Organization, Geneva, Switzerland.
- Yorke E, Alecu R, Ding L, Fontenla D, Kalend A, Kaurin D, Masterson-McGary ME, Marinello G, Matzen T, Saini A, Shi J, Simon W, Zhu TC, and Zhu XR 2005. *Diode in vivo dosimetry for patients receiving external beam radiation therapy, Report of the American Association of Physicists in Medicine (AAPM) Task Group 62*. Medical Physics Publishing, Madison, Wisconsin, USA

Zenda S, Kawashima M, Nishio T, Kohno R, Nihei K, Onozawa M, Arahira S, Ogino T

2011. Proton beam therapy as a nonsurgical approach to mucosal melanoma of the head and neck: a pilot study. *IJROBP*. **81** 135-139

Zhao L, Das IJ 2010. Gafchromic EBT film dosimetry in proton beams. *Phys. Med. Biol.* **55** N291-N301.

Zullo JR, Kudchadker RJ, Zhu XR, Sahoo N, Gillin MT 2010. LIF TLD-100 as a dosimeter in high energy proton beam therapy – can it yield accurate results? *Medical Dosimetry*. **35** 63-66.

VITA

Landon Scott Wootton was born in Austin, Texas on January 23, 1987, the son of Robert Todd Wootton and Catherine Osha Wootton. Landon graduated from Westwood High School in 2005 and then attended the University of Texas at Austin, majoring in physics. While at The University of Texas, he worked in the lab of Dr. Karol Lang, investigating the use of liquid scintillator for neutrino detection as part of the NOvA project. He graduated in December of 2008 and came to Houston to begin graduate work at The University of Texas at Houston Graduate School of Biomedical Sciences. During his time at the Graduate School of Biomedical Sciences Landon was awarded the Faculty Merit Fellowship and the American Legion Auxiliary Fellowship in Cancer Research. Landon was married to Whitney Campbell Wootton on March 23rd, 2013.

Permanent address:

10504 Oak View Drive
Austin, Texas 78759